UNIVERSITY OF COPENHAGEN
FACULTY OF SCIENCE

Probing Binary Black Hole Formation

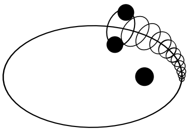

Ph.D. Dissertation

by

Kai Sebastian Paul Hendriks

Born 13.12.1996 in Nijmegen

To defend publicly in **Auditorium A, Niels Bohr Institute**
on Friday March 13th, 2026 at 14.00

This thesis has been submitted to the PhD School of The Faculty of Science,
University of Copenhagen.

This thesis was supported by the Villum Fonden grant No. 29466, and by the ERC Starting Grant no. 101043143 – BlackHoleMergs. The Center of Gravity is a Center of Excellence funded by the Danish National Research Foundation under grant No. 184. The Tycho supercomputer hosted at the SCIENCE HPC center at the University of Copenhagen was used for the high-performance-computing tasks in this work.

Printed by KU Campus Print
Cover designed by Lara Hendriks

Assessment and supervision

Supervisors

Dr. Johan Samsing	Niels Bohr Institutet, Københavns Universitet
Prof. Martin E. Pessah	Niels Bohr Institutet, Københavns Universitet

Assessment committee

Prof. Vitor Cardoso	Niels Bohr Institutet, Københavns Universitet
Prof. Fabio Antonini	Cardiff University
Prof. Manuel Arca Sedda	Gran Sasso Science Institute

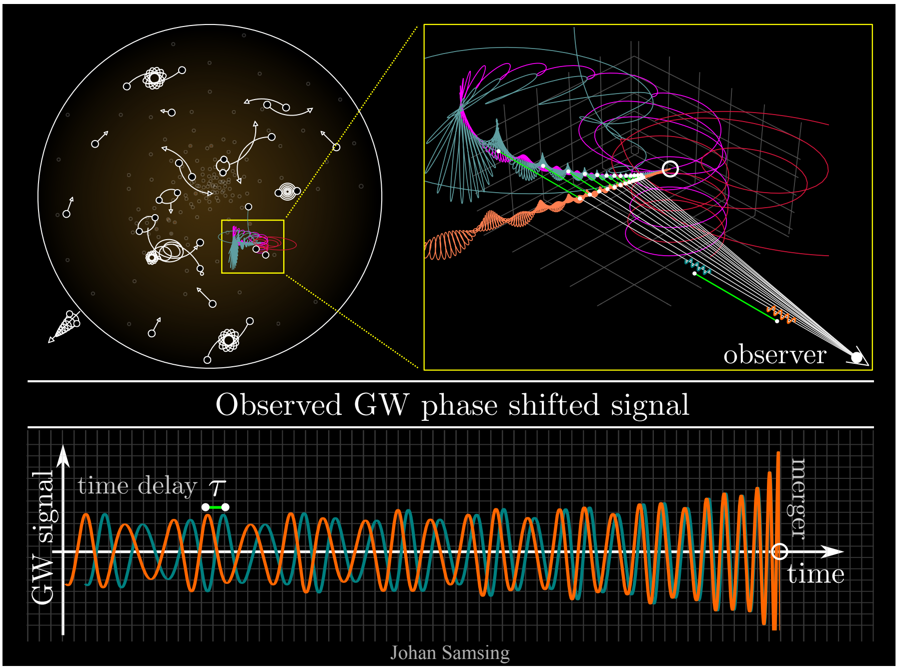

Gravitational waves from a binary black hole forming near a third black hole in a star cluster.

The same three-body interaction can be found in flip-book style on the odd-numbered pages.

Contents

Abstract

Ten years after the first observation of gravitational waves (GWs) from the collision of a pair of black holes (BHs), a central open question in GW astrophysics is how binary black holes (BBHs) form. Several formation mechanisms have been proposed, each with distinct characteristics in the populations of BBHs they produce. Recently, a complementary approach has emerged through the study of environmental effects (EEs). BBHs that form in dynamical environments such as dense stellar clusters interact with their environment, modulating their observed GW signal. Potentially detecting these imprints would allow us to directly infer the formation environment of individual BBH mergers.

This thesis examines in detail the EE of GW phase shifts due to Rømer time delay, characteristic of 3-body mergers in dynamical environments. This EE describes the dephasing of an observed GW signal due to the motion of the merging BBH on an outer orbit around a third BH. Building on existing models, I develop a semi-analytical description and analytical approximations of Rømer dephasing for systems in which both the inner and outer orbits are eccentric. I identify features of the phase shift associated with outer orbital eccentricity and establish the regimes where the eccentricity effects are strongest. I further demonstrate that the phase shift can be directly extracted from numerical 3-body scattering simulations.

In addition, I perform a controlled set of simulated 3-body interactions representative of stellar clusters, some of which result in 3-body mergers. I find that a subset of these produces large phase shifts, in some cases exceeding conservative analytical estimates. Motivated by these results, I perform a parameter study of the phase shift using an extended model which, besides outer eccentricity, includes observer projection effects. Through parameter surveys and mock inferences of circular binaries, assuming Einstein Telescope sensitivity, I show that there exist regimes where the outer orbital parameters, including the mass of the third BH, can be constrained and therefore used to deduce the BBH formation channel. Even when full parameter constraints are not achievable, the inferred limits can still be used to distinguish between a stellar-mass and supermassive BH as tertiary. Finally, I show that the previously claimed phase shift detection in GW190814 is non-physical.

This work establishes GW dephasing from Rømer time delay as a powerful tool to directly probe the astrophysical origin of BBHs forming in dynamical environments. As a new observable, it provides a direct link between simulations of astrophysical BBH-forming environments and GW data. This opens up various new avenues in understanding BBH formation from several different angles and strengthens the case for next-generation GW observatories.

Abstract på dansk

Ti år efter den første observation af tyngdebølger fra sammensmeltningen af to sorte huller er et centralt åbent spørgsmål i tyngdebølgeastrofysik, hvordan binære systemer af sorte huller dannes. Flere dannelsesmekanismer er blevet foreslået, hver med deres egne karakteristiske kendetegn i de populationer af binære sorte huller, de producerer. For nylig er en komplementær methode opstået gennem studiet af miljømæssige effekter. Binære sorte huller der dannes i dynamiske omgivelser, såsom tætte stjernehobe, interagerer med deres omgivelser som derved kan producere en modulering af det observerede tyngdebølgesignal. En mulig detektion af sådanne aftryk vil gøre det muligt direkte at udlede dannelsesmiljøet for individuelle sammensmeltninger af dobbelte sorte huller.

Denne afhandling undersøger i detaljer faseskift i tyngdebølger forårsaget af Rømer-tidsforsinkelse, som er karakteristisk for trelegeme-sammensmeltninger i dynamiske miljøer. Denne miljømæssige effekt beskriver afvigelsen i fase af et observeret tyngdebølgesignal, der opstår som følge af bevægelsen af de sammensmeltende binære sorte hullers ydre bane omkring et tredje sort hul. Byggende på eksisterende modeller udvikler jeg en semianalytisk beskrivelse samt analytiske approksimationer af Rømer-faseskift for systemer, hvor både den indre og den ydre bane er excentriske. Jeg identificerer karakteristiske træk ved faseskiftet forbundet med den ydre banes excentricitet og fastlægger de regimer, hvor disse excentricitetseffekter er stærkest. Endvidere demonstrerer jeg, at faseskiftet kan udtrækkes direkte fra numeriske trelegeme-interaktionssimuleringer.

Derudover udfører jeg et kontrolleret sæt af simuleringer af trelegemeinteraktioner, som er repræsentative for stjernehobe, og hvoraf nogle resulterer i trelegeme-sammensmeltninger. Jeg finder, at en del af disse producerer store faseskift, som i visse tilfælde overstiger konservative analytiske estimater. Motiveret af disse resultater gennemfører jeg en parameterundersøgelse af faseskiftet ved hjælp af en udvidet model, som foruden ydre excentricitet også inkluderer projektionseffekter relateret til observatørens synsretning. Gennem parameterstudier og simulerede inferenser af cirkulære dobbeltsystemer, under antagelse af Einstein-Teleskopets præcision, viser jeg, at der eksisterer regimer, hvor de ydre orbitale parametre, herunder værdien for massen af det tredje sorte hul, kan indsnævres og hvor metoden derfor kan anvendes til at udlede dannelsesmekanismen for det binære sorte hul. Selv hvis fulde parameterbegrænsninger ikke er mulige, kan de udledte grænser stadig anvendes til at skelne mellem et sort hul med stjernemasse og et supermassivt sort hul som tredje objekt. Til sidst viser jeg, at den tidligere påståede detektion af et faseskift i GW190814 ikke er fysisk velbegrundet.

Dette arbejde etablerer tyngdebølgefaseskift fra Rømer-tidsforsinkelse som et stærkt værktøj til direkte at undersøge den astrofysiske oprindelse af binære sorte huller der dannes i dynamiske omgivelser. Som en ny observerbar størrelse skaber denne effekt en direkte forbindelse mellem simuleringer af astrofysiske dannelsesmiljøer for binære sorte huller og tyngdebølgedata. Dette åbner en række nye veje til forståelse af dannelsen af binære sorte huller fra flere forskellige perspektiver og styrker argumentet for den næste generation af tyngdebølgeobservatorier.

Acknowledgements

> *"Rainy day people always seem to know when it's time to call.*
> *Rainy day people don't talk, they just listen 'til they've heard it all."*
> – Gordon Lightfoot

First of all, I would like to thank my supervisor Johan. Tusinde tak for din tro på mig og for alle de fantastiske oplevelser de sidste 3 år. You always made sure that the science we produced was the best version of itself, and prioritised my integration in the field of gravitational wave astrophysics by giving me countless opportunities to travel and network. Your continuous encouragement to discuss science with visitors of the institute, at conferences, and during my stay at Northwestern University helped me evolve as a researcher.

Also my co-supervisor Martin deserves praise (and a raise!). Thank you for always looking out for me and the others, and for making sure that we are doing OK. Your catchphrase "I think it's OK, as long as you're happy" resonates strongly within the group. I feel like I don't know half of how busy you are, yet you still always managed to make time for us. A similar sentiment goes out to our former group leader Dan: thank you for your contribution to making our group feel like home and for running it with a perfect balance between good science and good ol' hygge.

The GWAstro group would not be the GWAstro group without my fellow PhD students, office mates and friends David, Gaia, Marcela and Philip. As we have grown together as scientists, so have our friendships. They say you only learn the true nature of a person when you travel with them. I guess that is true, as I have come to deeply appreciate you guys as travel companions and friends after the many work trips we have taken together to places including Skeikampen, Aspen, Warsaw, Cambridge, Princeton (and whatever else I am forgetting). Jeg takker jer for alt det, vi har oplevet sammen!

I am also extremely fortunate to have been surrounded by our postdocs Chris, Lorenz, János, Pankaj, Connar and Alejandro. Thank you all for being someone to look up to, and for making doing science together so much fun. Our daily lunches, coffee breaks and Friday drinks at Søernes have quietly grown meaningful over the years. We collaborate and produce papers, but also find joy in each other's shenanigans. The weight of our sometimes tough academic life becomes just that little bit lighter from the support we give one another.

Believe it or not, the Niels Bohr Institute is filled with even more great people. To my friends Conor, Luka, Jose, Jaime, Thomas, Francesco, David: thank you for making life more than just doing physics. Whether it be jam sessions, trips to the Irish countryside, tennis matches, nights at Hangaren, Søhesten and Karrusel, or plunges in the Copenhagen harbour, every moment has been a true pleasure. And, most importantly, thank you for always listening when needed. Naturally, with a pint of Guinness in hand.

As the warm feeling at the Niels Bohr Institute continued at my actual home in Valbytopia, this section would be incomplete without the inclusion of my forever housemates Kristian, Filip, and Giannis. From the very day that I arrived in Copenhagen, I knew I was in good hands with you malakas. Thank you for giving me a home and for introducing me to Bang & Jensen. Our Valbytopia was probably the only place in the world where one's breakfast consists of toast with hagelslag, a shot of rakija, and a live performance of *Bella Ciao*.

Where the city of Copenhagen has been my home for over 3 years, some of my closest friendships stretch far beyond Denmark. Ever since I was a young, occasionally ambitious but mostly easily distracted wanna-be scientist in Maastricht, Lucas and Caroline have been a constant through both fortune and trouble, across borders and across time. Happy ten-year friendversary and thank you for being the kind of friends for whom distance has never really mattered.

In the same Maastricht chapter, I was fortunate enough to be mentored by Chris and Gideon. If it hadn't been for them, I might not have become a physicist in the first place. Chris, thank you for being the first one to spark my passion and for guiding me on my path. Gideon, thank you for being a great teacher, for kickstarting my academic career and for being enthusiastic about literally anything I do.

Beyond science, the core of it all is my family. Papa, mama, Lara en Jade: ik kan zo een hele waslijst met dingen opnoemen waar ik dankbaar voor ben. Om maar wat voorbeelden te bedenken, voor het plaatsvervangende enthousiasme over Kopenhagen en het Scandinavische leven, voor het afreizen naar het Noorden, voor het helpen met beide (!) verhuizingen, voor de Formule-1-video-calls, en voor de gesprekken over Carlos Alcaraz, Rob Jetten, de NAVO-top en het leven van Jade als begrafenisondernemer in Zuid-Limburg. Ja mama ik weet dat ik ver weg woon maar ik doe m'n uiterste best om wanneer het even kan in Nijmegen langs te komen.

Lastly, as proud as I am at my scientific progress, the true sense of completeness that I feel is due to my dearest Emma. En tiedä, mitä sanoa, koska on niin paljon sanottavaa. Mutta yritän: thank you for being you, for making me more mature, for being creative, for making me understand myself better, and for showing me new ways of thinking. And, above all, for your incredible support and understanding. I can't wait for our next chapter in Sweden, and I am so happy to share this adventure with you. Jag skulle rädda dig åtta gånger om dan om jag bara kunde.

List of Publications

This thesis contains the following first-author publications:

1. *"Eccentric Features in the Gravitational-wave Phase of Dynamically Formed Black Hole Binaries"*
   Kai Hendriks, Lorenz Zwick, and Johan Samsing.
   Published in *The Astrophysical Journal*, 985, 252 (2025).

2. *"Large Gravitational Wave Phase Shifts from Strong 3-body Interactions in Dense Stellar Clusters"*
   Kai Hendriks, Dany Atallah, Miguel Martinez, Michael Zevin, Lorenz Zwick, Alessandro A. Trani, Pankaj Saini, János Takátsy, and Johan Samsing.
   Under review at *Physical Review Letters*. ArXiv e-prints: 2411.08572 (2024).

3. *"Towards Gravitational Wave Parameter Inference for Binaries with an Eccentric Companion"*
   Kai Hendriks, Lorenz Zwick, Pankaj Saini, János Takátsy, and Johan Samsing.
   Submitted to *Physical Review D*. ArXiv e-prints: 2601.14918 (2026).

The following works were also co-authored by the candidate during the PhD.

4. *"Gravitational Wave Phase Shifts in Eccentric Black Hole Mergers as a Probe of Dynamical Formation Environments"*
   Johan Samsing, Kai Hendriks, Lorenz Zwick, Daniel J. D'Orazio, and Bin Liu.
   Published in *The Astrophysical Journal*, 990, 211 (2025)

5. *"Gravitational Wave Memory Imprints on the CMB from Populations of Massive Black Hole Mergers"*
   Lorenz Zwick, David O'Neill, Kai Hendriks, Philip Kirkeberg, and Miquel Miravet-Tenés.
   Published in *Astronomy & Astrophysics* Volume 694, A95 (2025)

6. *"Measuring the Transverse Velocity of Strongly Lensed Gravitational Wave Sources with Ground Based Detectors"*
   Johan Samsing, Lorenz Zwick, Pankaj Saini, Daniel J. D'Orazio, Kai Hendriks, Jose María Ezquiaga, Rico K. L. Lo, Luka Vujeva, Georgi D. Radev, and Yan Yu.
   Submitted to *Physical Review D*. ArXiv e-prints: 2412.14159 (2024)

7. *"Constraining Proper Motion of Strongly Lensed Eccentric Binary Mergers using Doppler Triangulation "*
   Johan Samsing, Lorenz Zwick, Pankaj Saini, Kai Hendriks, Rico K. L. Lo, Luka Vujeva, Georgi D. Radev, and Yan Yu.
   Submitted to *Physical Review D*. ArXiv e-prints: 2501.12494 (2025)

8. *"Environmental Effects in Stellar Mass Gravitational Wave Sources I: Expected Fraction of Signals with Significant Dephasing in the Dynamical and AGN Channels"*
   Lorenz Zwick, János Takátsy, Pankaj Saini, Kai Hendriks, Johan Samsing, Christopher Tiede, Connar Rowan, and Alessandro A. Trani.
   Published in *The Astrophysical Journal*, 991, 131 (2025)

9. *“The Construction and Use of Dephasing Prescriptions for Environmental Effects in Gravitational Wave Astronomy”*
János Takátsy, Lorenz Zwick, Kai Hendriks, Pankaj Saini, Gaia Fabj, and Johan Samsing.
Published in *The Astrophysical Journal*, 42, 215006 (2025)

10. *“Dissecting Environmental Effects with Eccentric Gravitational Wave Sources”*
Lorenz Zwick, Kai Hendriks, David O’Neill, János Takátsy, Philip Kirkeberg, Christopher Tiede, Jakob Stegmann, Johan Samsing, and Daniel J. D’Orazio.
Published in *Physical Review D*, 112, 063005 (2025)

11. *“Importance of relativistic pericenter precession in identifying the presence of a third body near eccentric binaries”*
Pankaj Saini, Lorenz Zwick, János Takátsy, Connar Rowan, Kai Hendriks, Gaia Fabj, Daniel J. D’Orazio, and Johan Samsing.
Published in *Physical Review D*, 112, 103047 (2025)

12. *“Environmental Effects in Stellar Mass Gravitational Wave Sources II: Joint Detections of Eccentricity and Phase Shifts in Binary Subpopulations”*
Lorenz Zwick, Kai Hendriks, Pankaj Saini, János Takátsy, Connar Rowan, Johan Samsing and Jakob Stegmann.
Submitted to *The Astrophysical Journal*. ArXiv e-prints: 2511.04540 (2025)

13. *“Gravitational Wave Phase Shifts of Black Hole Mergers in AGN Disks”*
Hiromichi Tagawa, Connar Rowan, János Takátsy, Lorenz Zwick, Kai Hendriks, Wen-Biao Han, and Johan Samsing.
Submitted to *The Astrophysical Journal*. ArXiv e-prints: 2511.15193 (2025)

Table 1: Frequently used symbols and abbreviations in this thesis.

Symbol/Acronym	**Description**
BH	Black hole
SMBH	Supermassive black hole
BBH	Black hole binary
GW	Gravitational wave
LVK	LIGO–Virgo–KAGRA
GC	Globular cluster
NSC	Nuclear star cluster
AGN	Active galactic nucleus
$\mathcal{PN}$	Post-Newtonian
COM	Centre of mass
LOSA	Line-of-sight acceleration
EE	Environmental effect
$M_\odot$	Solar mass
AU	Astronomical Unit
a	Semi-major axis
e	Eccentricity
f	GW frequency
m	BH mass
χ	BH spin

Chapter 1

The Origin of Binary Black Holes

"All things are so very uncertain,
and that's exactly what makes me feel reassured."
– Too-ticky in *Moominland Midwinter*

Astrophysics has allowed us to discover countless fascinating traits of our Universe and everything it contains ever since humans started to wonder. By studying the night sky, we have learnt about the nature of stars, galaxies, our own planet, even about the origins of the atoms that compose us. In its current state, however, astrophysics might have more unresolved questions than ever before. While this may sound alarming, the opposite is true. The more new unknowns arise, the more there is to uncover. "We live on an island surrounded by a sea of ignorance", as John Archibald Wheeler famously put it.[1] "As our island of knowledge grows, so does the shore of our ignorance."

Historically, astrophysics has used light as its primary source of knowledge. Electromagnetic radiation has acted as a messenger to communicate valuable information about countless astrophysical objects and phenomena to our telescopes and our own eyes. Ten years ago, a brand new messenger

---

[1] In Scientific American (1992), Vol. 267, Num. 6, page 20.

announced itself. In 2015, one hundred years after Albert Einstein predicted their existence, we observed *gravitational waves* (GWs) for the first time ever, originating from the collision of two black holes (BHs) (Abbott et al., 2016). The ability to detect GWs provided us with a completely new way to study the Universe. GWs can show us phenomena that light has never been able to probe. It meant the start of a golden era in astrophysics. A decade on, we have now observed over 200 binary BHs (BBHs) as well as a handful of colliding neutron star binaries (BNSs) and neutron star-black hole (NS-BH) mergers (The LIGO Scientific Collaboration et al., 2025a), each of which was filled with information inaccessible before.

We have already learnt a substantial amount about BBHs from GW observations. For instance, we now know that their mergers are in fact quite common, perhaps more common than expected (Abbott & et al., 2019; Abbott et al., 2024; The LIGO Scientific Collaboration et al., 2023, 2025a). We have also found that their orbits are mostly circular, with the exception of several possibly non-circular binaries (Romero-Shaw et al., 2021). Additionally, BHs are typically more massive than we had anticipated, where masses of many tens of solar masses are not uncommon (Rodriguez et al., 2015; Mandel & de Mink, 2016; The LIGO Scientific Collaboration et al., 2025a). As always, newly acquired knowledge raises even more questions. In fact, so much uncharted territory has appeared that it triggered the birth a new field: *gravitational wave astrophysics*. This field seeks to answer questions such as: where are BBHs produced? Is there more than one way to make them? Have they always been this common? How massive can they get? How long do they orbit each other before they merge?

In this thesis, I address one of the most burning central questions in GW astrophysics, namely: **how do merging black hole binaries form?** This question is so rich that it will require years of international collaboration within the GW community to get closer to an answer. Therefore, naturally, it cannot be answered in one doctoral thesis. However, in this work I lift the tip of the veil by investigating some of the many associated subquestions. I start doing so in the current Chapter 1, where I provide the necessary background information on GWs, BBHs and the different proposed formation mechanisms of BBHs. Additionally, I identify the gaps in the field and explain the approach I take in filling these. Subsequently, in Chapters 2–4 I present the different studies that I carried out in relation to this main question. The results of these are summarised and put into perspective in Chapter 5.

1.1 Theoretical background of gravitational waves

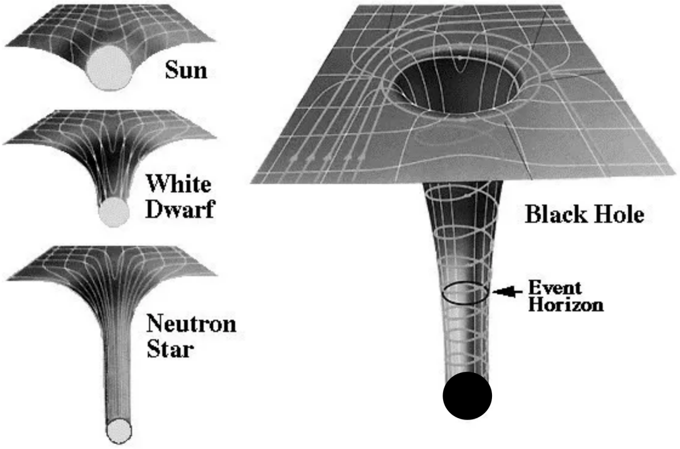

Figure 1.1: Illustration of Einstein's description of gravity. It shows 4 different types of astrophysical objects, with increasing mass. The gravitational pull of a BH is so strong, that matter reaching beyond the *event horizon* will fail to escape the gravitational well. Adapted from an illustration by Adam Apollo.

1.1.1 Black holes

In his theory of general relativity, Albert Einstein revolutionised physics by thoroughly changing our understanding of gravity. He postulated that objects with mass 'bend' the spacetime[2] that surrounds them (Einstein, 1915). This bending, or curvature, informs matter how to move in this gravitational field. The more massive the object, the more it curves its surrounding spacetime and the stronger its gravitational pull is (see Fig. 1.1). Einstein's theory predicted

---

[2] In his theory, space and time are not seen as separate, but as one combined entity.

the existence of objects whose gravity is so strong, that nothing, not even light, can escape once it gets too close (Schwarzschild, 1916). Such objects, BHs, are now known to be real (Abbott et al., 2016; Event Horizon Telescope Collaboration et al., 2019).

Different types of BHs exist. We divide them based on their mass: *stellar-mass* (with a mass of up to $\sim 100 M_{\odot}$), *intermediate-mass* ($\sim 100 - 10^{4} M_{\odot}$) and *supermassive* ($\sim 10^{5} - 10^{9} M_{\odot}$). In this work, unless stated otherwise, I focus on the stellar-mass kind. Stellar-mass BHs are the remnants of stars more massive than $\simeq 20 M_{\odot}$ (e.g. Heger et al., 2003) that have used up all of their fuel allowing it to shine. When such a star dies, the outward pressure that used to balance its inward gravitational pull disappears, causing it to implode. The remnant of this implosion is an object so dense that nothing which falls into it ever manages to climb back out: a BH (Oppenheimer & Snyder, 1939).

1.1.2 Gravitational waves

BHs are common constituents of the Universe. Consequently, it is a real possibility that one might find BHs in pairs, orbiting one another as depicted in the top part of Fig. 1.2. The spacetime that surrounds a BBH is violent; the orbital motion of these two extreme objects and their strong curvature generates ripples in this spacetime. These ripples, *gravitational waves*, travel through the cosmos and can eventually also reach the Earth, where we have the privilege to detect them. Fig. 1.2 shows the two topics that I will discuss in this Section. First, I will explain in more detail the top part of the image, i.e. how GWs are produced. Then, I will switch the attention to the bottom part and discuss the detection of GWs by describing *i)* how instruments on Earth can observe them and *ii)* how we can extract useful information from acquired GW data.

Producing gravitational waves

GWs dissipate energy and angular momentum from the BBH system. Conservation of these quantities therefore requires the BHs to get closer to one another until they eventually merge to form a single, heavier BH (e.g. Maggiore,

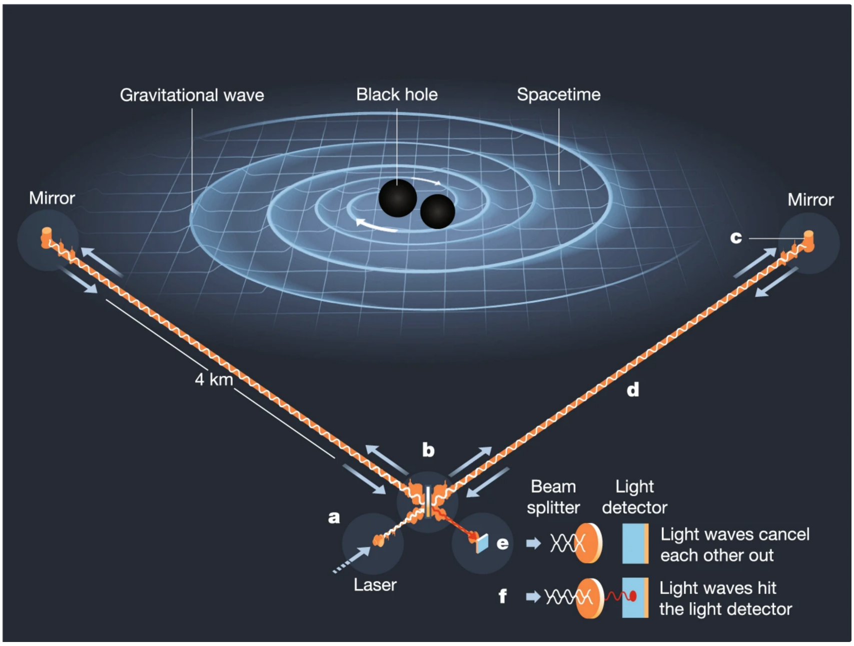

Figure 1.2: Schematic depiction of the production and detection of GWs. *Top:* a BBH that generates GWs which travel towards Earth to be detected. *Bottom:* sketch of a laser interferometer that observes GWs. We identify several parts of the detector. *a:* the source of the laser. *b:* the beam splitter that sends the laser in each of the 2 arms. *c:* a mirror that reflects the laser beam back towards the centre. *d:* the interferometer arm, i.e. the tunnel through which the laser beam travels. *e:* in the absence of a GW, the light waves from the two arms cancel each other out resulting in no signal on the detection screen. *f:* a passing GW temporarily stretches or compresses one of the arms, resulting in a signal on the detection screen. Figure taken from Castelvecchi (2018); Miller & Yunes (2019).

2007). Propagating GWs temporarily deform (i.e. stretch and compress) the space through which they travel. The distance between objects, including on Earth, is altered as a GW passes through. The relevant measurable quantity is the *GW strain*, which is defined as

$$h = \frac{\Delta L}{L}. \tag{1.1}$$

For two objects which are separated by a proper distance L, the strain is the change in their separation ΔL due to a passing GW, relative to L. How large the strain is, depends on the source of GWs, its properties and its distance from us. For BBHs, it can be approximated by (Sathyaprakash & Schutz, 2009; Moore et al., 2015)

$$h_{\mathrm{BBH}} \approx 4 \times 10^{-21} \left(\frac{100\,\mathrm{Mpc}}{D}\right) \left(\frac{\mathcal{M}}{30\,\mathrm{M}_{\odot}}\right)^{5/3} \left(\frac{f}{100\,\mathrm{Hz}}\right)^{2/3}, \tag{1.2}$$

where D and $\mathcal{M}$ are respectively the distance between Earth and the BBH, and the chirp mass

$$\mathcal{M} = \frac{(m_1 m_2)^{3/5}}{(m_1 + m_2)^{1/5}}. \tag{1.3}$$

Here, m_1 and m_2 are the masses of the two individual BHs. GWs, analagous to electromagnetic waves, have a *frequency*, which we denote by f. With typical astrophysical values for the parameters in Eq. 1.2, the measured strain of $\sim 10^{-21}$ is miniscule. To observe this, one requires an GW detector that is able to measure relative changes in separation of order 0.0000000000000000001%.

The GW strain is not static. As mentioned before, the emission of GWs from the binary pushes the BHs increasingly close together as they evolve. The closer, the higher the frequency f. From Eq. 1.2, we can see that the GW signal becomes stronger as the frequency increases. The higher the frequency, the higher the strain and the faster the frequency increases (i.e. the greater its time derivative df/dt) (Peters & Mathews, 1963; Maggiore, 2007):

$$\frac{df}{dt} = \frac{96}{5}\pi^{8/3} \left(\frac{G\mathcal{M}}{c^3}\right)^{5/3} f^{11/3}, \tag{1.4}$$

where G and c are respectively the gravitational constant and the speed of light. This runaway behaviour is called a *chirp* and is characteristic of GW mergers. The highest GW frequency that a BBH will reach is exactly when the two BHs are merging. The exact value of this frequency depends on the mass of the binary:

$$f_{\max} \approx \frac{1}{4\pi} \left(\frac{3GM}{R^3}\right)^{1/2} \approx 1\,\mathrm{kHz} \left(\frac{10\,M_{\odot}}{M}\right), \tag{1.5}$$

where for the second equality we used $R \approx \text{few} \times \frac{GM}{c^2}$ and M is the total mass of the BBH. From Eqs. 1.2, 1.4, & 1.5, we can see that BBHs with higher mass induce a larger strain than those with low mass, but also evolve faster and merge at a lower frequency.

In Fig. 1.3 we show in red how the strain evolves as a function of time. The signal that is shown is the actual recovered signal from the first GW detection GW150914 (Abbott et al., 2016). The oscillation of the strain between positive and negative values represents the fact that the passing GW alternately increases and decreases the relative distance between objects through which it travels. We distinguish three different phases in the evolution of a BBH: the *inspiral*, where the two BHs are revolving around each other and getting increasingly close, the *merger*, which is the exact moment when the two BHs coalesce, and the *ringdown*, i.e. the short period of time after the merger when the resulting, heavier BH is still vibrating from the violent merger that just happened (Maggiore, 2007). The merger and the late inspiral are the phases that current detectors can observe most precisely.

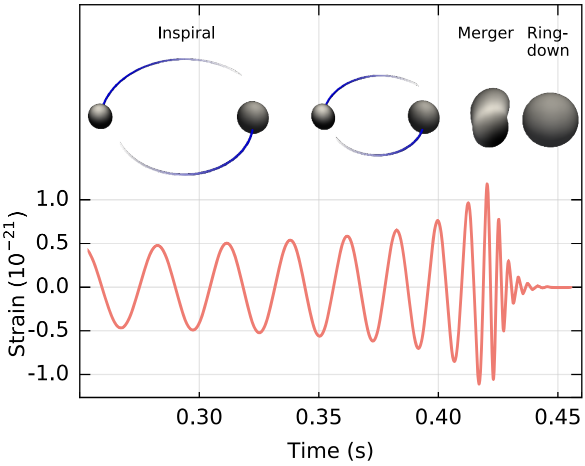

Figure 1.3: Illustration of the time dependence of the GW strain. At the top of the image, we show the relevant phases of the BBH evolution: inspiral, merger, and ringdown. This signal is in fact the reconstructed strain from the first GW detection GW159014. Image credit: LIGO/Caltech/MIT; adapted from (Abbott et al., 2016).

Detecting gravitational waves

The bottom part of Fig. 1.2 illustrates a *laser interferometer*, the type of device that is used to observe GWs. Specifically, it shows the Laser Interferometer Gravitational-Wave Observatory (LIGO) in the USA which measured the first GW signal in 2015 (Abbott et al., 2016). The LIGO instruments (there are two, one in Livingston and one in Hanford), are L-shaped observatories with arm lengths of 4km (LIGO Scientific Collaboration et al., 2015). When operational, the instrument launches a laser beam (point *a* in Fig. 1.2) which is split (b) into the two arms (*d)*, and subsequently reflected by a mirror (c) at the end of each arm to return to the centre. Without any GWs present (e), the two laser beams take exactly the same amount of time to travel back and forth through the arm and no signal is shown on the detector. If a GW passes through (scenario f), it slightly displaces the length of each arm by a different amount, resulting in a difference of arrival time of the beams. If the difference is large enough, the device can detect the GW.

GW observatories cannot just measure GWs with any frequency; they have a preferred frequency range. To understand in what regime a detector is most sensitive, one calculates its *noise power spectral density* (noise PSD), $S_n(f)$ (Maggiore, 2007). This quantity essentially tells us how much noise the detector has at each frequency. The lower, the more sensitive and therefore the better. The square root of the noise PSD $\sqrt{S_n(f)}$ is the *amplitude spectral density* (ASD). A graph of the ASD as a function of frequency is called the detector's *sensitivity curve*. We show the sensitivity curves of several current and future instruments in Fig. 1.4. Intuitively, one can understand it as follows: if a GW signal is above the sensitivity curve of a detector (the black curves), it is observable. Below, we list the different detectors along with the types of GW source they are expected to observe.

- In the high frequency range ($\sim 10 - 10^3$Hz) we find LIGO (or its most recent version advancedLIGO or aLIGO) (LIGO Scientific Collaboration et al., 2015), schematically depicted in the bottom part of Fig. 1.2. The aLIGO instrument operates in unison with the Virgo detector in Italy (Acernese et al., 2015) and KAGRA in Japan (Kagra Collaboration

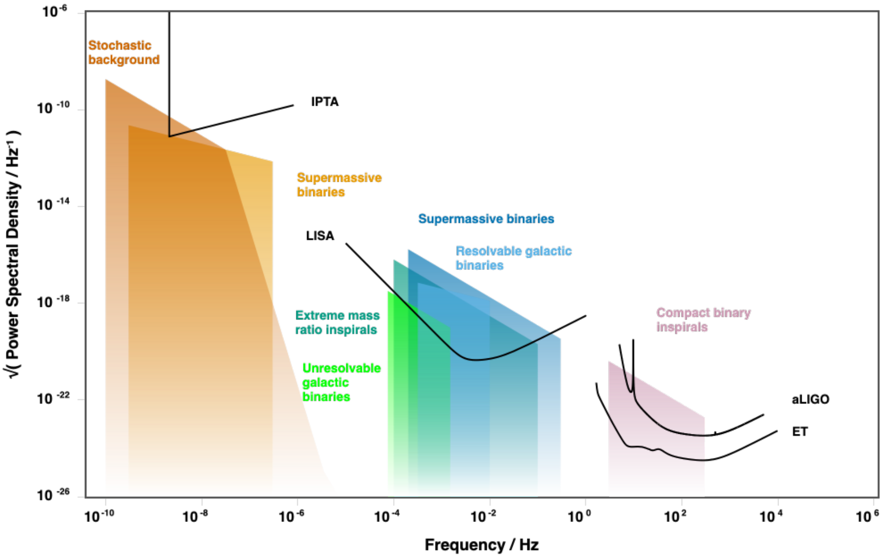

Figure 1.4: Different GW detectors (current and future) and sensitivity curves with the different GW sources they are going to be detecting. Image credit: GWPlotter.

et al., 2019) (these curves, similar range but poorer sensitivity, are not shown in this diagram). All GW detections so far have been made by the LIGO-Virgo-KAGRA (LVK) collaboration (Abbott & et al., 2019). The GW sources of interest for LVK are the inspirals of compact binaries such as BBHs, BNSs or NS-BHs. Each of these sources has their $f_{\max}$ (Eq. 1.5) within the LVK *frequency band*, so for the coalescences that close loud enough, LVK is able to detect their late inspiral and merger.

- A future ground-based GW detector that will target the same type of sources is the Einstein Telescope (ET) (Maggiore et al., 2020; Abac et al., 2025). ET, proposed to be built underground in a yet undecided location in Europe, will be $\sim$100 times more sensitive than aLIGO, and covers a wider frequency range, allowing to observe binaries earlier in their inspiral stage. As of now, ET is expected to start operating around 2035. An American counterpart to ET, the Cosmic Explorer (CE, not depicted here, Reitze et al. (2019)) will have a similar sensitivity curve.

It is expected to commence observations in the mid- to late-2030s.

- Another highly anticipated future observatory is the Laser Interferometer Space Antenna (LISA) (Amaro-Seoane et al., 2017, 2023). I show an illustration of LISA in the top panel of Fig. 1.5. LISA will operate in space. It will consist of three floating stations placed in a triangular configuration, with a 2.5 million km separation between each pair. Equivalently to LIGO, there will be a laser beam between the stations through which passing GWs can be measured. The resulting detector will trail the Earth on its orbit around the sun. Due to its much longer arm length than LIGO, LISA will be sensitive to lower frequencies, i.e. $\sim 10^{-4} - 10^{-1}$ Hz. This range is extremely rich, as there are many types of sources that emit GW radiation within it. A main target of GW sources is binaries of *supermassive BHs* (SMBHs), with masses of $\sim 10^5 - 10^6 M_\odot$. These binaries will inspiral and merge within the LISA frequency band. Additionally, LISA will be sensitive to *extreme mass ratio inspirals* (EMRIs). These are pairs of BHs that consist of one supermassive and a stellar-mass BH that orbits its larger companion. Lastly, LISA is set to observe the GWs from *galactic white dwarf binaries*. White dwarfs (WDs) are the remnants of sun-like stars that are not heavy enough to form a BH or a NS after they run out of fuel. They also exist in binary systems and emit GWs as they orbit one another. WDs are not as extreme as BHs and their emitted GWs are not strong enough to drive them closer to eventually merge in the lifetime of the Universe; we will observe them as *monochromatic sources*, where they will essentially remain at the same separation forever. Their GW signal is also relatively weak, so we will only observe those closest to us, i.e. the ones in the Milky Way. The majority of WD binaries in LISA will be *unresolvable*: a large population of binaries all emitting at different frequencies will emit a background of GWs. Disentangling the GW signals in this population from the other sources will be one of the main challenges in analysing LISA data. Fortunately, a fraction of WD binaries will be *resolvable* and we will be able to see the signals from individual events. LISA has recently been adopted by the European Space Agency and is planned for launch in the mid-2030s.

- Finally, at the lowest frequencies, we find a type of GW detector called *pulsar timing arrays* (PTAs). We show the sensitivity curve of the International PTA (IPTA, Verbiest et al. (2016)) in Fig 1.4. The bottom panel of Fig. 1.5 illustrates how PTAs measure GWs. A PTA uses *millisecond pulsars* to measure GW signals. A millisecond pulsar is a neutron star that spins rapidly around its own axis and emits flashes of light towards Earth once every few milliseconds. As the photons from each flash travel towards us and a GW passes through, slightly stretching and compressing its path, the arrival time of the photon is affected. This change in arrival time encodes the properties of the GW. A PTA uses an entire network of such pulsars to map GW signals as the same GW affects different pulsars differently. The IPTA is currently operational and has collected evidence for the detection of a *stochastic background* signal of GWs that is permanently present, most likely originating from a population of supermassive BBHs (Agazie et al., 2023). In principle, although this has not been observed yet, PTAs are also sensitive to individual SMBH mergers up to $\sim 10^9 M_\odot$ (e.g. Petiteau et al., 2013).

Analysing gravitational wave data

Naturally, collecting data with a GW observatory does not automatically mean that a GW signal is detected. If a GW is present, a highly non-trivial process follows in order to extract meaningful information about the properties of the source responsible for said signal. We break down the essentials of this important procedure in this section.

As the exact method to analyse GW data depends on the GW detector and nature of the source, we here focus on how the LVK collaboration processes its data, since this is how the sources that are of greatest interest in this thesis, stellar-mass BBHs, are observed. The method used in GW data analysis is

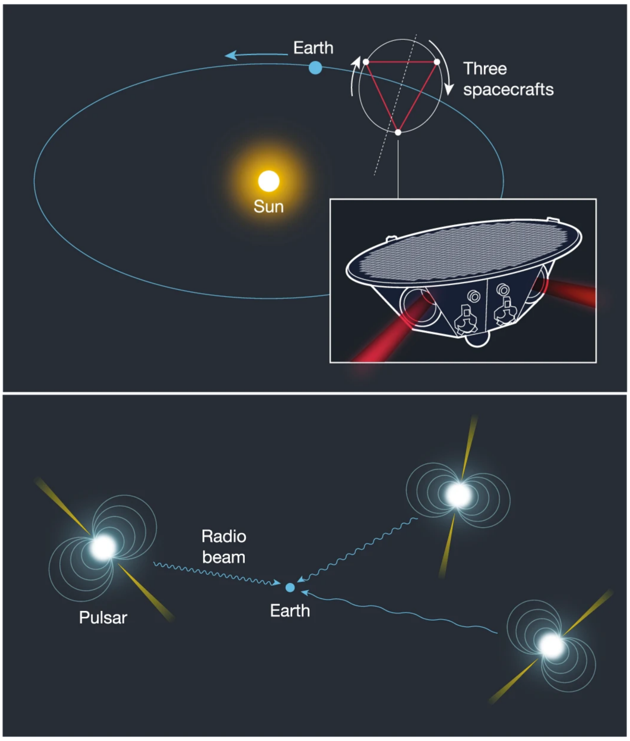

Figure 1.5: *Top:* schematic illustration of the LISA GW observatory. It shows three spacecrafts in a triangular configuration with 2.5 million kilometre laser arms between them. The interferometer is on an orbit that trails the earth around the sun and detects GWs by measuring changes in the arm lengths. *Bottom:* the concept of PTAs. We show multiple millisecond pulsars, each sending radio pulses towards earth. The timing between pulses is affected if a GW passes by and therefore contains information about the GW source. Figure taken from Castelvecchi (2018); Miller & Yunes (2019).

called *matched filtering* (e.g. Cutler & Flanagan, 1994). The signal arriving in a GW detector, which we call $s(t)$ (t because it changes over time) can be broken down as

$$s(t) = n(t) + h(t). \tag{1.6}$$

We visualise this setup in Fig. 1.6. $n(t)$ is the *noise* in the detector at time t, which is defined as ”everything in the signal that is not a GW”. It is very important that one knows $n(t)$ accurately in order to find the GW. If one is certain of the noise, then what is left in the signal is $h(t)$, the part that actually

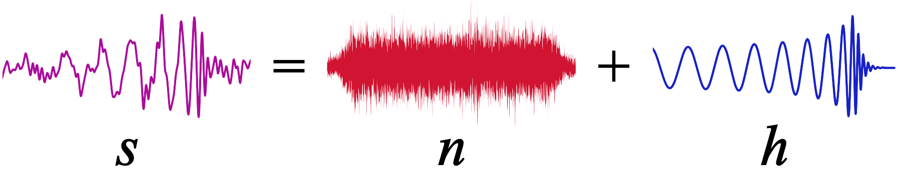

Figure 1.6: Illustration of the components of a GW signal. We distinguish the signal s, the detector noise n, and the waveform h. The properties of the sources are imprinted in h. This image uses the waveform and signal of Abbott et al. (2016).

comes from the GW. In fact, for convenience (see also Eq. 1.2) it is customary to express these quantities in terms of frequency instead of time:

$$\tilde{s}(f) = \tilde{n}(f) + \tilde{h}(f). \tag{1.7}$$

To be able to extract meaningful properties out of the signal, one needs to have a model for $\tilde{h}(f)$ that describes exactly what the frequency-dependent GW strain from e.g. a BBH looks like. This is called the *waveform model*. In principle, we already provided one here in Eq. 1.2. This is a simple waveform model that predicts how the strain depends on the BH masses (m_1 and m_2) and the separation D between us and the BBH. Let us depict a scenario where a GW from a BBH passes through the detector. Assuming that one knows the noise of the detector $\tilde{n}(f)$ (which one gets from the noise PSD $S_n(f)$), one can then extract the properties of the BBH from this signal. One needs to find the combination of masses and distance which gives a realisation of $\tilde{h}(f)$ that matches the measured signal best. The way this is carried out is essentially through trial-and-error: one computes $\tilde{h}(f)$ for many different combinations of values for m_1, m_2 and D. Each combination of these values and its resulting $\tilde{h}(f)$ is called a *template*. The criterion for finding the best-fit template is the *signal-to-noise ratio* (SNR). This quantity tells us how well the template matches the measured signal, taking into account the noise characteristics of the detector. Mathematically,

$$\mathrm{SNR} = \sqrt{\int_0^\infty \frac{|\tilde{h}(f)|^2}{S_n(f)} df}. \tag{1.8}$$

The higher the SNR, the better the chosen template fits the data. Generally, a signal is seen as ”detected” if SNR $\gtrsim 8$ (Abbott et al., 2016). The waveform model in Eq. 1.2 that we used for this explanation is too simplistic for actual analyses. The LVK collaboration has developed many different waveform models which are significantly more complex and describe signals from BBHs more accurately. Where Eq. 1.2 uses 2 parameters, real LVK models could have as many as 16 (e.g. Pratten et al., 2021).

1.2 Astrophysical formation of binary black holes

With the required background information, we may now return to the main premise of this work, namely to shed light onto how BHs are able to form binary systems in the first place. Naturally, many other studies have preceded this one and have produced valuable knowledge that helps in answering this question. In this Section, I summarise the current state of the art in GW astrophysics on what we, as of yet, know about the assembly mechanisms of BBHs.

GW astrophysics predicts that there are in fact multiple ways through which BBHs can pair up. Different assembly methods are typically placed in one of two buckets: *isolated formation* and *dynamical formation*. Each of these is called a *formation channel*. They can be distinguished as follows:

- The **isolated formation** scenario begins with two stars that were born from the same cloud of gas and therefore closely orbit each other in a binary throughout their entire lifetime. Eventually, each star collapses and turn into a BH, forming a tight BBH. This BBH then inspirals and merges.

- In the case of **dynamical formation**, the BBH does not assemble in isolation. Instead, astrophysical environments such as dense star clusters or gaseous accretion disks interact with the BHs contained within them, occasionally producing BBHs that are tight enough to they emit GWs and eventually merge.

One can imagine that the dynamical formation channel requires a specific environment where the density of BHs is high enough that close encounters between single BHs are frequent enough that mergers can be produced. An important candidate environment is that of *star clusters* or *stellar clusters* (e.g. Rodriguez et al., 2015, 2016a); these are big clouds of stars which are all gravitationally bound to one another (e.g. Sparke & Gallagher, 2000; Binney & Tremaine, 2008). Naturally, such clusters also have a high density of BHs. Additionally, BBHs are believed to form dynamically in *the accretion discs of active galactic nuclei (AGN)* (e.g. McKernan et al., 2018; Samsing et al., 2022). These are large discs of gas around a SMBH, in which stellar-mass BHs reside and can form binaries. Both of these environments produce BBHs with distinct features in their GW signal, and are therefore seen as *sub-channels* of the dynamical channel. We name them the *cluster channel* and the *AGN channel*.

I schematically depict the different formation environments in Fig. 1.7. In the bottom part of the same image, I also show the properties of the BBHs produced through each channel. The relevant parameters are the following:

- The **masses** of the BHs. We distinguish the component masses m_1 and m_2 as well as the mass ratio $q = m_1/m_2$ (where m_1 is the heavier BH).
- The **spins** of the BHs, i.e. how fast and in what direction they rotate around their own axis. The spin parameter χ has a value between 0 (non-spinning) and 1 (maximally spinning).
- The **eccentricity** of the BBH, i.e. how circular ($e = 0$) or elliptic ($e = 1$) the orbit is.

Each of these parameters can be measured in the GW signal. Below, I discuss in more detail how BBHs are produced in each (sub-)channel.

1.2.1 Isolated formation

BBH formation in the isolated scenario starts with a binary of two stars on the main sequence (MS), i.e. fusing hydrogen to form helium and shining from

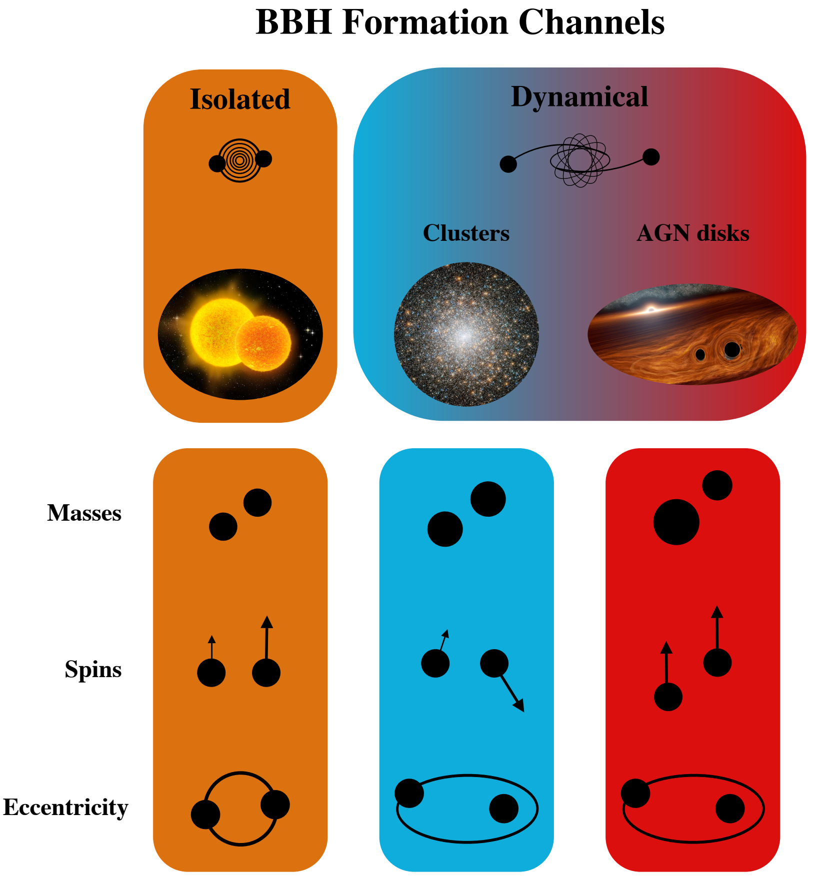

Figure 1.7: The main formation channels of GW-emitting BBHs. We distinguish isolated and dynamical origins. Where the isolated branch forms BBHs directly from stars in binary systems, BBHs can assemble dynamically either in star clusters or in the discs of AGN. In the bottom of this schematic I show the masses, spins and eccentricities by which binaries formed in each channels are typically characterised.

the energy release of said process. The key for this binary to become a BBH that emits GWs and merges is for the stars to both collapse to a BH and for the BHs to be close enough that gravitational radiation is strong enough to drive the evolution. The initial orbital separations of MS binaries are necessarily too wide for GW emission to dominate the evolution, given the large radii of the stars. As such, some mechanism is required to drive them closer together. In Fig. 1.8 I visualise the typical formation pathways of GW-emitting BBHs in this channel. In the initial MS stage, the heavier star A is the first to burn

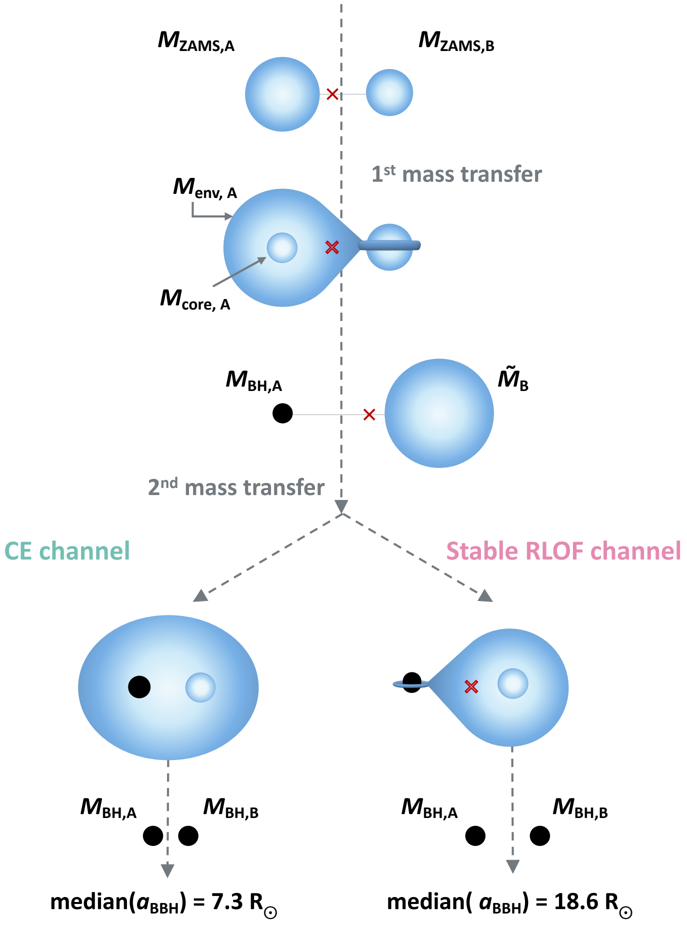

Figure 1.8: Cartoon depiction of the typical evolution of a stellar binary in the isolated channel to form a BBH. The symbols refer to mass of the star at zero-age main sequence (M_{ZAMS}), envelope mass (M_{env}), core mass (M_{core}), BH mass (M_{BH}), mass after mass transfer ($\tilde{M}$), common envelope (CE), Roche lobe overflow (RLOF), and BBH separation (a_{BBH}). The subscripts A and B respectively denote the primary (more massive) and secondary star. The red mark represents the location of the binary centre of mass. Figure was taken from van Son et al. (2022).

through its hydrogen reservoir. Upon completion of hydrogen fusion, its core (now composed of helium) contracts. At the same time its outer layers expand to form a large envelope around the star. This initiates *Roche lobe overflow* (RLOF), transferring mass to star B. Following the mass-transfer phase, star

A ultimately collapses to a BH, leaving star B more massive and extended (third stage from the top in Fig. 1.8) (e.g. Mandel & Farmer, 2022; van Son et al., 2022).

Subsequently, a second mass transfer stage happens. Similar to before, the core of star B now contracts and its outer layers expand, forming a large envelope of thick gas around the star. The envelope transfers mass from star B to the BH. Two BBH-forming scenarios are now possible. On the one hand, if the mass transfer is unstable, the gas envelope ends up surrounding the pair as a *common envelope* (CE). The CE channel is depicted on the bottom left side of the cartoon. Friction between the stars and the envelope then drives the the stars closer together. Eventually, star B also collapses to a BH and a BBH is created. On the other hand, if the second mass transfer is stable, the CE phase is not initiated and instead a second RLOF stage occurs. In some cases the mass transfer may remove angular momentum from the binary, pushing it closer together. When star B eventually collapses to a BH, a tight BBH is the final result (Tutukov & Yungelson, 1993; Belczynski et al., 2016a; Mandel & Farmer, 2017; Stevenson et al., 2017).

The masses of BHs in binaries formed through the isolated formation channel typically do not exceed $\sim 50 M_\odot$ (Mandel & Farmer, 2022). Dynamical formation scenarios are a more favourable explanation for BBHs with high component masses. Generally, the isolated channel is expected to produce mostly equal-mass binaries. The multiple episodes of mass transfer cause the spins of BBHs in this channel to typically be aligned with the orbital angular momentum, i.e. the rotation axis for both BHs points in the same direction as the rotation axis of the orbit (Gerosa & Berti, 2017). While the progenitor stars to the BHs may be rapidly spinning, most of the angular momentum is contained in the outer layers which is lost throughout the evolution, leading to BHs with generally low spin magnitudes (Mandel & Farmer, 2022). In some cases, however, tidal interactions in the binary may spin up the BH (Kushnir et al., 2016; Hotokezaka & Piran, 2017; Zaldarriaga et al., 2018). This is especially relevant for the CE channel (Zevin et al., 2021; Bavera et al., 2021). The orbits of BBHs formed in isolation are expected to be circular.

- **Masses**: preferably low masses (up to $\sim 50M_\odot$) and equal-mass binaries.
- **Spins**: aligned with the angular momentum of the binary, while the magnitude depends on subtleties in the evolution, in principle allowing for both low and high spin.
- **Eccentricity**: predominantly circular.

1.2.2 Dynamical formation

In the dynamical channel, BBHs do not descend from isolated stellar binaries. Instead, they assemble through close gravitational encounters between BHs, often involving multiple interactions (Heggie, 1975; Binney & Tremaine, 2008). A dynamical encounter between BHs is often called a *scattering* and may be highly chaotic in nature. The GW signals from dynamically assembled BBHs can have distinct features that sets them apart from the isolated channel. Below, I discuss the two main types of astrophysical environments that host dynamically formed BH binaries.

Stellar clusters

Stellar clusters are gravitationally bound groups of stars that all formed from the same cloud of gas and therefore have similar age and chemical compositions. Stellar clusters are ideal nurseries for both BHs and BBHs. In terms of BBH formation, two different types of cluster are relevant: *globular clusters* (GCs) and *nuclear star clusters* (NSCs) (e.g. Sparke & Gallagher, 2000; Binney & Tremaine, 2008). GCs are clusters that contain anywhere between tens of thousands and millions of stars, and span tens to hundreds of lightyears. They are very dense, especially in their centres, and are therefore ideal environments for strong interactions between BHs. NSCs sit closer to the centre of a galaxy and are strongly influenced by the presence of the SMBH at the centre of the galaxy with effective radii of several parsecs. With typically several millions of stars, they are even denser than GCs.

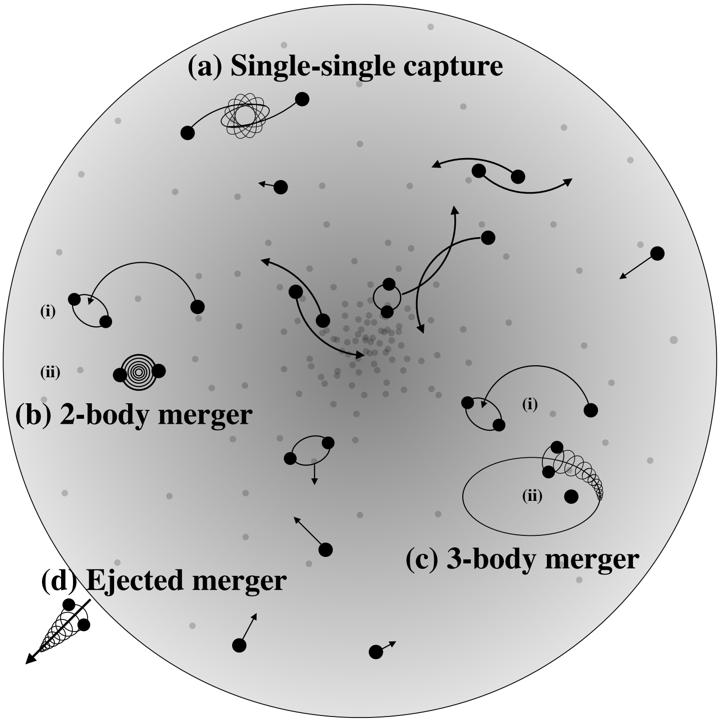

Figure 1.9: Four different ways to dynamically assemble a BBH in a GC. Figure adapted from Samsing et al. (2020).

Fig. 1.9 schematically depicts a GC to represent the cluster sub-channel. We distinguish 4 different types of interactions between BHs that lead to mergers.

Single-single captures

Two BHs that are initially unbound (positive orbital energy) can become bound in a BBH if they pass each other close enough that GW radiation dissipates energy from the system. The BBH is typically highly eccentric right when it forms ($e \sim 1$). GWs circularise the orbit of the BBH as it inspirals (Maggiore, 2007); when the binary merges, its orbit will be completely circular. BBHs formed in this way may, however, still have some residual eccentricity when they enter the LVK band. These mergers only make up a few per cent of BBHs from clusters (Samsing et al., 2020).

2-body mergers

Binary-single scatterings are common occurrences in clusters. In this type of encounter a third BH flies closely past a bound binary (that is not tight enough to emit GWs and inspiral). This is depicted in sketch *(b)-i)* in Fig. 1.9. A possible outcome (shown in *(b)-ii)*) is a scenario where one of the three BHs is ejected from the system, and a tighter binary is formed whose evolution is GW-dominated. The binary is so tight that it merges before a potential next encounter with a new third BH. Where these 2-body mergers are initially eccentric, they tend to circularise before entering the LVK band. 2-body mergers in their eccentric phase may, however, be observable in the LISA frequency band. It should be noted that *binary-binary scatterings*, not depicted in Fig. 1.9 to preserve clarity, are also an efficient way to form 2-body mergers. It is expected that $\sim 40\%$ of BBHs in clusters assemble through a 2-body merger (Samsing & D'Orazio, 2018).

3-body mergers

Another outcome of binary-single (or binary-binary) scatterings is a 3-body merger. In this case, at some point in the interaction, a close pericentre passage between two of the BHs occurs where GW radiation dissipates so much energy that the entire 3-body system becomes bound. The outcome *(c)-ii)* is an inspiralling and merging BBH whose centre-of-mass is on a bound orbit around the third BH. Since this requires a closer passage than for a 2-body merger, it is less common. The tight binary that forms at the close pericentre passage is highly eccentric upon formation ($e \sim 1$) and may have residual eccentricity when it eventually enters the LVK frequency band. About 10% of mergers in clusters have this origin (Samsing & D'Orazio, 2018).

Ejected mergers

A fourth possible type of merger is one that eventually occurs *outside* of the cluster. A binary–single interaction may form a tight BBH that is subsequently ejected from the cluster through dynamical recoil imparted by the third BBH. A large fraction of BBHs may follow this path. Once this type of merger enters the LVK band it has mostly circularised. This type of outcome is believed to be the case in about 50% of all binaries that form in clusters (Samsing & D'Orazio, 2018; Rodriguez et al., 2018; Samsing et al., 2020).

Clusters allow for higher BH masses than the isolated channel due to the possibility of *hierarchical mergers*; the remnant BH from a BBH collision may subsequently merge with another BH in a dynamical encounter. The remnant from any GW merger receives a *recoil kick* arising from asymmetries in the system (e.g. in the masses). A subsequent merger is only possible if the kick velocity is lower than the escape velocity of the cluster. If it is not, the remnant BH gets ejected from the cluster. In principle, hierarchical mergers can happen in GCs. However, a more favourable environment for this is that of NSCs; the presence of a central SMBH in NSCs results in escape velocities of several hundreds of km/s, which makes it more likely that remnants are retained and therefore makes higher generations of BH mergers more frequent (Binney & Tremaine, 2008).

An important process in clusters is *two-body relaxation* (Sparke & Gallagher, 2000; Binney & Tremaine, 2008). This is the cumulative effect of many weak gravitational encounters between objects in a stellar cluster, which gradually redistribute orbital energies and angular momenta. Through this process the system evolves toward partial energy equipartition, such that more massive objects lose kinetic energy on average while lower mass ones gain it. As a result, massive BHs sink further into the cluster core than lighter ones. This process is called *mass segregation* and is the reason why equal-mass mergers are the most common in the cluster channel (e.g. Rodriguez et al., 2016a). The spin orientations of cluster-assembled BBHs are typically isotropically distributed (Rodriguez et al., 2016c; Farr et al., 2017). The spin magnitudes depend on the BHs' individual formation, where hierarchical mergers typically have higher spins ($\chi \sim 0.7$).

- **Masses**: high mass possible, but not common, although more likely in NSCs. Mergers are preferably equal-mass.

- **Spins**: isotropically distributed (random). Both small and large spins are possible.
- **Eccentricity**: both circular and eccentric (in the LVK band) mergers are possible, where eccentricity is a key indicator of a dynamical formation history.

Active Galactic Nuclei

Observations have shown that most galaxies host an SMBH at their centre (e.g. Magorrian et al., 1998). The compact region in the centre of some galaxies is ”active”, i.e. the BH is surrounded by a disc of gas and accretes matter. The accretion that takes place between the gas and the SMBH makes this region extremely luminous, bright enough to be electromagnetically observable (Netzer, 2013). The accretion disc of such an Active Galactic Nucleus (AGN) can be the host environment of dynamically forming BBHs. We show a visualisation of an AGN disc in Fig. 1.10, including different types of mergers.

BHs in AGN discs are either born from a star in the disc or brought into the disc from the NSC that surrounds it. They migrate radially through the disc and may interact with other BHs. Similarly to inside clusters, merging BBHs can be formed in single-single captures, or in 2- or 3-body mergers through binary-single or binary-binary interactions (Samsing et al., 2022). The main difference with the cluster channel is that the presence of the gaseous disc influences the formation process of BBHs. This manifests itself in several ways in observable features of the GW signal. One key distinction with cluster formation is that the AGN channel allows for higher BH masses (e.g. Bellovary et al., 2016; Vaccaro et al., 2024, 2025). AGN discs provide an environment in which BHs can grow efficiently. Firstly, BHs embedded in the disc can gain mass by accreting gas. Secondly, BHs produced by mergers are more likely to remain in the disc. Although a BH merger remnant receives a GW kick, the surrounding gas can slow it down and prevent it from escaping. This allows the remnant to stay in the disc and take part in further mergers. As a result, AGN discs naturally allow for repeated, hierarchical mergers, leading to heavier BHs than typically formed in stellar clusters. These environments

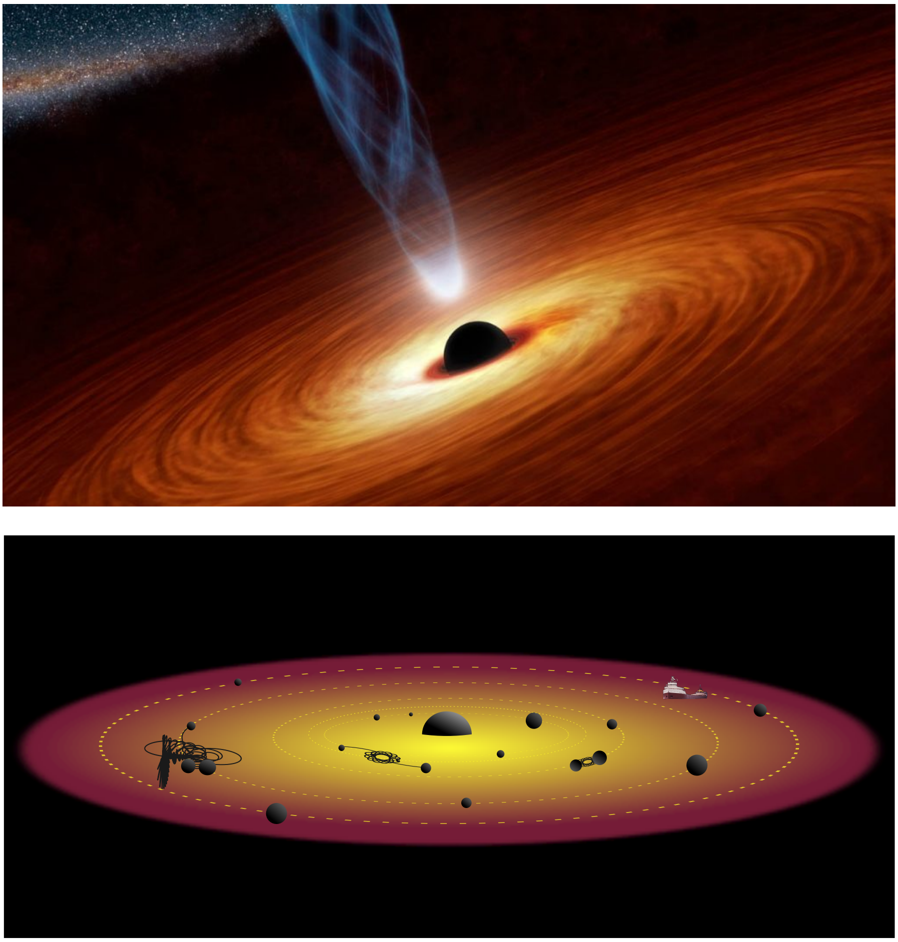

Figure 1.10: *Top:* artist impression of an AGN. It shows the central SMBH, its surrounding accretion disc, and a luminous relativistic jet perpendicular to the disc. Image credit: NASA/JPL-Caltech. *Bottom:* sketch of the different types of BH interactions within an AGN disc. We distinguish 3-body mergers (left), single-single captures (left of the middle), and 2-body mergers (right). Similar to cluster formation, 2- and 3-body mergers can occur as a result of binary-single and binary-binary scatterings. Image adapted from Samsing et al. (2022); Tagawa et al. (2025).

therefore produce a wider range of merger masses, as well as a wider range of mass ratios as heavier BHs may also collide with lighter, lower-generation BHs (Yang et al., 2019; Tagawa et al., 2020). The spins of BHs in AGN discs tend to be high (even up to $\chi \sim 1$) and aligned with the angular momentum of the disc, as gas accretion can efficiently torque the BHs toward this preferred direction (e.g. McKernan & Ford, 2024). In contrast, as a result of the dynamical interactions the BHs undergo, the orbital angular momentum of the BBH is not necessarily aligned with the disc (Fabj et al., 2025). As in stellar clusters, dynamical interactions can produce both circular and eccentric binaries. The presence of gas adds an additional layer of complexity, as disc interactions may significantly alter BBH dynamics including eccentricity damping or excitation, depending on the specific conditions (Rowan et al., 2023, 2024; O'Neill et al., 2024; Rowan et al., 2025a).

- **Masses**: both low and higher mass possible, including equal-mass and non-equal mass mergers.
- **Spins**: preferably high and aligned with the angular momentum of the disc.
- **Eccentricity**: both circular and eccentric mergers possible.

1.3 Environmental effects: this thesis in context

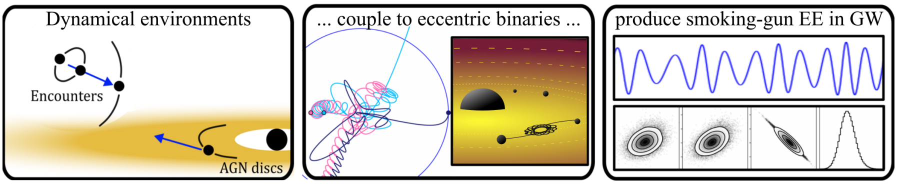

Figure 1.11: General rationale for the study of environmental effects (EEs) that motivates the work I present in this thesis. EEs are the direct imprints of realistic environmental effects onto BBH waveforms that act as smoking-gun signatures to probe the BBH formation channel. Figure adapted from Zwick et al. (2025b).

The advances in GW astrophysics outlined above have already provided valuable insights into the origins of BBH mergers. Current observations can now be interpreted in terms of likely formation channels, and population studies have begun to reveal clear trends in BH masses, spins, and orbital properties (The LIGO Scientific Collaboration et al., 2025b). However, these inferences are inherently statistical in nature. They rely on *population-level* predictions and allow only general statements, e.g. that mergers in AGN can have high masses or that isolated binaries tend to have aligned spins. While powerful, this approach cannot, on its own, tell us how a *specific* BBH merger formed. It allows for hints towards likely formation channels for individual events, but cannot directly determine their astrophysical origin.

A new, complementary way of inferring formation channels is through so-called *environmental effects* (EEs) (e.g. Barausse et al., 2014; Meiron et al., 2017; Torres-Orjuela et al., 2019; Derdzinski et al., 2021; Garg et al., 2022; Cardoso et al., 2022; Speri et al., 2023; Zwick et al., 2023; Tiede et al., 2024; Dyson et al., 2024; Zwick et al., 2024; Duque et al., 2025; Spieksma et al., 2025). Rather than asking what properties a population of mergers should have, this approach focuses on how the surrounding environment *directly imprints itself* on the GW signal emitted by a single binary. For dynamically formed systems, the binary does not evolve in isolation, but interacts continuously with its environment. An illustrative example is a BBH embedded in the disc of an AGN, where interactions with the surrounding gas can directly modify the emitted waveform (e.g. Antoni et al., 2019; Whitehead et al., 2024; Rowan et al., 2023, 2025b,a). By modelling these environmental imprints, it becomes possible to identify the astrophysical environment of an individual merger, providing a *smoking-gun signature* of the formation environment. This is a fundamentally different and more direct route to constraining binary formation.

The new results that I present in this thesis are fully motivated by this novel approach in probing BBH formation. I illustrate its rationale in Fig. 1.11. Several distinct types of EEs can arise in realistic astrophysical settings. For instance, as mentioned above, the presence of gas in an AGN disc can directly modify the GW signal of a BBH forming within the disc. In other scenarios, such as 3-body mergers, the GW signal can be influenced by the presence and motion of a third BH (e.g. Yunes et al., 2011; Antonini et al., 2016; Arca Sedda et al., 2021; Zwick et al., 2025b). Each of these effects can be studied extensively in its own right.

In this thesis, however, I focus on a single EE. I address **how the orbital motion of a merging BBH in a 3-body system leaves a measurable imprint on the observed GW signal**. Below, I discuss this effect in more detail and explore its implications for identifying the formation environment of BBH mergers.

1.3.1 Binaries from 3-body encounters: Rømer time delay

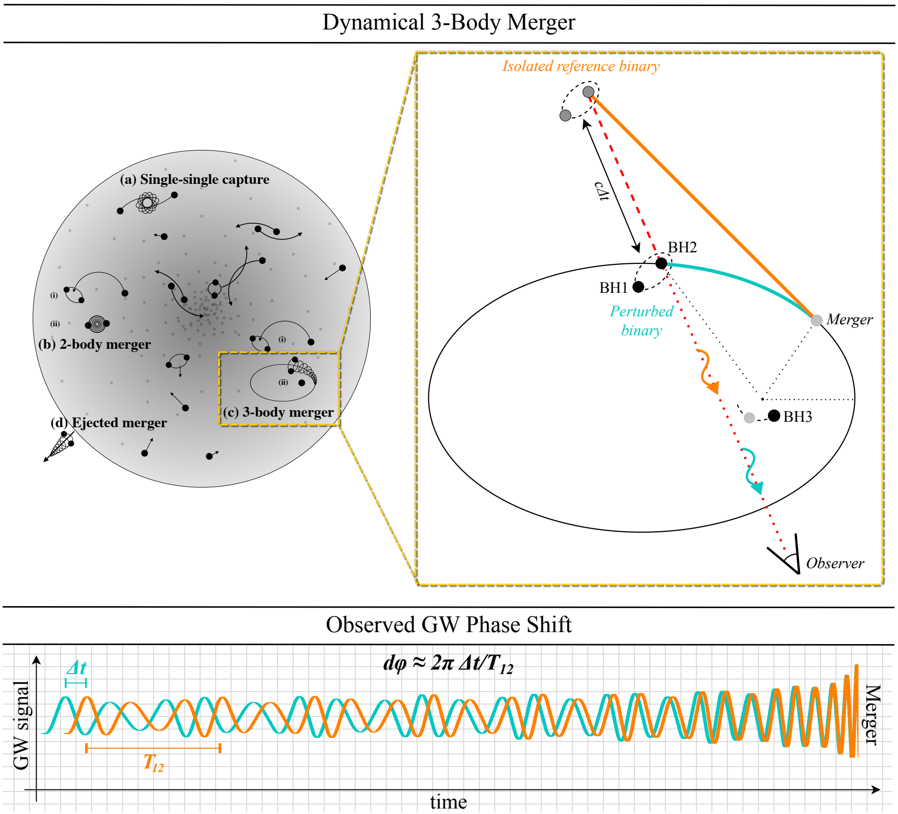

Figure 1.12: Setup of the type of EE studied in this thesis, occurring in 3-body mergers. The orbital motion of the COM of the merging binary (BH1-BH2) around a third bound BH induces a phase shift in the observed GW signal. The phase shift contains the orbital properties of the orbit around BH3, which can in principle be inferred directly from the GWs. It should be noted that in this setup and the equations outlined below, we assume an ideal observer: it always sees the maximum possible phase shift, so it ”rotates” along with the binary around BH3.

Fig. 1.12 visualises the concrete effect that I study in this thesis: *GW* *phase shifts due to Rømer delay*. This EE is relevant for 3-body mergers inside stellar clusters or AGN discs. The BBH that will eventually merge, consisting of BH1 and BH2, forms through a close pericentre passage while it is bound to BH3 (Samsing et al., 2025). The binary is highly eccentric ($e \sim 1$) when it forms, but eventually circularises as it inspirals. We call the orbit of BH1-BH2 the *inner orbit*. Since it is bound to BH3, the centre of mass (COM) of the binary moves on a larger *outer orbit* around the third BH as it inspirals. Eventually, it merges in a different place on the outer orbit than where it formed. In Fig. 1.12 we compare the real, perturbed path (in turquoise) of the BBH COM with the path it *would have had* if BH3 had not been present. The latter, depicted in orange, would have simply been a straight line with a constant speed (equal to the outer orbital speed at merger). This is simply a reference binary that does not actually exist; the real signal that one observes is that of the perturbed binary.

We may compare the GW signals from both the perturbed binary and the isolated reference binary. We assume that both merge at the same point in time and in the same place on the outer orbit. We place an observer in our schematic who receives the GW signal from either binary. Just like electromagnetic waves, GWs have a finite travel speed: the speed of light. It is evident from the sketch in Fig. 1.12 that GWs from the isolated binary have to travel a larger distance to the observer compared to those from the perturbed binary emitted at the same time. The difference in travel time results in a *time delay* $\Delta t(t)$ of the observed GW signal. The bottom panel of Fig. 1.12 shows the time delay between the two GW signals. If we equate the time delay relative to the orbital period of the inspiralling binary BH1-BH2, we have a *GW phase shift*:

$$d\phi(t) \approx 2\pi \frac{\Delta t(t)}{T_{12}(t)}. \tag{1.9}$$

The phase shift encodes the properties of the third body and can therefore *directly probe the formation environment of the BBH*. It can be included in waveform models in order to be used in real detection data analysis.

The exact form of Eq. 1.9 depends on the assumptions made for the 3-

body system. Its simplest form assumes a *circular outer orbit*:

$$\Delta\phi(t) \approx \frac{1}{2}\frac{G^{3/2}}{c}\frac{m_3 m_{12}^{1/2}}{R^2} \times \frac{t^2}{a(t)^{3/2}}. \tag{1.10}$$

Here we can see that the phase shift depends on the BH3 mass m_3, binary mass m_{12} and distance R between BH1-BH2 and BH3. It also depends on the time-dependent semi-major axis of BH1-BH2 $a(t)$ which decreases as the binary inspirals. How a and t relate to one another is dependent on whether the binary is circular or eccentric. For circular BBHs (Peters, 1964),

$$t_c = (5/256)(c^5/G^3)a^4 m_1^{-1} m_2^{-1} m_{12}^{-1}. \tag{1.11}$$

The phase shift when *both the inner and outer orbit are circular* then becomes

$$\Delta\phi(t) \approx \frac{c^{7/8}G^{3/8}}{2}\left(\frac{5}{256}\right)^{3/8} \times \frac{m_3}{R^2}\frac{m_{12}^{1/8}}{m_1^{3/8}m_2^{3/8}} \times t^{13/8}. \tag{1.12}$$

Or, in terms of the orbital frequency $f_{\rm orb}$:

$$\Delta\phi(f, e=0) \approx \frac{c^9 G^{-7/3}}{2\pi^{13/3}}\left(\frac{5}{256}\right)^{2} \times \frac{m_3}{R^2}\frac{m_{12}^{2/3}}{m_1^2 m_2^2} \times f_{\rm orb}^{-13/3}. \tag{1.13}$$

This tells us that the phase shift is smallest when the BBH is close to merger (t close to 0 and high $f_{\rm orb}$), and therefore largest early in the evolution of the binary. This circular limit has been extensively studied (Yunes et al., 2011; Meiron et al., 2017; Bonvin et al., 2017; Robson et al., 2018; Vijaykumar et al., 2023; Tiwari et al., 2024). It should be noted that Eq. 1.13 is off by a factor of 2 compared to its version in these references. The reason for that is that I work with the orbital frequency here instead of the GW frequency to facilitate the transition from circular to eccentric binaries. Only in the circular case, the relation $f_{\rm GW} = 2f_{\rm orb}$ holds. Eccentric binaries emit GW radiation at multiple frequencies (Peters & Mathews, 1963), making the relation more complicated.

An important characteristic of BBHs in 3-body mergers is that the binary is highly eccentric when it forms. Therefore, the assumption of a circular inner orbit is not valid for these encounters. In Samsing et al. (2025), we extend the phase shift prescription to *eccentric inner orbits and circular outer orbits*. In the highly eccentric limit of $e \sim 1$ (Peters, 1964),

$$t_e \approx t_c \times (768/425)(1 - e^2)^{7/2}, \tag{1.14}$$

where t_c is given by Eq. 1.11 and e is the binary eccentricity. In the eccentric limit, the GW phase shift scales as

$$\Delta\phi(t) \propto t^{-1}. \tag{1.15}$$

Interestingly, this implies that the phase shift for highly eccentric binaries actually *increases* as the BHs get closer to one another. While this is correct for the initial stage of evolution, it does not keep increasing forever as the binary will eventually circularise and the phase shift will return to the $t^{13/8}$ dependence of Eq. 1.12. This initial rise and eventual turnover to a decreasing phase shift closer to merger implies the occurrence of a maximum in phase shift. This happens at $e \approx 0.95$ (Samsing et al., 2025); after that, the phase shift drops. I visualise this finding in Fig. 1.13.

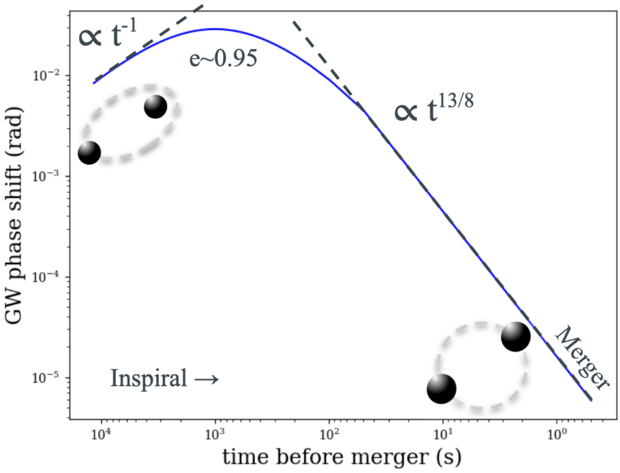

Figure 1.13: Illustration of the evolution of the GW phase shift in the eccentric (left) and circular limit (right).

A closed form for $d\phi(t)$ with arbitrary eccentricity does not exist, since there is no analytical solution for $e(t)$ (Peters, 1964). However, one can write $d\phi$ in terms of the eccentricity e of the inspiralling binary:

$$\begin{aligned}\Delta\phi(e) \approx \frac{288\sqrt{2}}{85^2 g(1)^{13/2}} \frac{c^9}{G^{9/2}} \times \frac{m_3}{R^2} \frac{r_0^{13/2}}{m_1^2 m_2^2 m_{12}^{3/2}} \\ \times\, e^{78/19}(1-e^2)^{1/2} g(e)^{13/2}.\end{aligned} \tag{1.16}$$

Here, r_0 is the pericentre distance of BH1-BH2 in their very first orbit, right after formation. The function $g(e)$ is given by

$$g(e) = \left(1 + 121e^2/304\right)^{870/2299}. \tag{1.17}$$

Having obtained Eq. 1.16 (Samsing et al., 2025), we are now equipped with a tool to calculate the GW phase shift of a BBH with *any* eccentricity, provided the outer orbit is circular. The outer orbit, however, is not necessarily circular as the 3-body interactions through which these mergers form naturally allow for arbitrary outer eccentricity (e.g. Portegies Zwart & McMillan, 2000; Samsing et al., 2014). A vital extension of our phase shift model is therefore to allow the outer orbit to also be eccentric. The study in which I do so is presented in Chapter 2, where I discuss the new unique features in the phase shift due to outer orbit eccentricity.

Eq. 1.16 and its eccentric equivalent allow us to understand how the phase shift depends on the parameters m_1, m_2, m_3, R, r_0 and e. Whether reality agrees with these dependencies, however, remains to be explored. The BH scatterings that produce these 3-body mergers can be highly chaotic and may be full of surprises. A deeper understanding requires testing our models against explicit binary–single scatterings. Fortunately, we can recreate these encounters on our computers with so-called *N-body simulations*. These simulations (in our case, $N = 3$) can accurately model the interaction between three BHs in a binary-single scattering by calculating numerically how their mutual forces evolve over time and eventually lead them to a 3-body merger. These simulations can also compute the GW phase shift numerically. Details on how N-body simulations work can be found in Appendix A. In Chapter 3, I present results from a study in which we simulated a population of binary-single scatterings and calculated their corresponding GW phase shift, aiming to identify the astrophysical configurations that maximise the phase shift.

Lastly, a vital piece to the puzzle is an investigation of the detectability of the phase shift. After all, in order to know whether this tool is a realistic way to probe the binary formation environment, it is important to quantify how well the outer orbital parameters (e.g. the tertiary mass m_3) can be constrained in detections of phase-shifted GW signals. Chapter 4 contains a parameter inference study in which we generated several phase-shifted GW signals and analyse how well a next-generation detector like ET can recover the outer orbital parameters.

Motivated by the open questions outlined above, I present below the concrete objectives of this thesis.

1. Explore the impact of eccentric outer orbits on the GW phase shift (Chapter 2).
2. Study the behaviour of the phase shift in realistic binary–single scatterings (Chapter 3).
3. Evaluate the extent to which the formation environment can be inferred in phase-shifted GW signals (Chapter 4).

Chapter 2

Eccentric features in the Gravitational Wave Phase of Dynamically Formed Black Hole Binaries

> *"Imagine you're Galileo and you don't know what the gravitational constant is."*
>
> – Conor Dyson

This chapter includes the article *"Eccentric features in the Gravitational Wave Phase of Dynamically Formed Black Hole Binaries"*, by Kai Hendriks, Lorenz Zwick, and Johan Samsing, published in *the Astrophysical Journal* 985, 252 (2025).

2.1 Abstract

We study the gravitational wave (GW) phase shift arising from centre-of-mass accelerations of binary black hole (BBH) mergers formed dynamically in three-body systems, where both the inner orbit of the merging binary and the outer orbit are eccentric. We provide a semi-analytical model and several analytical approximations that allow for fast evaluation of both the temporal evolution and the maximum value of the phase shift. The highest phase shifts occur when the binary merges close to the pericentre of the outer orbit, and can in this case be orders-of-magnitude larger compared to the circular limit. At high outer orbit eccentricities, the orbital curvature leaves distinct imprints onto the phase shift if the binary passes the outer pericentre during its inspiral. By comparing with phase shifts measured in numerical chaotic 3-body scatterings, we show that our model accurately describes the observed phase of dynamically assembled binary systems in realistic astrophysical scenarios, providing a way to directly determine their formation channel via single GW observations. Phase shifts produced in such environments may receive additional amplifications due to the tidal pull from the perturber onto the BBH.

2.2 Introduction

A variety of merging binary black holes (BBHs) has been observed through their emission of gravitational waves (GWs) with LIGO/Virgo/Kagra (LVK) (Abbott et al., 2023). Although the BBH masses (Abbott et al., 2019a, 2020a), spins (Zackay et al., 2019; García-Bellido et al., 2021), and orbital eccentricities (Abbott et al., 2019b; Romero-Shaw et al., 2021; Gayathri et al., 2022; Abac et al., 2024) have been measured, or at least constrained, the origin of these objects and binaries is still a major unsolved question. Some proposed formation environments include isolated binary stars (Dominik et al., 2012, 2013, 2015; Belczynski et al., 2016b,a; Silsbee & Tremaine, 2017; Murguia-Berthier et al., 2017; Rodriguez & Antonini, 2018; Schrøder et al., 2018; Iorio et al., 2023), dense stellar clusters (Portegies Zwart & McMillan, 2000; Lee et al., 2010; Banerjee et al., 2010; Tanikawa, 2013; Bae et al., 2014; Rodriguez et al., 2015; Ramirez-Ruiz et al., 2015; Rodriguez et al., 2016a,b,b; Askar et al., 2017; Park et al., 2017; Samsing, 2018; Samsing & D'Orazio, 2018; Samsing et al., 2020; Trani et al., 2021, 2022), galactic nuclei (GN) (O'Leary et al., 2009; Hong & Lee, 2015; VanLandingham et al., 2016; Antonini & Rasio, 2016; Stephan et al., 2016; Hoang et al., 2018; Hamers et al., 2018; Trani et al., 2019; Liu et al., 2019a; Liu & Lai, 2021; Atallah et al., 2023), active galactic nuclei (AGN) discs (Bartos et al., 2017; Stone et al., 2017; McKernan et al., 2018; Tagawa et al., 2020; Samsing et al., 2022; Trani et al., 2024b; Fabj & Samsing, 2024), single-single GW captures of primordial black holes (Bird et al., 2016; Cholis et al., 2016; Sasaki et al., 2016; Carr et al., 2016), and very massive stellar mergers (Loeb, 2016; Woosley, 2016; Janiuk et al., 2017; D'Orazio & Loeb, 2018). Generally, it has proven difficult to tell these different channels apart using GWs alone. However, studies have shown that different classes of channels share specific properties, e.g. dynamically formed BBH mergers will give rise to a significant fraction of eccentric mergers (e.g. Gültekin et al., 2006; Samsing et al., 2014; Samsing & Ramirez-Ruiz, 2017; Samsing & Ilan, 2018; Samsing et al., 2018b; Samsing, 2018; Samsing et al., 2018a; Samsing & D'Orazio, 2018; Rodriguez et al., 2018; Liu et al., 2019b; Zevin et al., 2019; Samsing et al., 2019, 2020), which is different from those forming through isolated binary evolution. The BBH spins (e.g. Kalogera, 2000; Rodriguez et al., 2016c; Liu & Lai, 2018), as well as the mass distribution (e.g. Zevin et al., 2017; Su et al., 2021) can also be used to disentangle different formation channels. While this is encouraging, the group of dynamically formed BBH mergers also consists of several different channels, with overlapping observed quantities. For example, GW captures forming in GN (e.g. O'Leary et al., 2009), hierarchical Lidov-Kozai-triple configurations (e.g. Hoang et al., 2018; Liu et al., 2019b), and few-body interactions in globular cluster (GCs) (e.g. Samsing, 2018) and AGNs (e.g. Samsing et al., 2022; Fabj & Samsing, 2024) all give rise to eccentric mergers with similar distributions.

One very interesting measure of the formation environment is how the presence of a third body induces a phase shift onto the gravitational waveform

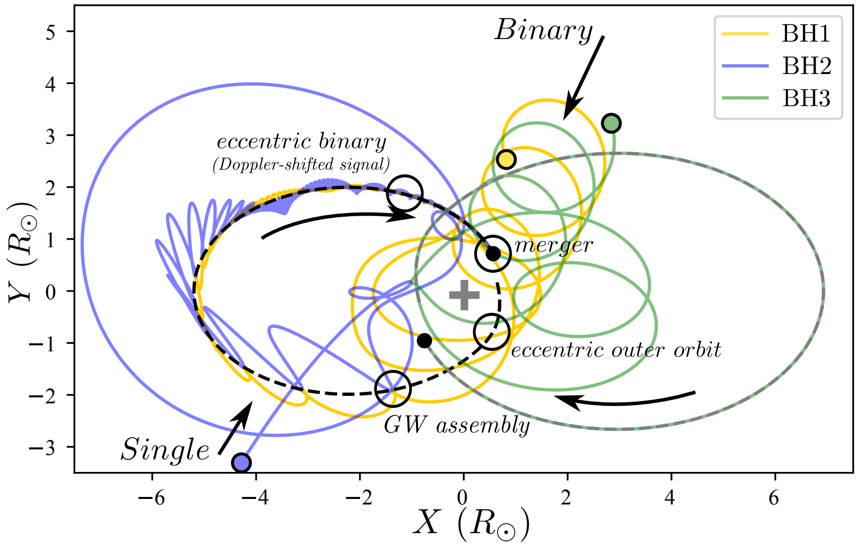

Figure 2.1: **Formation of a GW phase-shifted source.** Illustrative example of a scattering between a binary black hole (BH1, BH3) and an incoming single black hole (BH2) that results in a highly eccentric BBH merger (BH1, BH2), while all three objects are still bound to each other. The eccentric BBH merger therefore inspirals and merge on an eccentric orbit around the remaining BH3, which gives rise to a Doppler-shifted GW signal due to binary COM acceleration in the COM frame. This GW-shift can be detected, and will leave imprints on how the specific BBH assembly and merger takes place, thereby revealing the BBH origin. This is further illustrated in Fig. 2.2. In this example, we use $m_1 = 15M_\odot$, $m_2 = 5M_\odot$, and $m_3 = 15M_\odot$.

in the observer frame. In such a scenario, the BBH evolves while its COM is being accelerated. The acceleration causes a time-dependent Doppler shift in the gravitational waveform, which in principle can be measured and used to probe the exact dynamical environment within which the binary lives as it merges. Therefore, looking for GW phase shifts, or more generally environmental effects, could be the key to help us tell apart the large suit of sub-channels, provided they are present in the observable GW bands (e.g. Tiwari et al., 2024, 2025a).

As of now, this scenario has been looked at in the case of circular orbits for both the BBH itself (inner orbit) and its orbit around the perturbing BH (outer orbit) (Meiron et al., 2017), and a circular binary on an eccentric outer orbit (Robson et al., 2018). Recently, we extended this problem to the case of BBHs formed dynamically (Samsing et al., 2025). Here the BBH itself is eccentric and inspirals on a circular orbit around the third object, which naturally gives rise to more unique imprints in the gravitational waveform. In this present paper we take the next step and model the GW phase of a general eccentric BBH inspiralling on an eccentric outer orbit near another BH.

This generalisation is vital as it accurately represents the case for dynamically assembled BBH mergers (see e.g., Portegies Zwart & McMillan, 2000; Samsing et al., 2014; Rodriguez et al., 2016a,b; Askar et al., 2017; Samsing & D'Orazio, 2018; Liu & Lai, 2018; Hoang et al., 2018; Trani et al., 2022). An example is depicted in Fig. 2.1, that shows the formation of a BBH inspiral and merger formed through a chaotic scattering process between three black holes. These types of interactions are known to frequently take place in GCs and other dense environments, and have especially been suggested to be among the most reliable ways for forming BBH mergers with residual eccentricity across the observable GW bands (Samsing, 2018). Moreover, including and considering outer orbit eccentricity is not expected to just add a small perturbation to the problem, as the maximum GW phase shift scales as $\propto R^{-2}$, where R is the distance between the BBH and the third BH (Meiron et al., 2017; Samsing et al., 2025). This implies that if the BBH merges close to the pericentre of its outer orbit, the GW phase shift may increase dramatically compared to a circular outer orbit with the same period. This situation is in fact seen in Fig. 2.1, where *'merger'* takes place near pericentre of the outer orbit.

The aim of this paper is to investigate the GW Doppler shift and corresponding GW phase shift of an eccentric BBH on an eccentric orbit around a third BH, by quantifying effects that are unique to the outer orbit being eccentric. Effects for different outer orbit families have recently been explored using an expansion in acceleration (Tiwari et al., 2025a); In our present paper we expand on this, by further developing a semi-analytical method that solves for the full orbit from which we discover several new non-linear effects in the resultant GW phase shift.

The paper is organised as follows. We start in Sec. 2.3 by outlining our theory for how we calculate GW phase shifts in the general case where both the inner and outer orbits can be eccentric. This is followed by Sec. 2.4, where we explain the main characteristics and observable features of the eccentric outer orbit. In Sec. 2.5 we discuss implications in astrophysically relevant cases, where we highlight phase shifts in scatterings and the impact of tidal forces on the phase shift. We then conclude the study and provide future prospects in Sec. 2.6.

2.3 Theory

As described in Meiron et al. (2017); Samsing et al. (2025), the GW Doppler shift arising from the acceleration on an outer orbit can equivalently be viewed as the GW phase shift from Rømer delay (RD) between the binary trajectory and some non-accelerating reference trajectory. In Fig. 2.2 we show our setup in this framework. We depict in turquoise the trajectory of an initially highly (inner-orbit) eccentric BBH (BH1, BH2) that inspirals and merges on an eccentric (outer) orbit around BH3 (see also Fig. 2.1). Each of these BHs have a mass m denoted m_1, m_2 and m_3, respectively. We compare this to a fictional reference binary, shown in orange. This binary has exactly the same parameters (i.e. initial eccentricity, semi-major axis, time to coalescence, binary masses), but moves on a straight line with a constant velocity v_m that is equal to the tangential velocity of the perturbed binary at merger. Tracing these two paths back in time from merger, their gradual deviation is what gives rise to the time-dependent Rømer delay. If the distance between the two trajectories at some time t is given by $l(t)$ (red dashed line in Fig. 2.2), then their relative maximum Rømer delay, $\Delta t(t)$, is

$$\Delta t(t) = l(t)/c, \tag{2.1}$$

where c is here the speed of light. As shown in the bottom sketch of Fig. 2.2, the difference in arrival time between the GWs from the two trajectories induces a phase shift onto the gravitational waveform.

It is important to realise that the Δt shown in Fig. 2.2 is the maximum time delay between the two trajectories. In reality, an observer only sees the projection of Δt in their own line-of-sight (e.g. Meiron et al., 2017; Samsing et al., 2025). However, in this work, we solely focus on the maximum possible phase shift that we denote simply by $d\phi$; factoring in the trivial observer dependent factor will be investigated in later work. Other sources of dephasing in gravitational waveforms in dynamically assembled systems includes General Relativistic (GR) effects, such as Shapiro delay (Backer & Hellings, 1986), gravitational redshift (Meiron et al., 2017; Chen, 2021), and gravitational lensing (e.g. Wang et al., 1996; Takahashi & Nakamura, 2003; Ezquiaga et al., 2021; Lo et al., 2025), as well as special relativistic effects (Torres-Orjuela et al., 2019; Yan et al., 2023), aberration (Torres-Orjuela et al., 2020), and classical tidal effects (Samsing et al., 2025). Relevant discussions of similar setups can be found in (e.g. Yunes et al., 2011; Inayoshi et al., 2017b; Robson et al., 2018; Chamberlain et al., 2019; Randall & Xianyu, 2019a; Wong et al., 2019; Tamanini et al., 2020; D'Orazio & Loeb, 2020; Toubiana et al., 2021; Strokov et al., 2022; Xuan et al., 2023; Laeuger et al., 2024; Tiwari et al., 2024).

In the sections below we start by deriving our semi-analytical description for the Rømer time delay (Sec. 2.3.1), as well as our expression for the corresponding GW phase shift (Sec. 2.3.2). Subsequently, in Sec. 2.3.3 we lay out the general numerical procedure to obtain these quantities. Finally, we provide analytical approximations to the phase shift and illustrate how they can be used to estimate the GW phase shift created for outer eccentric orbits when the observational time window is relatively small (Sec. 2.3.4).

2.3.1 Rømer Time Delay

Using Kepler's Laws, one can use geometrical arguments and standard mechanics to derive the Rømer time delay and corresponding phase shift, as we illustrate in the following. The analytical solution to the case where the inner orbit is eccentric and the outer orbit is circular was presented in Samsing et al. (2025), and we therefore go right into presenting the solution for the RD in the more general case of an eccentric outer orbit.

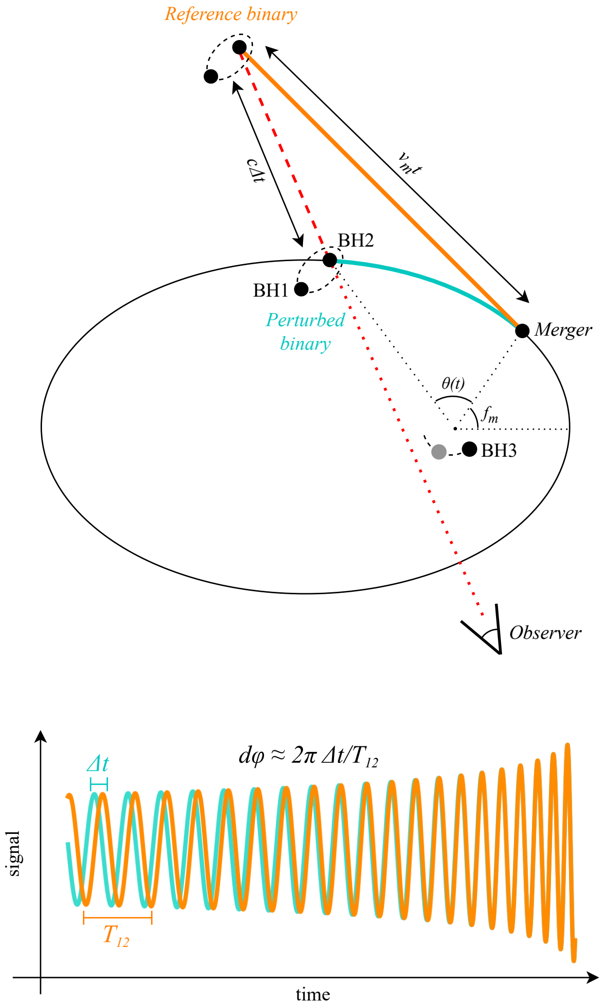

Figure 2.2: **Illustration of our setup**. *Top:* The turquoise curve represents the real trajectory of the COM of an eccentric binary (BH1, BH2), whose COM is on an eccentric orbit around a perturber (BH3). In orange, we show the trajectory of the same binary, if it had evolved in isolation. The reference binary has a constant speed v_m equal to the orbital speed of the COM of the perturbed binary at merger, which happens at true anomaly f_m. A Rømer delay Δt arises due to the difference in light travel time between the two scenarios towards an observer, who is depicted in the bottom right. *Bottom:* schematic representation of how the Rømer delay is imprinted in the gravitational waveform. The perturbed waveform receives a time-dependent Doppler shift with respect to its isolated counterpart, which we can turn into a phase shift by equating it with the orbital period of the binary (BH1, BH2) at the same point in time: $d\phi \approx 2\pi\Delta t/T_{12}$.

For deriving the RD Δt we start by calculating the distance between the the turquoise perturbed binary COM and the orange reference binary COM at a given time t (see Fig. 2.2), defined as the time in the restframe of the 3-body system. The fact that the position and evolution of a Keplerian eccentric orbit cannot be written in closed form, makes the simple geometrically description slightly more complex compared to the circular case.

In this work we find it convenient to split up the true anomaly f in two parts,

$$f(t) = \theta(t) + f_m, \tag{2.2}$$

where f_m is the angle at which the binary merges and $\theta(t)$ is the angle between the position vector of the turquoise binary COM at time t and its position vector at merger (see Fig. 2.2). Another important quantity to note is the distance between the BBH and the third object, $r(f)$, which is a function of f as given by,

$$r(f) = \frac{a_{\text{out}}(1 - e_{\text{out}}^2)}{1 + e_{\text{out}} \cos f}, \tag{2.3}$$

where a_{out} and e_{out} denote the semi-major axis and eccentricity of the BBH outer orbit, respectively. With this set of equations we are now in a position to calculate the distance l between the reference binary undergoing a straight line motion with velocity v_m, and the perturbed or true binary moving on the eccentric outer orbit. Using standard geometry the distance l is at time t given by,

$$\begin{aligned} l(t) = \mu \bigg[& [r(f_m)\cos(f_m) + v_{m,x}t - r(f)\cos(f)]^2 \\ & + [r(f_m)\sin(f_m) + v_{m,y}t - r(f)\sin(f)]^2 \bigg]^{1/2} \qquad (2.4) \\ = \mu \bigg[& v_m^2 t^2 \\ & - 2t\bigg[v_{m,x}(r(f)\cos(f) - r(f_m)\cos(f_m)) \end{aligned}$$

$$+ v_{m,y}(r(f)\sin(f) - r(f_m)\sin(f_m)))\Big]$$

$$+ r^2(f_m) + r^2(f) - 2r(f_m)r(f)\cos(f - f_m)\Big]^{1/2},$$

where the quantities $v_{m,x}$ and $v_{m,y}$ are the x, y velocity components at merger, f depends on t through Eq. 2.2, and $\mu = m_3/m_{123}$, where $m_{123} = m_1 + m_2 + m_3$. In the rest of the paper, we will refer to the quantity $r(f_m)$, i.e. the distance to the perturber at merger, simply as r_m. These quantities relate to the angular and radial velocities of the binary COM at phase f,

$$v_{\text{ang}}(f) = \frac{\sqrt{Gm_{123}a_{\text{out}}(1 - e_{\text{out}}^2))}}{r(f)}, \tag{2.5}$$

and

$$v_{\text{rad}}(f) = e_{\text{out}}\sin(f)\sqrt{\frac{Gm_{123}a_{\text{out}}}{(1 - e_{\text{out}}^2)}}, \tag{2.6}$$

as

$$\vec{v}(f) = -\begin{pmatrix} v_{\text{ang}}\sin(f) - v_{\text{rad}}\cos(f) \\ -v_{\text{ang}}\cos(f) - v_{\text{rad}}\sin(f) \end{pmatrix}. \tag{2.7}$$

Here, we explicitly mention that $\vec{v}_m = \vec{v}(f_m)$.

Because the outer orbit is eccentric, we cannot obtain an analytical relation between f and t. Therefore, we calculate $l(t)$ numerically using the equations above. From this calculation of the distance l between the two trajectories, the RD can now be calculated using Eq. 2.1.

2.3.2 Gravitational Wave Phase shift

As shown in Samsing et al. (2025), the maximum GW phase shift at a given time t, $d\phi(t)$, evaluated in the observer frame can be approximated by the maximum RD, Δt, divided by the inner orbital time of the BBH, T_{12}, times

2π to get it in radians,

$$d\phi(t) \approx 2\pi \frac{\Delta t(t)}{T_{12}(t)} = \frac{2\pi}{c} \frac{l(t)}{T_{12}(t)}. \tag{2.8}$$

This is the relevant factor to consider in relation to observational constraints (e.g. Meiron et al., 2017).

To derive $d\phi$ for outer eccentric orbits we have the RD Δt from Eq. 2.4 that can be evaluated at time t. The corresponding orbital time T_{12} can also be defined at time t, which follows from Kepler's Law,

$$T_{12} = \frac{2\pi}{\sqrt{G(m_1 + m_2)}} a^{3/2}, \tag{2.9}$$

where a, and associated e, refer to the semi-major axis and the eccentricity of the merging BBH inner orbit, respectively. For solving the evolution, from assembly to merger of the BBH due to GW angular momentum and energy losses as it spirals in, we use the relation for $a(e)$ presented in Peters (1964) (which, hereafter, we will refer to as Peters64),

$$a(e) = a_0 \frac{g(e)}{g(e_0)}, \tag{2.10}$$

where

$$g(e) = \frac{e^{12/19}}{1 - e^2} \left(1 + \frac{121}{304} e^2\right)^{870/2299}, \tag{2.11}$$

and a_0 and e_0 are the semi-major axis and eccentricity of the binary at some reference point in their evolution.

Note that in order to calculate the phase shift we need $\Delta t(t)$ and T_{12} in terms of either t or e. While a closed form for $e(t)$ does not exist, an expression for $t(e)$ is given in Peters64. However, this form is somewhat inaccurate for estimating the correct inspiral time when the binary is highly eccentric. The general problem relates to the fact that the orbital elements, a and e, are defined using Newtonian prescriptions, which break down especially for eccentric BBH inspirals where these quantities not only are drastically changing as a function of time, but also ill-defined. Instead we here make use of the fitting function presented in (Zwick et al., 2020; Zwick et al., 2021), which provides a more accurate estimate for the merger time than the Peters64 solution. The fit takes the form

$$\begin{aligned} t_c = & \frac{5c^5(1+q)^2}{256G^3m_{12}^3q}\frac{a(e)^4}{f(e)}8^{1-\sqrt{1-e}}\exp\left(\frac{2.8r_S}{a(e)(1-e)}\right) \\ & \times\left\{1+\left[-1+\exp\left(\frac{2.2r_S}{a(e)(1-e)}\right)\right.\right. \\ & \qquad \left.+\left(\frac{3.8r_S}{a(e)(1-e)}\right)^{3/2}\right](1-e)^2 \\ & \qquad \left.-\left(\frac{3.8r_S}{a(e)(1-e)}\right)^{3/2}(1-e)\right\}, \end{aligned} \tag{2.12}$$

where $m_{12} = m_1 + m_2$, $q = m_2/m_1 \geq 1$, $r_S = 2G(m_1 + m_2)/c^2$ and

$$f(e) = \left(1 + \frac{73}{24}e^2 + \frac{37}{96}e^4\right)(1-e^2)^{-7/2}. \tag{2.13}$$

The relation $a(e)$ from Peters64 given by Eq. 2.10, has been shown to still provide an accurate description, and we therefore continue using this throughout this work.

2.3.3 Numerical Procedure

Here we briefly lay out the numerical procedure we follow to calculate the phase shift $d\phi$ in our setup. Our model requires a total of 8 inputs: 4 from for the inner orbit BBH evolution (m_1, m_2, a_0, e_0), where a_0, e_0 here refer to the initial values right after assembly, and 4 for the outer orbit evolution of the BBH around the perturber $(m_3, f_m, a_{\mathrm{out}}, e_{\mathrm{out}})$. First we derive the inner orbital evolution of the inspiralling BBH.

- We first make an array of values for e ranging from e_0 all the way to $e = 0$, from which we can make an array for $a(e)$ using Eq. 2.10.

- With our derived array $a(e)$ we then calculate the corresponding BBH inner orbital time T_{12}, given by Eq. 2.9.

- We then compute the array for the corresponding merger time t_c given by Eq. 2.12.

For estimating the phase shift, we have to couple this procedure with the outer orbital evolution of the BBH around the perturber.

- We first choose orbital elements for the (non-decaying) outer orbit, $a_{\rm out}$ and $e_{\rm out}$, and an angular position for where the merger takes place, f_m.

- The computed array of the BBH merger time, t_c (from the inner binary as described above) is then used with $a_{\rm out}$, $e_{\rm out}$, and f_m, to numerically obtain an array for the corresponding true anomaly f.

- From this we now have the components to compute the distance $l(t)$, defined in Eq. 2.4, from which we find the maximum RD given by Eq. 2.1.

- Finally, we now have matching arrays with Δt and orbital time T_{12}, as a function of either time t, orbital eccentricity e, or true anomaly f. We then calculate the maximum GW phase shift $d\phi$ given by Eq. 2.8.

2.3.4 Analytical Approximations

Before we move to the main results derived from our procedure outlined above, we first consider a few highly useful and general approximations to the GW phase shift that allow one to estimate its magnitude analytically and corresponding relevant scalings. We especially describe how these can be used for fast estimations of the phase shift for eccentric BBH mergers formed during chaotic few-body interactions, which are being explored both in controlled experiments (e.g. Samsing, 2018; Samsing et al., 2025) and in MC codes such as CMC (Kremer et al., 2020) where merger statistics are based on millions of scatterings.

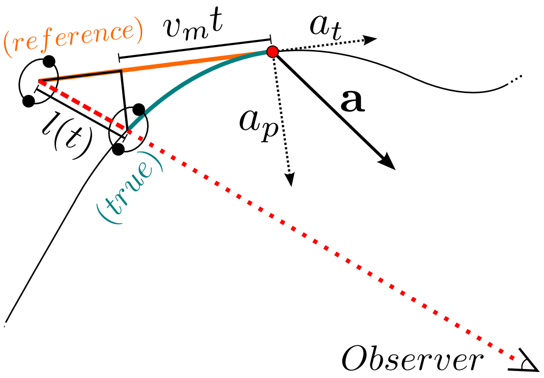

Figure 2.3: **Binary undergoing accelerated motion.** Schematic depicting a binary with an accelerated centre of mass (turquoise line) with respect to an inertial reference binary (orange line). The presence of curvature in the binary's path creates a time varying Doppler shift that influences its orbital frequency, as measured by an observer along a given line of sight (dotted red line).

Below we first present an analytical approximate solution to the general case of an inspiralling eccentric BBH moving on an arbitrary trajectory, while being subject to an arbitrary acceleration vector (for recent work on circular binaries, see also Vijaykumar et al., 2023; Tiwari et al., 2024). We then consider solutions specific to inner and outer eccentric orbits applicable to PN N-body studies.

Phase Shift from a General Acceleration

We start by considering the case of a BBH moving on an arbitrary trajectory, as shown in Fig. 2.3. At the point of merger the BBH has a velocity v_m and is subject to a general acceleration $\mathbf{a}$. While the velocity vector is tangential to the trajectory of the BBH, the acceleration vector does not have to be either parallel or perpendicular to the the trajectory. In a circular motion, the acceleration vector will be perpendicular to the velocity vector, but this is not the case for e.g. a simple eccentric orbit, where the velocity- and the acceleration vectors only are perpendicular to each other at peri- and apocentre. The question is what the maximum phase shift $d\phi$ can be for such a general trajectory and acceleration (see also Tiwari et al. (2025a)). We here estimate this to linear order, where we assume the acceleration and velocity is constant near the point of merger. As shown in Samsing et al. (2025), the maximum value of the phase shift when the BBH inspirals with non-zero inner orbit eccentricity, e.g. without taking into account the observer position, will arise close to merger, which justifies this assumption.

Using the notation from Fig. 2.3, we first estimate the distance l, i.e. $l = c\Delta t$ as shown in Fig. 2.2, between the reference trajectory and the real trajectory while taking into account both the tangential- and the perpendicular acceleration components,

$$l(t)^2 = \left(a_t t^2/2\right)^2 + \left(a_p t^2/2\right)^2 = |\mathbf{a}|^2 \left(t^2/2\right)^2, \tag{2.14}$$

leading to

$$l(t) = \frac{1}{2}|\mathbf{a}|t^2. \tag{2.15}$$

Using the general expression for $d\phi$ given by Eq. 2.8, one sees that $d\phi$ for an inspiralling BBH on an arbitrary orbit subject to a general acceleration vector $\mathbf{a}$ near merger is

$$d\phi \approx \frac{\pi}{c}\frac{|\mathbf{a}|t^2}{T_{12}}. \tag{2.16}$$

This can easily be evaluated for any system, including N-body systems, which allows for a fast phase shift estimation as we will further explain in Sec. 2.3.4 below.

Circular Approximation

The approximation above is at the linear level. However, when considering the specific case of a BBH moving on an eccentric orbit it is possible to provide a slightly more accurate, but still fast, estimate by approximating the trajectory by a circle around the point of merger instead of a line. For this, we continue under the assumption that the BBH is moving on a circle that is tangent to the point of merger with a radius corresponding to the distance between the BBH and the three-body COM, μr_m, and effective velocity v

defined as,

$$v = \sqrt{Gm_{123}/r_m}. \tag{2.17}$$

By now defining the angle θ to be the angular evolution of the BBH on that circle,

$$\theta(t) = vt/r_m, \tag{2.18}$$

the RD is found in this approximation using standard geometry (see Samsing et al. (2025) for further details),

$$\begin{aligned}\Delta t(t) = \frac{2\mu r_m}{c}&[(\theta/2)^2 + \sin^2(\theta/2)\\ &- 2(\theta/2)\sin(\theta/2)\cos(\theta/2)]^{1/2}.\end{aligned} \tag{2.19}$$

By now substituting this relation into Eq. 2.8, one finds

$$\begin{aligned}d\phi \approx 2\frac{\sqrt{Gm_{12}}\mu r_m}{a(e)^{3/2}}&\left[\frac{Gm_{123}}{4r_m^3}t_c(e)^2 + \sin^2\left(\sqrt{\frac{Gm_{123}}{r_m}}\frac{t_c(e)}{2r_m}\right)\right.\\ &- \sqrt{\frac{Gm_{123}}{r_m}}\frac{t_c(e)}{r_m}\sin\left(\sqrt{\frac{Gm_{123}}{r_m}}\frac{t_c(e)}{2r_m}\right)\\ &\left.\times\cos\left(\sqrt{\frac{Gm_{123}}{r_m}}\frac{t_c(e)}{r_m}\right)\right]^{1/2},\end{aligned} \tag{2.20}$$

where t_c is given by Eq. 2.12. If one uses the eccentricity as evolution factor, one can derive $d\phi(e)$ in closed form for any value of e as described in the following.

Fast Linear Approximation

The fastest estimator for the maximum phase shift $d\phi$ can be calculated using Eq. 2.16 with

$$|\mathbf{a}| = \frac{Gm_3}{r_m^2} \tag{2.21}$$

from which it directly follows,

$$\begin{aligned} d\phi(e) &\approx \frac{1}{2}\frac{G^{3/2}}{c}\frac{m_3 m_{12}^{1/2}}{r_m^2}\frac{t(e)^2}{a(e)^{3/2}} \\ &= \frac{1}{2}\frac{G^{3/2}}{c} m_3 m_{12}^{1/2} \\ &\quad \times \left(\frac{1+e_{\text{out}}\cos f_m}{a_{\text{out}}(1-e_{\text{out}}^2)}\right)^2 \frac{t(e)^2}{a(e)^{3/2}}, \end{aligned} \tag{2.22}$$

where in the last equality we have made the relation to the orbital elements describing the eccentric outer trajectory of the BBH relative to the single BH. Note that this equation also can be deduced from Eq. 2.19, by taking the small angular limit $\theta << 1$. One general result that follows from this is that the maximum phase shift, also in this outer orbit eccentric case, scales $\propto 1/{r_m}^2$, i.e. the closer to pericentre the merger happens, the higher the phase shift. This is one of the main reasons and motivations to study the outer eccentric case as we do here.

While one can substitute a, e, and t in the above equations, it is not easy to read off the maximum of $d\phi$. However, by combining this linear approximation and using Peters64 for both the inspiral time t and for $a(e)$ it becomes possible (Samsing et al., 2025), even here in the more general case of an outer eccentric orbit. Following this approach, we now start by substituting t in Eq. 2.22 with the approximative estimator given by Peters64,

$$t_c = \frac{3/85}{c^5/G^3}\frac{a^4}{m_1 m_2 m_{12}} \times (1-e^2)^{7/2}. \tag{2.23}$$

The reason why we use this expression here instead of the fit Eq. 2.12 is that this equation, despite being slightly less accurate, allows for direct estimation of the binary eccentricity at which the maximum phase shift occurs. This then results in an analytical expression for the maximum phase shift and its relevant scalings of the problem, which is extremely valuable for studies with e.g. N-body simulations containing millions of few-body interactions and mergers.

For $a(e)$ we use Eq. 2.10 and Eq. 2.11 that in the limit where the BBH is assembled with a high initial eccentricity, e_0, can be written as (see Samsing et al., 2025),

$$a(e) \approx \frac{2r_0 e^{12/19}}{(1-e^2)} \frac{h(e)}{h(1)}, \; (e_0 \approx 1), \tag{2.24}$$

where r_0 is the initial pericentre distance at assembly of the inspiralling BBH and

$$\begin{aligned} h(e) &= \left(1 + \frac{121}{304}e^2\right)^{870/2299} \\ &= g(e)\frac{1-e^2}{e^{12/19}}. \end{aligned} \tag{2.25}$$

The input r_0 is well defined and easy to estimate, in contrast to a_0 and e_0. Combining these relations, we reach the following relation,

$$\begin{aligned} d\phi(e) \approx & \frac{288\sqrt{2}}{85^2 h(1)^{13/2}} \frac{c^9}{G^{9/2}} \times \frac{m_3}{r_m^2} \frac{r_0^{13/2}}{m_1^2 m_2^2 m_{12}^{3/2}} \\ & \times e^{78/19}(1-e^2)^{1/2} h(e)^{13/2}. \end{aligned} \tag{2.26}$$

The maximum value of $d\phi$ can now easily be found by maximizing the function

$$F(e) = e^{78/19}(1-e^2)^{1/2} h(e)^{13/2}, \tag{2.27}$$

from which one finds

$$e_m = \sqrt{2\left(\sqrt{391681} - 115\right)/1213} \approx 0.92, \tag{2.28}$$

where e_m denotes the value that maximizes $F(e)$ and thereby $d\phi$. From this we conclude that the maximum possible value for $d\phi$ for a dynamically assembled BBH that mergers at a distance r_m from a perturber can be put in closed form as,

$$\begin{aligned} d\phi_{\max} \approx & \frac{288\sqrt{2}}{85^2 h(1)^{13/2}} \frac{c^9}{G^{9/2}} \times \frac{m_3}{r_m^2} \frac{r_0^{13/2}}{m_1^2 m_2^2 m_{12}^{3/2}} \\ & \times e_m^{78/19}(1-e_m^2)^{1/2} h(e_m)^{13/2}, \end{aligned} \tag{2.29}$$

with $e_m \approx 0.92$. One should note here that this maximum value might not be in the observable band. As was proven in Samsing et al. (2025), the initial BBH peak frequency $f_0(r_0)$ needs to be near the observable band for the phase shift effects to be large enough to be observable, i.e. for these calculations to be relevant for e.g. LIGO, f_0 at assembly has to be $\sim$ 10 Hz or above. It can be lower, but then the phase shift will have decreased significantly before reaching the observable band. For example, in the limit where the BBH is assumed circular, $d\phi \propto f^{-13/3}$, i.e. it rapidly drops as the frequency increases.

2.3.5 Limitations and Conclusions

Both the linear and the circular approximations from above are based on assumptions of constant velocity and acceleration during the time over which the phase shift is observed, which are generally justified. However, in some cases, especially relevant for the LISA mission, the observational time window can be comparable or even longer than the outer orbital time, which leads to periodic features from the time-evolving Doppler shift that will naturally enter the GW waveform and phase shift. In our considered case, where dynamically assembled binaries are often evolving along highly eccentric outer orbits, other effects can occur on much smaller timescales, as the acceleration will vary greatly over the orbit from pericentre to apocentre. Most notably, if the BBH happens to pass near pericentre at the time of observation, one expects large non-linear dephasing effects on a timescale set by the time of pericentre passage, which can be orders-of-magnitude smaller than the outer orbital time. Such effects are not captured by our approximations from this section, but below we will study such encounters in much more detail.

2.4 Phase Shift Characteristics

Here, we explore the unique features arising in the GW phase shift from changing the outer orbit eccentricity e_{out}, and the angular position at which merger takes place, f_m, for chirping and merging eccentric BBHs. For the illustrative examples below, unless otherwise stated, we consider cases for which $m_1 = m_2 = 5M_\odot$, $m_3 = 100M_\odot$, $a_0 = 1.3R_\odot$, $e_0 = 0.999$, and $a_{\rm out} = 30R_\odot$. These values for the inner BBH correspond to a GW burst source with peak frequency $f_{p,GW} \approx 32$Hz.

2.4.1 Imprints of Orbital Eccentricity

In Fig. 2.4 we show the BBH evolution along outer orbits with a representative moderate eccentricity of 0.6, as well as with reference binary tracks, for 4 different values of f_m. The corresponding GW phase shift, $d\phi$, as a function of time to merger, is depicted in the lowest panel of the figure. For all these computations we follow our procedure outlined in Sec. 2.3.3.

The general shapes of the curves in Fig. 2.4 are reminiscent of the circular case (Samsing et al., 2025), i.e., the peak that is present in the phase shift of circular outer orbits also persists here in the eccentric case. However, the evolution and peak value of $d\phi$ clearly vary with f_m, as the value of f_m maps to r_m that determines the magnitude of the phase shift, $d\phi_{\rm max} \propto r_m^{-2}$, which follows from Eq. 2.29. This also implies that when the outer orbit is eccentric, the maximum value $d\phi_{\rm max}$ will change by a factor set by the pericentre and apocentre distances, such that

$$\frac{d\phi_{\rm peri}}{d\phi_{\rm apo}} \approx \frac{(1+e)^2}{(1-e)^2}, \tag{2.30}$$

and correspondingly by a factor of $1/(1-e)^2$ compared to if the BBH was circular with radius $a_{\rm out}$.

Note how, for the cases $f_m = -0.75\pi$ and $f_m = 0.75\pi$, the distance at merger between the binary and the third object is the same. Therefore these cases have an almost identical peak phase shift. However, their phase shifts diverge at earlier times because of the differing ellipse curvatures along the orbit.

In summary, the leading order effect from introducing a small to moderate eccentricity of the outer orbit, is a change in the maximum phase shift $d\phi_{\rm max}$. Generally, as the distance r between the binary and third object at the point

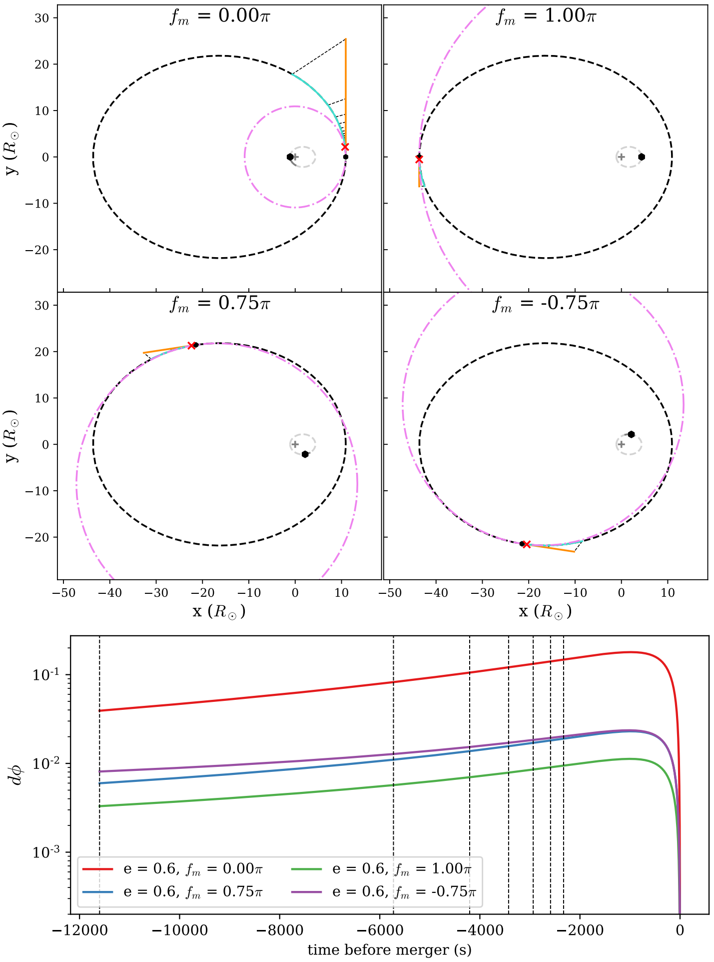

Figure 2.4: **GW phase shifts from eccentric orbits.** *Top 4 panels:* Trajectories of four different GW phase shift-inducing scenarios, each with different f_m. The eccentricity of the outer orbit is set to $e_{\mathrm{out}} = 0.6$. The turquoise curve is the true trajectory of the binary (merging at the smaller black dot at the corresponding f_m) on an eccentric orbit around BH3 (the larger black dot). The reference trajectory in isolation is depicted by the straight orange line. The dashed straight lines represent the distance $l(t)$ between the two trajectories which is used to calculate the time delay according to $\Delta t(t) = l(t)/c$. The red cross corresponds to the place on the orbit where $d\phi_{\mathrm{max}}$ occurs, which is quite close to merger in all cases. We also show in pink the circle with radius equal to μr_m, which we use for our circular approximation. The black and grey dashed ellipses depict the Keplerian orbits of the binary COM and BH3, respectively. *Bottom panel:* the phase shift $d\phi$ as a function of time for each scenario. The black dashed lines in this panel represent the temporal location of the same lines in the trajectory plots.

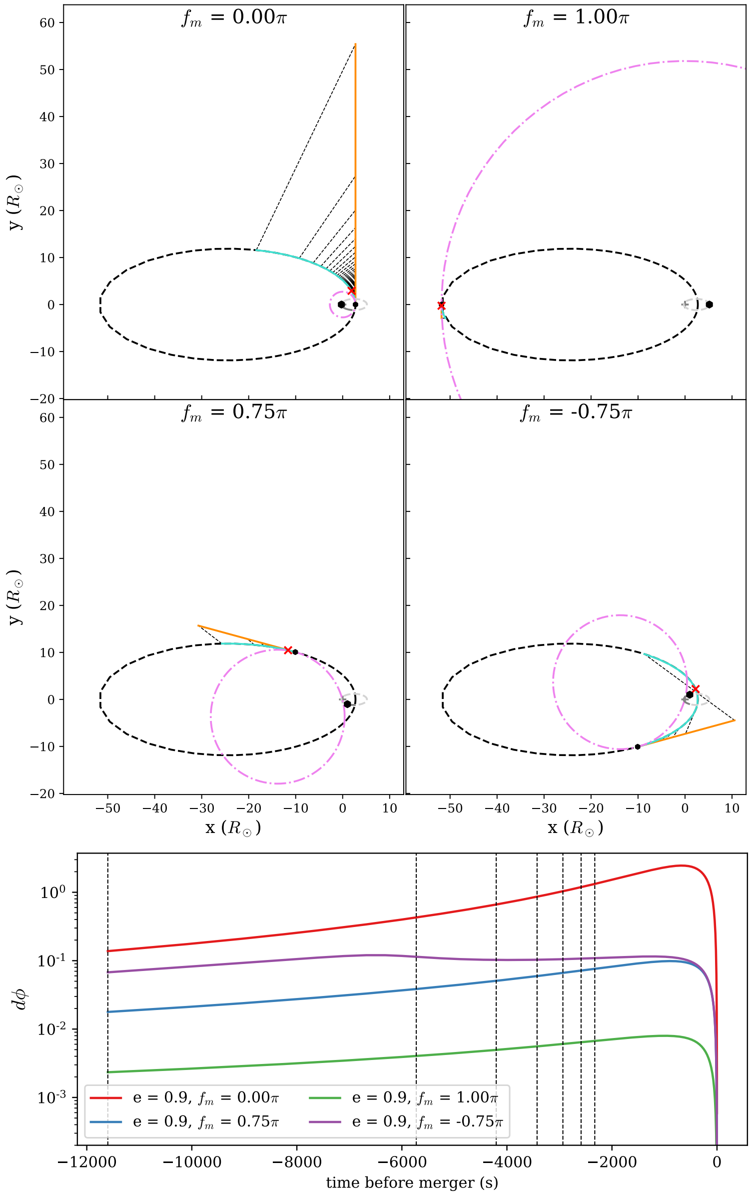

Figure 2.5: **GW phase shifts from eccentric orbits.** Similar to Fig. 2.4, but with the eccentricity of the outer orbit set to $e_{\mathrm{out}} = 0.9$.

of merger increases, the peak value decreases as $\propto 1/r^2$. Note here that there will be further dynamically constraints on the BBH if the outer orbit eccentricity increases. We will touch upon this in Sec. 2.5.2.

2.4.2 Strong Effects and Secondary Peaks

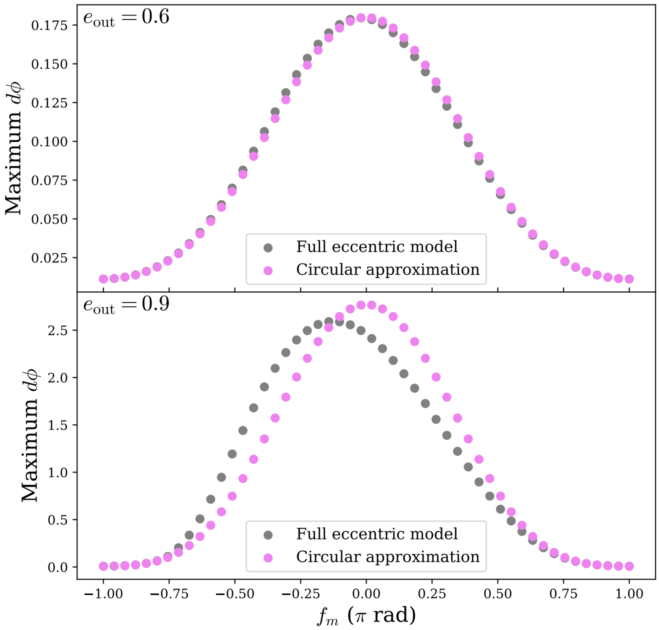

Figure 2.6: **Maximum GW phase shift.** *Top*: In grey, we show the dependence of $d\phi_{\rm max}$ on the true anomaly at merger f_m. The pink curve represents our circular approximation (Eq. 2.20). The outer eccentricity is 0.6. *Bottom*: the same relation, this time with $e_{\rm out} = 0.9$.

Having studied features of the moderately eccentric case, we now move to the case where the outer orbit has a significant eccentricity, which we show will give rise to additional unique imprints on the GW phase shift. For this, we start by considering Fig. 2.5, which shows the trajectories of the BBH (with respect to the isolated case) at four different value of f_m, with an outer eccentricity of 0.9.

We focus here on the new qualitative features that go beyond the expectations from the $1/r_m^2$ scaling. For highly eccentric outer orbits, the maximum phase shift is achieved for binaries that merge shortly after their pericentre passage. As an example, a binary merging at $f_m \sim -0.2\pi$ passes the high curvature region at pericentre, changing direction rapidly. This change in direction, combined with a high orbital velocity, causes higher possible phase shifts as opposed to a binary simply merging at pericentre ($f_m = 0$). In the regions $-0.75\pi < f_m < -0.25\pi$ and $0.25\pi < f_m < 0.75\pi$, the circular approximation respectively under- and overestimates the maximum phase shift due to the extra ac- and deceleration of the binary from the strong curvature. This is further outlined in Fig. 2.6.

More characteristics unique to highly eccentric outer orbits are visible in Fig. 2.5. The case $f_m = -0.75\pi$ has two peaks: a main peak that occurs at around the same time as for the other curves, and a secondary peak appearing at earlier times. In Fig. 2.9 we schematically depict this scenario, where in orange we show the trajectory of a binary that produces a single-peak phase shift, and in pink a case that has two peaks. The two peaks can be understood in the following way:

- the main peak, close to merger, is simply the generic shape of the phase shift of eccentric inspirals (Eq. 2.26);
- the secondary peak, earlier in the inspiral, occurs when the binary passes the pericentre of the outer orbit. During this passage, the binary COM changes direction rapidly on the orbit and its path therefore deviates significantly from a constant-speed reference binary. This induces a boost in Rømer delay, resulting in an additional peak in the GW phase shift.

There is a preferred region on the outer orbit for the secondary peaks to appear. Three conditions have to be satisfied:

1. The binary COM should pass the outer orbit pericentre during its inspiral;
2. The binary COM should not pass the pericentre too shortly before it merges. In that case, the two peaks would merge into one;
3. The binary COM should not pass the pericentre too long before it merges. In that case, pericentre passage would occur when the binary orbital

period T is too large for the boost in Δt to generate an extra peak in $d\phi = 2\pi\Delta t/T$.

With our choice of parameters, the region in which the secondary peak occurs is $-0.8\pi \lesssim f_m \lesssim -0.6\pi$. We stress that this is an important feature of a system like this, as it is a direct mapping of the environment in which the BBH merges. It only occurs when e_{out} is high and in a specific section of the outer orbit, thus a possible observation of this would directly pin down properties of this BBH formation channel.

In Fig. 2.7 we show in more detail how the GW phase shift curves vary around pericentre with changing f_m, where each coloured line corresponds to a different value of f_m, as illustrated in the upper left insert figure for each panel (f_m for a given coloured line is where the line ends at the outer orbit shown with a black dashed line). In the top panel, we see that curves with the highest peak in the $e_{\text{out}} = 0.6$ scenario are green/light blue, which correspond to mergers near pericentre. The colour of the highest peak at $e_{\text{out}} = 0.9$ is a deeper blue, corresponding to mergers just after pericentre (at $f_m \sim -0.2\pi$). The bottom panel visualises how the secondary peak evolves. As we move from pink into blue, the merger happens increasingly close to pericentre, so the secondary peak slowly melts together with the main peak.

Fig. 2.8 visualises the shape of $d\phi$, including the changing location of the maximum, for a full range of f_m at a high outer eccentricity. Each vertical line in this plot represents the GW phase shift path of a binary merging at a specific f_m, where the binary evolves as a function of true anomaly f from the top and down. The colour represents the (normalised) phase shift at each f in the orbit. It is clearly seen how the evolving GW phase shift depends on how and where the BBH merges on the outer eccentric orbit. In particular, between $f_m \sim -0.75\pi$ and $f_m \sim -0.65\pi$ the presence of the secondary peak is clearly visible.

To sum up, outer orbits with high eccentricities give rise to extra features and effects that are not present otherwise. Firstly, an increased eccentricity results in a much closer encounter at pericentre which leads to significantly larger phase shifts. Additionally, strong curvature effects around pericentre

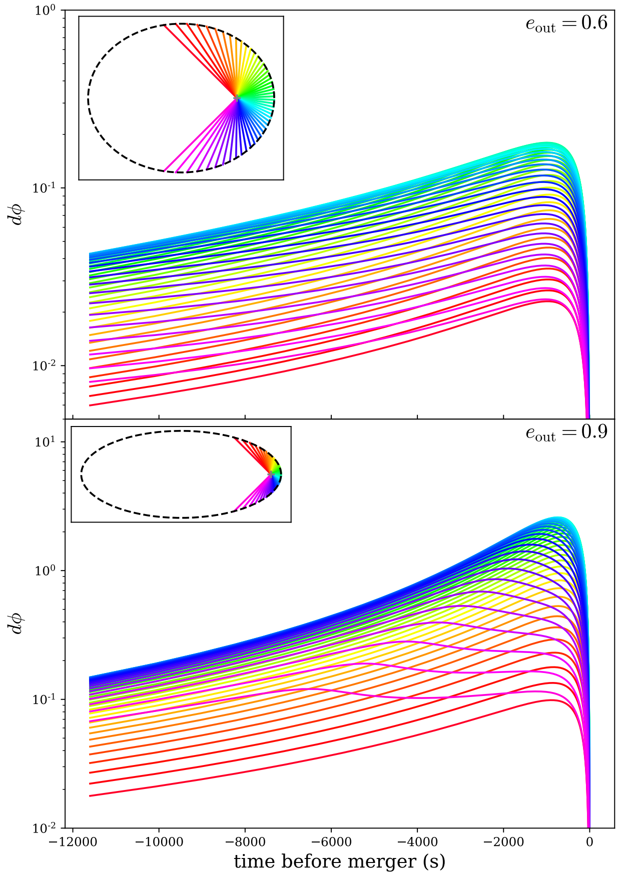

Figure 2.7: **GW phase shift, eccentricity, and double peaks.** The phase shift $d\phi$ as a function of time, for a range of f_m close to pericentre ($-0.75\pi \leq f_m \leq 0.75\pi$). The ellipse in the top left corner illustrates the outer eccentric orbit. Every coloured line represents a certain f_m, where the location of merger is the point where that line intersects with the ellipse. The colour of each line in the main plot corresponds to the colour of the lines within the ellipse. *Top:* We show the results for $e_{\rm out} = 0.6$. *Bottom:* Results for $e_{\rm out} = 0.9$.

leave their imprint on the shape of the phase shift: (i) The largest possible phase shift does not occur when the binary merges at pericentre, but slightly beyond (at $f_m \sim -0.2\pi$ in our example) due to the extra curvature effects due to passing pericentre, and (ii) a secondary peak shows up when the binary passes pericentre before it reaches the main peak (for $-0.8\pi \lesssim f_m \lesssim -0.6\pi$ in our setup). Although our linear approximations from Sec. 2.3.4 do not

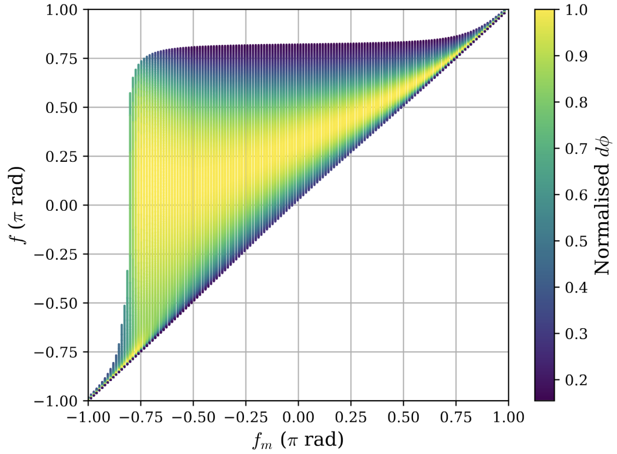

Figure 2.8: **Orbital phase and GW phase shift.** Heat map of the the phase shift, as a function of the orbital phase f, for different realisations of f_m. Each vertical line represents the trajectory of an inspiralling binary, forming at some true anomaly f_f (top), and merging at f_m (bottom). We normalise $d\phi$ for each trajectory, such that $d\phi_{\max} = 1$ for every f_m. We employ an outer eccentricity of 0.9.

include these effects, we find that they still quite accurately predict the magnitude of the peak.

2.4.3 Generalised Behaviour

We generalise our results more by showing the transition between moderate and high eccentricities and when strong curvature effects begin to occur. In the top panel of Fig. 2.10 we show $d\phi_{\max}$ as a function of f_m for a range of e_{out} (from 0.6 to 0.99) for our considered system. Each horizontal slice of this plot can be viewed as a curve like Fig. 2.6. It becomes clear that eccentricity effects are already visible as low as $e_{\text{out}} = 0.6$. There, the location of the maximum phase is already shifted to the left of periastron. Between $e_{\text{out}} = 0.6$ and $e_{\text{out}} = 0.95$, the maximum possible phase shift steadily increases by about 3 orders-of-magnitude.

It is further informative to show the emergence of the secondary peak as we increase the outer eccentricity, and in what range of f_m the peak appears. We portray this in the bottom panel of Fig. 2.10, where the x-axis shows f_m

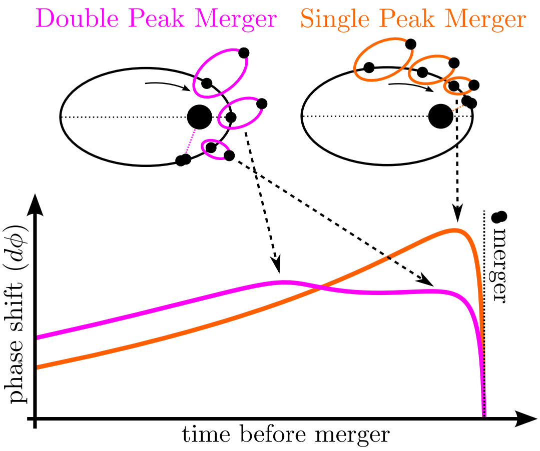

Figure 2.9: **Formation of double peak mergers.** Schematic visualisation of the secondary peak. In orange, we depict the trajectory of a binary merging before pericentre, giving rise to the typical single-peak phase shift. The trajectory of a binary merging after pericentre is shown in pink, where the pericentre passage gives rise to a second peak.

and the y-axis $e_{\rm out}$. We define the presence of a double peak by a sign change in the second time derivative of the phase shift. The green area shows the region of f_m and $e_{\rm out}$ for which there is a secondary peak. The double peak does not occur for the lowest eccentricities, as the curvature effects of passing pericentre are not large enough. With this setup, the secondary peak appears for $e_{\rm out}$ as low as ~ 0.7. As $e_{\rm out}$ increases the green region widens. On the left, it asymptotes towards apocentre. On the right, the width increases faster due to the strong curvature effects. Above $e_{\rm out} \sim 0.9$, the width decreases again, as the binary moves extremely fast close to pericentre. For an eccentricity of ~ 0.95, the time between pericentre passage and a merger happening at f_m of $\sim -0.5\pi$ is so short that the two peaks become indistinguishable.

In summary, the features of the phase shift that are typical of triples with a high outer eccentricity can show up in the phase shift at moderate to moderately high eccentricity. In terms of detections this is a positive result as it indicates towards the possibility of distinguishing circular outer orbits from their eccentric counterparts not just in the most extremely eccentric cases.

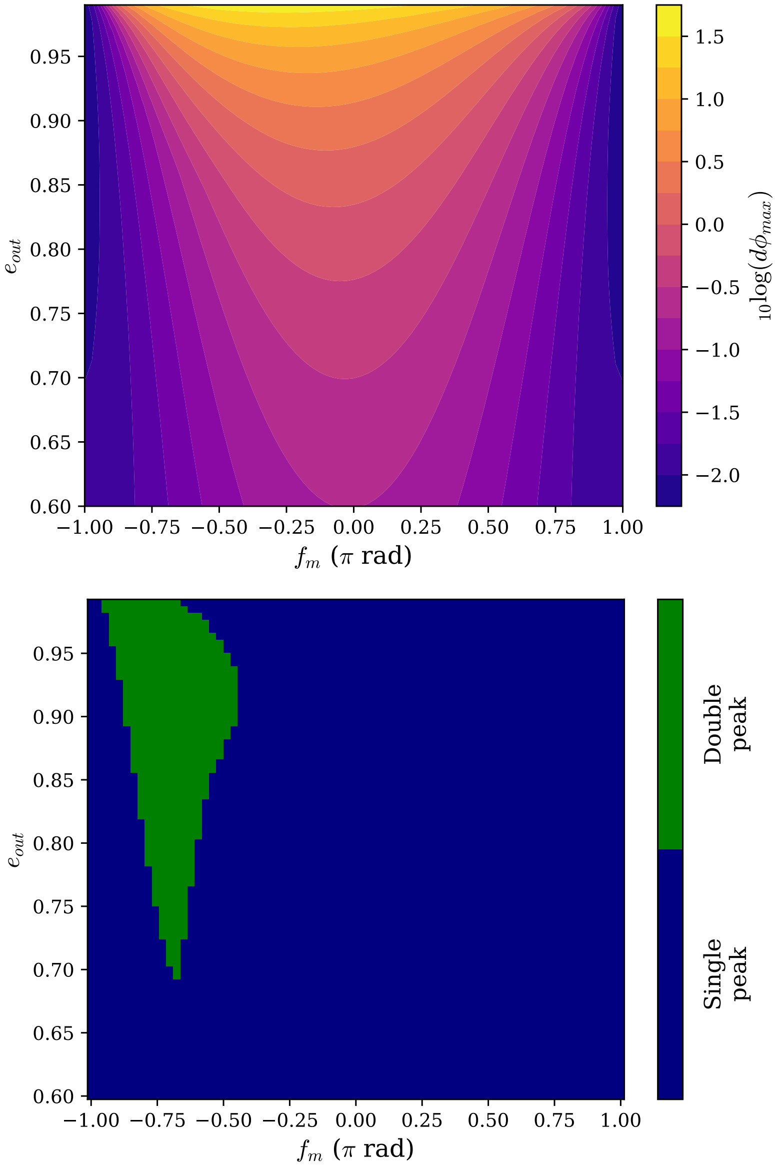

Figure 2.10: *Top:* Maximum phase shift $d\phi_{\max}$ as a function of f_m and e_{out} for the parameters listed in Sec. 2.3.2. *Bottom:* Phase space area in f_m and e_{out} that presents a double-peaked (green) or a single-peaked (blue) dephasing curve.

2.5 Astrophysically Relevant Scenarios

Here we showcase two examples of astrophysical scenarios that may give rise to potentially detectable phase shifts with interesting features. We first investigate in more detail the case of Fig. 2.1, i.e. a triple scattering in e.g. a stellar cluster (see e.g. Samsing, 2018; Gültekin et al., 2006; Samsing et al., 2014; Samsing & Ramirez-Ruiz, 2017). Then, we discuss the influence of tidal forces from the perturber onto the amplitude of the phase shift.

2.5.1 Three-body Scatterings

Chaotic scatterings are ideal environments for producing systems with potentially detectable GW phase shifts. In the top panel of Fig. 2.11, we show once again the trajectories of a chaotic triple producing a highly eccentric merger. From the positions and velocities at merger we can extract the orbital elements of the triple that are needed as input for our model to compute the phase shift, except for a_0 and e_0 which we extract at some reference time before merger. In the bottom panel of Fig. 2.11 we plot the binary and reference trajectory (blue and orange) on top of the data from the N-body simulation (grey shaded).

The resulting phase shift $d\phi$ of this scattering is depicted in Fig. 2.12, as a function of time (top) and orbital eccentricity (bottom). We observe that both versions of our approximation slightly overestimate the magnitude of the (maximum) phase shift, as compared to the prediction from our full semi-analytical model. The reason for this is simply that for this setup, and in this part of the outer orbit, the acceleration when the phase shift is at its maximum (red cross) has changed significantly compared to the value at merger. However, despite these known limitation of our analytical approximations, we do find that the estimates for $d\phi_{\max}$ from both the fast linear approximation (Eq. 2.29) and the circular approximation (Eq. 2.20) are only about a factor of $1-3$ off compared to our more accurate semi-analytical model. This greatly motivates to explore the possibilities of using such approximations for future large-data projects involving determining GW phase shifts for millions of PN few-body scatterings across cosmic time for e.g. different cluster environments. Lastly, we see that our estimates here are fully consistent with the numerically estimated phase shift for this scattering shown in Samsing et al. (2025). Especially our semi-analytical model correctly captures the slope of $d\phi$ on both sides of the peak, whereas the circular approximation that was over-plotted in Samsing et al. (2025) deviates from the truth at earlier times.

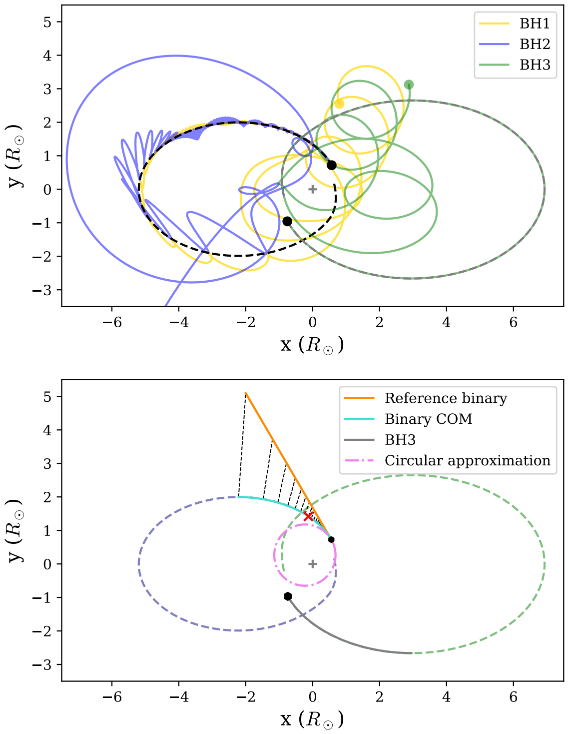

Figure 2.11: **Eccentric orbits in 3-body interactions.** *Top:* The trajectories of the scattering from Fig. 2.1 for illustration. *Bottom:* the binary and reference trajectories including Rømer delay for this particular scattering, including the orbit for our circular approximation. The shaded dashed lines show the final orbits of the binary (blue) and third object (green) in the N-body simulation. The location of the maximum phase shift is depicted by the red cross. All trajectories are shown in the COM frame of the triple.

2.5.2 Influence of Tides

BBHs assembled during chaotic scatterings are often undergoing their first part of their inspiral while being subject to tidal influence from the nearby

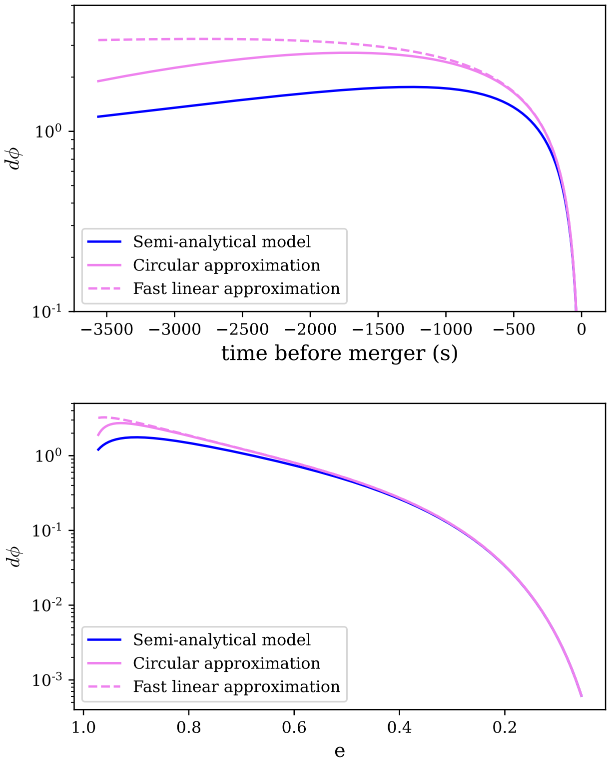

Figure 2.12: **3-body GW phase shifts and models.** GW phase shift as a function of time (*top*) and orbital eccentricity (*bottom*) for the case study depicted in Fig. 2.11. In blue, we show the result from our semi-analytical model, and in pink our approximations: the solid line depicts the circular approximation (Eq. 2.20), and the dashed line shows the fast linear approximation (Eq. 2.26).

perturber. This effect was studied for a few numerical cases in Samsing et al. (2025). Here we perform a more controlled study of this, by investigating how the tidal influence on the eccentricity of the inspiralling BBH will propagate to changes in the expected later GW phase shift. As described below, for this we consider a BBH (BH1,BH2) that is assembled near the Hill sphere with respect to a third object (BH3).

For our initial setup, we consider two BHs that become bound near BH3 after radiating an amount ΔE_{GW} of GW radiation during their first pericentre passage. We can describe this as (see Peters, 1964; Hansen, 1972; Samsing et al., 2018b):

$$\Delta E_{\rm GW} = \frac{85\pi}{12\sqrt{2}} \frac{G^{7/2}}{c^5} \frac{m_1^2 m_2^2 m_{12}^{1/2}}{r_p^{7/2}}, \tag{2.31}$$

Here, $r_p = a(1-e)$ is the distance at pericentre, and $m_{12} = m_1 + m_2$. Under the assumption that the two BHs will end up near the Hill sphere relative to BH3 after their first pericentre passage, they will have an orbital energy given by,

$$\Delta E_{\rm orb} = \frac{G m_1 m_2}{2a} \approx \frac{G m_1 m_2}{R_H}. \tag{2.32}$$

The definition of the Hill radius of BH1, on which we place BH2, is

$$\begin{aligned} R_H &= r(f) \left(\frac{m_1 + m_2}{3 m_3} \right)^{1/3} \\ &= \frac{a_{\rm out}(1 - e_{\rm out}^2)}{1 + e_{\rm out} \cos f} \left(\frac{m_1 + m_2}{3 m_3} \right)^{1/3}. \end{aligned} \tag{2.33}$$

By combining Eqs. 2.31 and 2.32 we now have an estimate for the initial eccentricity and semi-major axis in this GW capture scenario, which is a toy description of what do realistically happen in triple scatterings,

$$e_0 \approx 1 - 2 \left(\frac{85\pi}{12\sqrt{2}} \right)^{2/7} \frac{G^{5/7}}{c^{10/7}} m_1^{2/7} m_2^{2/7} m_{12}^{1/7} \frac{1}{R_H^{5/7}}, \tag{2.34}$$

and

$$a_0 \approx \frac{R_H}{2}. \tag{2.35}$$

Upon formation of the inspiralling BBH, when the binary is still relatively wide, tidal forces from the third object can alter the initial semi-major axis and eccentricity (see also Samsing et al., 2025). Exactly how and to what extent the binary is influenced by the tides is chaotic and is dependent on several factors, such as the orientation and distance with respect to the third object. Any change to the initial conditions may have a large effect on the

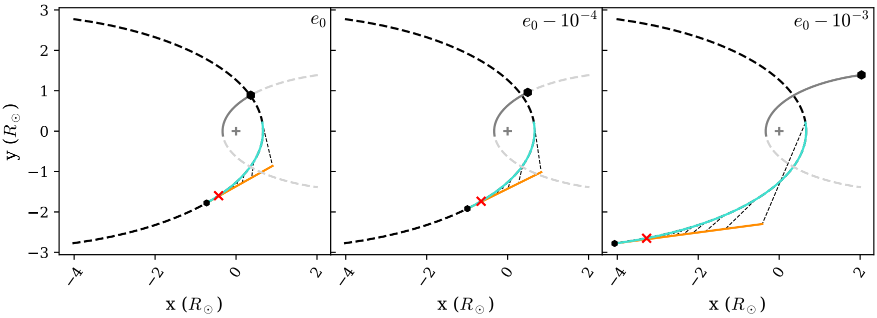

Figure 2.13: **Orbital changes from tides.** Trajectories of the binary COM (turquoise), reference binary (orange), and third BH (grey), for 2 different values subtracted from e_0 (10^{-4}, and 10^{-3}). The choices for the other parameters are described in Sec. 2.5.2.

inspiral time and thereby evolution of the phase shift. To illustrate this, here we investigate how small changes in the initial binary eccentricity e_0 may affect the phase shift evolution. We create a binary that forms on the Hill radius with eccentricity and semi-major axis according to Eqs. 2.34 and 2.35. The binary forms at a true anomaly $f_f = 0.1\pi$. We evolve this system 3 times: once with the original e_0 and a_0, and twice with a slight alteration of the initial eccentricity that can arise from the tidal forces of the perturber. We decrease the initial eccentricity by 10^{-4} and 10^{-3}. The trajectories of each of these four systems are depicted in Fig. 2.13. In Fig. 2.14, we show their phase shift evolution as a function of time and peak GW frequency.

As seen, a small change in eccentricity may lead to drastic changes in the initial pericentre distance, especially in mergers that form at such high eccentricities. The system that we study here has an initial eccentricity of $e_0 \sim 0.998$, and decreasing this by only 10^{-3} would increase the pericentre distance by a factor of 1.49. This allows for less power emitted in GWs in these early stages, therefore resulting in a longer inspiral time. With an eccentricity change of 10^{-4}, the time to coalescence becomes ~ 1.17 times larger. For the 10^{-3} case we obtain an increase in time as large as a factor $\sim$3.7. In terms of detectability, this might work in our favour. However, as we see in the bottom panel of Fig. 2.14, this also has its downsides as it shifts the evolution of the phase shift to a lower peak GW frequency, potentially

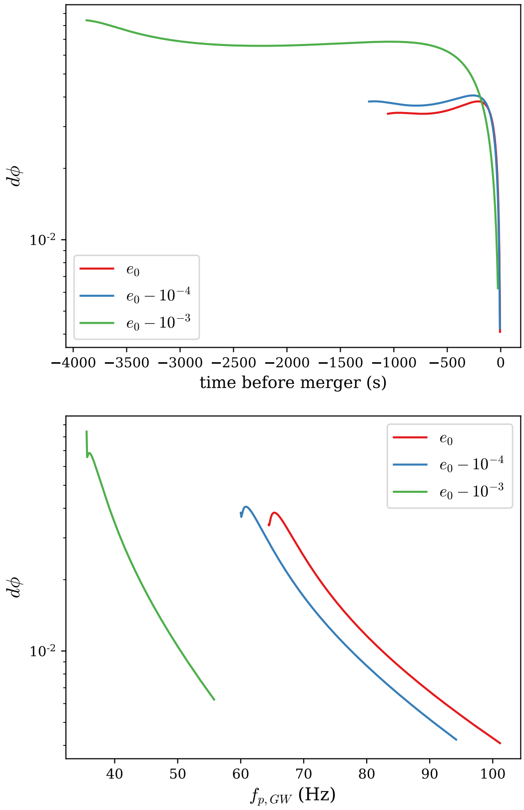

Figure 2.14: **Tidal influence on GW phase shift evolutions.** Phase shift as a function of time (*top*) and peak GW frequency (*bottom*) for three different initial binary eccentricities. We start with e_0 according to Eq. 2.34, and systematically subtract a small value to alter the phase shift evolution. We use $m_1 = m_2 = 5M_\odot$, $m_3 = 20M_\odot$, $e_{\rm out} = 0.9$ and $a_{\rm out} = 10R_\odot$. We observe that each of these trajectories shows the secondary peak in the phase shift that was discussed in the above.

pushing it out of band. Given that

$$f_{\rm p,GW} \sim \frac{1}{\pi}\sqrt{\frac{2Gm}{r_p^3}}, \tag{2.36}$$

increasing r_p by a factor 1.49 lowers the peak GW frequency at formation by a factor ~1.8.

The conclusion from this section is twofold. First of all, we find that our phase shift can readily be applied to numerical simulations of three-body scatterings, and that both our analytical approximations provide accurate estimates of both the amplitude and the shape of the phase shift in eccentric hierarchical triples. An important next step is to use this model on full N-body simulations of GCs to give predictions of the phase shifts originating from this formation channel. Secondly, phase shifts may get largely amplified by tides from the tidal pull of the third black hole. This has the potential to increase the possibility of a detection.

2.6 Summary

In this paper, we explored for the first time the Rømer delay-induced phase shift, arising from an acceleration to the binary COM, of an eccentric BBH that is on an eccentric orbit around a third object. Besides presenting results from a semi-analytical model including orbital evolution using PN-orbit averaged equations and Kepler's Equations, we further presented several analytical approximations. With these tools, we investigated the effects of the GW phase shift that are unique to the outer orbit being eccentric together with an eccentric evolving inner orbit merging BBH. Lastly, we applied our model to relevant astrophysical scenarios of chaotic 3-body scatterings, and studied the effect of tides from the third-body onto the GW phase shift.

The main takeaways from this work are the following:

- For BBHs that inspiral along eccentric orbits the time evolution of the phase shift is dependent on where in the orbit the binary evolves. For low and moderate outer eccentricities, the leading order effect relates to how the magnitude of the GW phase shift can change over the orbit with the distance between the binary and third object, r_m, as $\propto r_m^{-2}$. This especially illustrates that the GW phase shift easily can change by order-of-magnitude over the orbit with its maximum around merger at pericentre.

- At high outer eccentricities ($e_{\text{out}} = 0.9$ in our example), effects of the strong curvature around pericentre are imprinted onto the phase shift. Two characteristics stand out: first, the maximum possible phase shift no longer occurs when the binary merges at pericentre, but slightly beyond ($f_m \sim -0.2\pi$). Secondly, in certain parts of parameter space ($f_m \sim -0.75\pi$ in our example), two peaks may occur. If the binary passes pericentre before the main peak happens, a boost in phase shift due to the large curvature and high velocity may give rise to a secondary peak. These features are important properties of eccentric outer orbits..

- Chaotic scatterings are ideal environments for such phase shifts and their orbits have to be described by eccentric models, as the ones we presented here, compared to the standard circular ones. Our models can readily be applied to state-of-the-art N-body simulations to accurately quantify the phase shift in chaotic three-body scatterings.

- In the case of GW capture formation of BBHs at the Hill sphere, tides from the third body may give rise to small changes in the initial binary eccentricity. This induces an increased time to coalescence and thereby a higher maximum $d\phi$.

The completion of this work has opened up the window to numerous interesting future studies, including quantifying the detectability, GW phase statistics from cluster simulations, comparisons to other dynamical environments, as well as incorporating observer dependence and other GR GW phase shift effects. We reserve that for future works.

Acknowledgements

It is our pleasure to thank Daniel J. D’Orazio, Martin Pessah, David W. O’Neill and Gaia Fabj for their extremely insightful comments and suggestions. K.H. is grateful for the fruitful discussion sessions at CIERA, Northwestern University, which helped complete this work. The authors are supported by Villum Fonden grant No. 29466, and by the ERC Starting Grant no. 101043143 — BlackHoleMergs.

Data Availability

The data underlying this article will be shared upon reasonable request to the corresponding author.

Appendix

Below we link our model to actual GW observations by adding our phase shift to an eccentric waveform model in the LIGO band, and investigate observable characteristics. As mentioned in Sec. 2.6, more detailed studies of the detectability of the phase shift in GW signals will be executed in the near future.

2.7 Effect on gravitational waveform

The phase shift has a direct imprint on the gravitational waveform of the binary. In order to visualise this, we depict the evolution of a perturbed eccentric binary including its waveform in Fig. 2.15. The parameters of the triple are listed in the caption. The top two panels show the setup of the system and the trajectories of the binary COM and the third object. Since we are tracking the evolution only from late inspiral up to merger, the binary COM only covers a tiny part of the outer eccentric orbit, making the trajectory invisible in the top left panel. Both paths are more visible in the zoomed-in version on the right. Note that the x- and y-axis are not on the same scale, making the two trajectories look more different than they actually are. Using the `EccentricTD` waveform model (Tanay et al., 2016) in the `pycbc` Python package (Nitz et al., 2024), we generated an eccentric waveform with $e_0 = 0.25$ at $f_{\rm GW} = 10$ Hz. This can be seen as a case study of an eccentric binary in the LIGO band. This waveform is depicted in the middle panels of Fig. 2.15. Here, two versions of this GW signal are seen; in orange we show the signal to which we applied a Rømer delay corresponding to the triple parameters, and the turquoise curve represents its isolated reference counterpart. In the left panel, it is very difficult to distinguish the isolated and perturbed signal. Their time-dependent offset is more prevalent on the right, where we show a zoomed-in window of the first few orbits after it enters the detector band. This panel clearly highlights the presence of the time delay. At $f_{\rm GW} = 10$ Hz, this setup yields a Rømer delay $\Delta t \sim 0.005$s.

We can track the evolution of the phase shift between these two waveforms as a function of the peak GW frequency $f_{\rm p,GW}$, i.e. the GW frequency that contains the most power (which is eccentricity-dependent). In order to do so, we directly measure $\Delta t, T_{\rm orb}$ and $f_{\rm p,GW}$ from the waveform. We plot the resulting phase shift in the bottom panels of Fig. 2.15 in turquoise. We compare the directly measured phase shift to our semi-analytical model, which we plot in orange. All 7 initial parameters necessary for our model are known, except for a_0; this elusive parameter was obtained from the initial binary orbital period, measured from the waveform. It should be noted that our model returns the orbital frequency rather than the (peak) GW frequency, so we must use Eq. 2.36. In purple, we show the frequency evolution of the phase shift for a binary with the same parameters, but $e_0 = 0$.

We observe some fluctuations in the phase shift that we measured from the waveform. The binary is eccentric, so the GW frequency shows oscillatory behaviour as it chirps due to the fact that the binary separation varies over the course of an orbit. We can see that the eccentric and circular inspiral yield a clearly different phase shift. While they both have similar shapes, the circular version grows much faster in this regime; at $f_{\rm GW} \sim 10$ Hz, it is about 1.5 times larger than the eccentric case. At the same GW peak frequency, the orbital period of the eccentric binary is larger therefore resulting in a lower phase shift. The phase shift that we extracted from the waveform is slightly off from both curves, but clearly fits the eccentric case better. The fact that the eccentric and circular case are potentially distinguishable at frequencies as high as ~ 10 Hz is promising in the context of possible detections. This difference becomes more apparent if we were to track the evolution down to lower frequencies. In the bottom right panel of Fig. 2.15, we extend the phase shift down to a GW frequency of 6 Hz, which lies in the DECIGO band.

The circular case continues to rise, while in the eccentric case the decreasing orbital period catches up with the increasing Rømer delay, resulting in the typical peak.

The phase shift that we extract from the waveform does not match perfectly with our eccentric model. This is largely due to the discrepancy between Keplerian and PN descriptions of the parameters we extract. The orbital parameters e_0 and a_0 (and therefore $T_{\rm orb}$ as well) describe a closed Keplerian orbit, but are not defined as such in the PN framework in which the gravitational waveform of Fig. 2.15 evolves (Damour & Deruelle, 1985; Memmesheimer et al., 2004). In other words, we are extracting Keplerian parameters from a system that is PN in nature. Additionally, we extract the peak GW frequency directly by identifying the duration of the bursts in the waveform corresponding to pericentre passage. This somewhat simplified picture may also give rise to extra errors between the model and measured $d\phi$-$f_{\rm p,GW}$ relation. The fluctuations in the green curve arise from the presence of apsidal precession, which creates oscillations in the peak frequency. We have damped these oscillations using a moving-average filter in order to better isolate the global evolution of the phase shift.

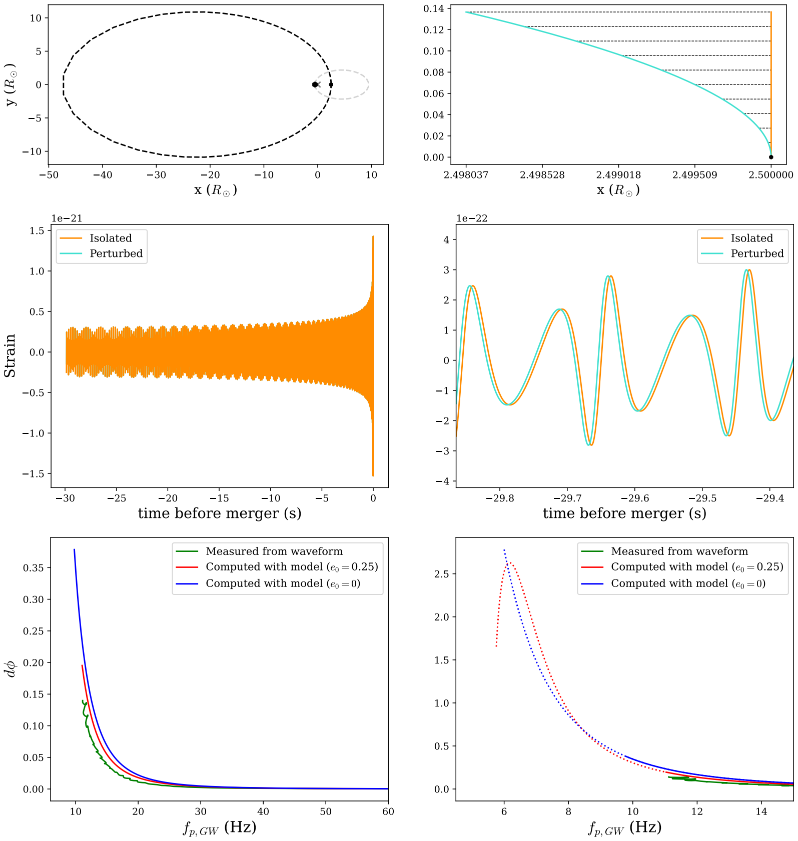

Figure 2.15: **GW phase shift from real GW forms.** Binary parameters: $m_1 = m_2 = 5M_\odot$ with $e_0 = 0.25$ at $f_{\rm GW} = 10$ Hz, at a distance $D = 100$pc and inclination $\iota = 0$. For the triple, we use $m_3 = 100M_\odot$, $a_{\rm out} = 30R_\odot$, and $e_{\rm out} = 0.9$. *Top left*: the trajectories of the binary COM (rightmost black circle) and perturber (leftmost black circle), around the triple COM (red cross). The dashed green auxilliary ellipse depicts the Keplerian outer orbit on which the binary COM is moving. The binary merges at the pericentre of the outer orbit ($f_m = 0$). *Top right*: a zoomed-in version of the left panel, where we can distinguish the trajectory of the binary in the presence of a perturber (orange) and its isolated reference version with a constant speed equal to the orbital speed at merger (turquoise). The coloured lines represent the distance $l(f)$ in Eq. 2.1 at different t before merger. *Middle left*: in orange, we show the eccentric gravitational waveform of the perturbed binary. Behind this, in turquoise, we show the waveform of the isolated binary. These two waveforms are shifted in time due to their associated Rømer delay. The waveforms were generated with the `EccentricTD` model of the `pycbc` package. *Middle right*: zoomed-in version of the left panel. *Bottom left*: in turquoise, we show the phase shift as a function of GW frequency of the perturbed binary, where we extract Δt, T_{12}, and f_{GW} directly from the waveforms in the middle panels. The orange curve represents the phase shift of a binary with the abovementioned parameters, as computed by our semi-analytical model of Sec. 2.3. The purple curve shows the evolving phase shift for a binary with the same parameters, but one whose inspiral is entirely circular. *Bottom right:* here, we show the same plot as on the left, but we extend our semi-analytical models down to a GW frequency of 6 Hz.

Chapter 3

Large Gravitational Wave Phase Shifts from Strong 3-Body Interactions in Dense Stellar Clusters

”Nu hebben we een spoor, geloof ik!”
– Kuifje

This chapter includes the article *“Large Gravitational Wave Phase Shifts from Strong 3-Body Interactions in Dense Stellar Clusters”*, by Kai Hendriks, Dany Atallah, Miguel Martinez, Michael Zevin, Lorenz Zwick, Alessandro A. Trani, Pankaj Saini, János Tákatsy, and Johan Samsing, in review for publication in *Physical Review Letters*.

3.1 Abstract

The phase evolution of gravitational waves (GWs) can be modulated by the astrophysical environment surrounding the source, which provides a probe for the origin of individual binary black holes (BBHs) using GWs alone. We here study the evolving phase of the GW waveform derived from a large set of simulations of BBH mergers forming in dense stellar clusters through binary-single interactions. We uncover that a well-defined fraction of the assembled eccentric GW sources will have a notable GW phase shift induced by the remaining third object. The magnitude of the GW phase shift often exceeds conservative analytical estimates due to strong 3-body interactions, which occasionally results in GW sources with clearly shifted and perturbed GW waveforms. This opens up promising opportunities for current and future GW detectors, as observing such a phase shift can identify the formation environment of a BBH, as well as help to characterise the local properties of its surrounding environment.

3.2 Introduction

Gravitational wave (GW) templates for binary black hole (BBH) mergers are constructed with the masses, spins, and orbital eccentricities of the progenitor systems. The different proposed formation channels of BBH produce distinct features in these three parameters, indicative of the BBH formation mechanism (e.g. Zevin et al., 2017; Su et al., 2021; Gültekin et al., 2006; Samsing et al., 2014; Samsing & Ramirez-Ruiz, 2017; Samsing & Ilan, 2018; Samsing et al., 2018b,a; Samsing & D'Orazio, 2018; Rodriguez et al., 2018; Liu et al., 2019b). While powerful, this method only allows for population-level statements and cannot on its own directly show how a *single* BBH formed.

A novel approach that is gaining increasing attention is to identify direct modulations of the GW signals of binaries due to the astrophysical environment in which they form, which, if observable, yield a means to probe the environment and formation mechanism of the BBH itself on a *single-event basis* (e.g. Vijaykumar et al., 2023). These modulations include general relativistic propagation effects (e.g., GW source acceleration (e.g. Yunes et al., 2011; Meiron et al., 2017; Inayoshi et al., 2017b; Robson et al., 2018; Chamberlain et al., 2019; Randall & Xianyu, 2019a; Wong et al., 2019; Tamanini et al., 2020; D'Orazio & Loeb, 2020; Toubiana et al., 2021; Strokov et al., 2022; Xuan et al., 2023; Laeuger et al., 2024; Vijaykumar et al., 2023; Samsing et al., 2025; Hendriks et al., 2025), GW lensing and gravitational redshift (e.g. Gondán & Kocsis, 2022; Pijnenburg et al., 2024)), astrophysical environmental effects (e.g., gas dynamical friction (e.g. Barausse et al., 2014; Zwick et al., 2023) and tidal forces (Samsing et al., 2025)), and effects beyond classical general relativity (GR) (e.g. Camilloni et al., 2023, 2024). As no BBH merges in a completely empty Universe, such effects should leave imprints in every observed GW signal; however, in most cases the modulations are too small to be resolved. This has led to the key question whether any of the considered BBH merger formation channels such as stellar clusters (Portegies Zwart & McMillan, 2000; Lee et al., 2010; Banerjee et al., 2010; Tanikawa, 2013; Bae et al., 2014; Rodriguez et al., 2015; Ramirez-Ruiz et al., 2015; Rodriguez et al., 2016a,b,b; Askar et al., 2017; Park et al., 2017; Rodriguez et al., 2018; Samsing, 2018; Samsing & D'Orazio, 2018; Samsing et al., 2020; Trani et al., 2021, 2022, 2024a), isolated binary stars (Dominik et al., 2012, 2013, 2015; Belczynski et al., 2016b,a; Silsbee & Tremaine, 2017; Murguia-Berthier et al., 2017; Rodriguez & Antonini, 2018; Schrøder et al., 2018; Spera et al., 2019; Tanikawa et al., 2021, 2022; Iorio et al., 2023), active galactic nuclei (AGN) discs (Bartos et al., 2017; Stone et al., 2017; McKernan et al., 2018; Tagawa et al., 2020; Samsing et al., 2022; Trani et al., 2024b; Fabj & Samsing, 2024), or galactic nuclei (O'Leary et al., 2009; Hong & Lee, 2015; VanLandingham et al., 2016; Antonini & Rasio, 2016; Stephan et al., 2016; Hoang et al., 2018; Hamers et al., 2018; Trani et al., 2019; Liu et al., 2019a; Liu & Lai, 2021; Atallah et al., 2023; Trani et al., 2024b), naturally produce a notable fraction of mergers with measurable GW modulations able to inform about the environment of the merger.

In this *Letter* we perform post-Newtonian ($\mathcal{PN}$) N-body simulations (see Methods), to show that BBHs formed through binary-single interactions oc-

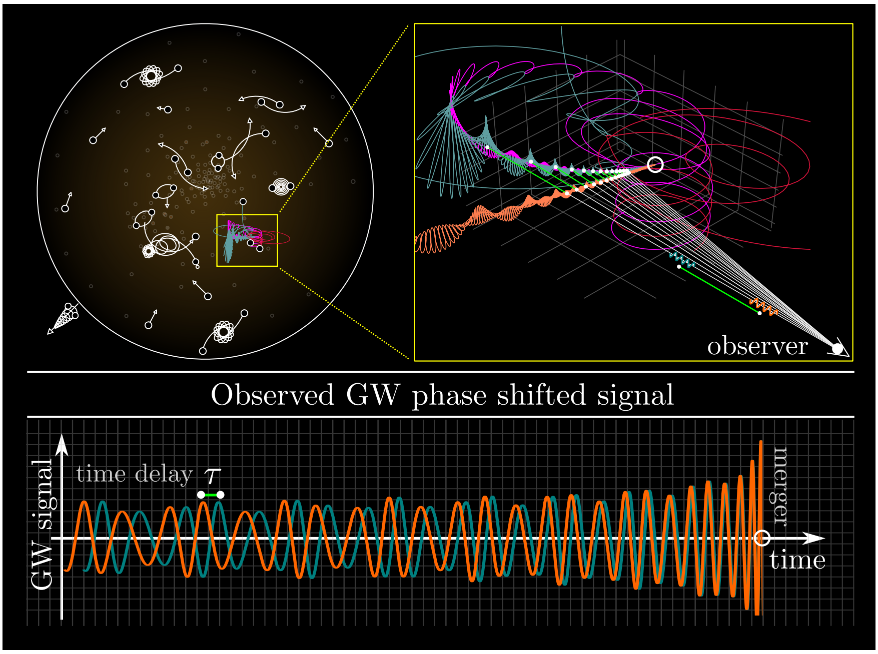

Figure 3.1: **Illustration of 3-body interaction resulting in a BBH merger with an observable GW Phase Shift.** *Top left*: A stellar cluster with highlighted BH interactions, each of which is able to produce BBH mergers. *Top right*: Zoom-in on a binary-single interaction resulting in a BBH merger with the third object still bound (3-body merger). *Turquoise*- and *pink* lines show the trajectory of the merging BHs (true path), where the *orange* lines illustrate the path the BBH would have taken without the third object (reference path). The trajectory of the third BH is depicted in *red*. The *white* lines show lines-of-sight for an observer located in the lower right corner, where the *green* lines illustrate the spacial distance between the true- and the reference paths along the sight-lines, respectively. *Bottom*: GW strain as a function of time. The *turquoise* curve shows the GW signal for the observed BBH inspiral (true path), where the *orange* shows what the isolated BBH merger signal would look like (reference path). The two signals are shifted by the light crossing time between the true and the reference BBH paths, i.e. the time it takes the GWs to travel along the green lines. This gives rise to a unique observable GW phase shift that can be directly mapped to the BBH formation and environment.

curring in dense stellar clusters naturally lead to a well-defined population of GW sources with a measurable GW phase shift caused by the presence of the third object. This is illustrated in Fig. 3.1, which shows an illustration of different dynamical interactions in a cluster environment (*upper left*), a BH binary-single interaction producing a GW-driven merger (*upper right*), and the corresponding GW phase-shifted signal caused by the presence of the third-object (*lower panel*). Several dynamical pathways can lead to BBH mergers in clusters (e.g. Samsing et al., 2020), but the pathway relevant for clearly producing phase-shifted sources observable by ground based detectors is characterized by two of the three interacting BHs inspiralling and merge while the third is still bound (Fig. 3.1 upper right and Fig. 3.2), also referred to as a *3-body merger* (see Methods). Such 3-body mergers constitute $\sim 10\%$ of the BBH mergers from globular clusters (GCs) (Samsing, 2018) and dominate the fraction of eccentric sources, which implies that GW phase-shifted sources will form in notable numbers with observable prospects for both current ground-based GW detectors (LIGO/Virgo/KAGRA) (Aasi et al., 2015; Acernese et al., 2015; Akutsu et al., 2019; Abbott et al., 2018) and future (Einstein Telescope (ET) (Maggiore et al., 2020), Cosmic Explorer (CE) (Evans et al., 2023)), as well as space-borne detectors (DECIGO/TianQin/Taiji (Kawamura et al., 2011; Luo et al., 2016; Hu & Wu, 2017; Liu et al., 2020) (deci-Hertz) and LISA (Amaro-Seoane et al., 2017) (milli-Hertz)).

3.3 Gravitational Wave Phase Shifts

The GW phase shift in 3-body mergers arises from the BBH being bound to the single BH while merging, and therefore moving on a curved orbit with a time-varying velocity along the line-of-sight (LOS) relative to the observer. This creates a time-dependent Doppler shift of the GW waveform, which translates to a GW phase shift that can be mapped to the dynamics of the 3-body system (Samsing et al., 2025), analogous to binary pulsar timings (e.g. Meiron et al., 2017; Samsing et al., 2025).

In the limit where the acceleration $\mathbf{a}$ of the BBH center-of-mass (COM) near merger from the presence of the third body can be assumed constant, the maximum displacement in time between a GW signal sent from the accelerated BBH path and a non-accelerated path as seen by a distant non-cosmological observer is given by (e.g. Hendriks et al., 2025),

$$\tau(t) = \frac{1}{2c}|\mathbf{a}|t^2 = \frac{1}{2}\frac{Gm}{c}\frac{t^2}{R^2}. \tag{3.1}$$

Here we assume all three BHs have equal mass m, c denotes the speed-of-light, and R refers to the distance between the BBH COM and the single BH at the time of merger (see Methods for solution to the unequal mass case). This τ corresponds to the time it takes a light pulse to travel along one of the green lines shown in Fig. 3.1; a time that often is referred to as the *Rømer Delay*. From τ, the GW phase shift ϕ, which is the difference in angular cycles of the GW signal in units of radians, can now be expressed as (Samsing et al., 2025)

$$\Delta\phi(t) \approx 2\pi\frac{\tau(t)}{T(t)} \approx \frac{\sqrt{2}}{2}\frac{G^{3/2}}{c}\frac{m^{3/2}}{R^2} \times \frac{t^2}{a(t)^{3/2}}\,, \tag{3.2}$$

where $T(t)$ and $a(t)$ denote the BBH orbital time and the BBH semi-major axis (SMA), respectively, at time t. Using the analytical framework of Peters (1964), hereafter referred to as *Peters64*, for relating the time t to the BBH's eccentricity, e, and SMA, a, as well as the relation for $a(e)$, one now finds (see Methods),

$$\begin{aligned}\Delta\phi(e) \approx{}& \frac{144}{85^2 g(1)^{13/2}}\frac{c^9}{G^{9/2}} \times \frac{1}{R^2}\frac{r_0^{13/2}}{m^{9/2}}\\ &\times e^{78/19}(1-e^2)^{1/2}g(e)^{13/2},\end{aligned} \tag{3.3}$$

where $g(e) = (1 + 121e^2/304)^{870/2299}$, and r_0 is the peri-center distance of the merging BBH at the time of formation during the interaction. This r_0 maps to a corresponding GW peak frequency as (e.g. Samsing, 2018)

$$f_0 \approx \frac{1}{\pi}\sqrt{2Gm/r_0^3}, \tag{3.4}$$

which can be used as a proxy for judging if the BBH is likely to be in the observable band or not (see also Vijaykumar et al. (2024)). It should be noted that the definition of the eccentricity in this work is based on the peak harmonic of the orbital frequency Wen (2003); Vijaykumar et al. (2024). By maximizing the function $e^{78/19}(1-e^2)^{1/2}g(e)^{13/2}$ from Eq. (3.3), one finds that the GW phase shift $\Delta\phi(e)$ takes its maximum value at eccentricity

$e_m \approx 0.95$, with corresponding GW peak frequency (see Methods),

$$f_m \approx f_0 \left(\frac{2e_m^{12/19}}{1+e_m} \frac{g(e_m)}{g(1)} \right)^{-3/2}. \tag{3.5}$$

To summarise, given r_0 and R for each individual scattering, one can now estimate the maximum GW phase shift $\Delta\phi(e_m)$ using Eq. (3.3) and the corresponding f_m using Eq. (3.5). We now consider this formalism in the scattering experiments described in the following section.

3.4 Results

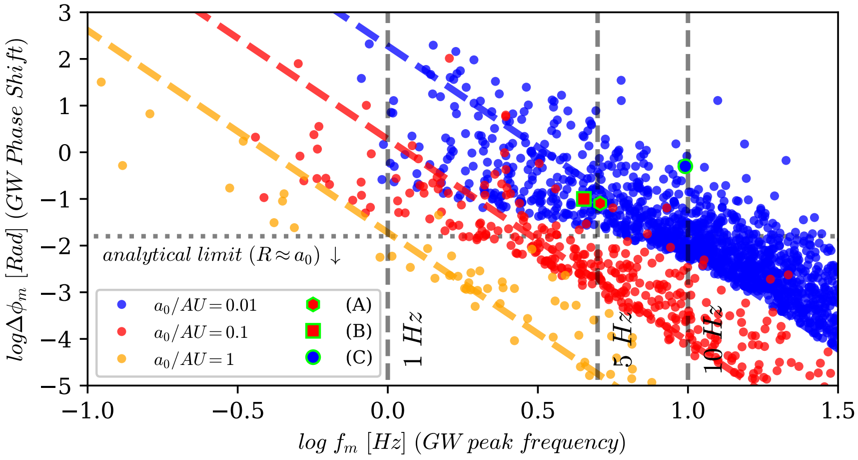

Figure 3.2: **Distribution of maximum GW phase shifts from 3-body BBH mergers.** Results from $\mathcal{PN}$ simulations between a BBH and a single incoming BH that concludes with two of the three BHs merging while the third BH is still bound (see Fig. 3.1 and Fig. 3.3). Each dot shows the *maximum observable GW phase shift* (y-axis) for each of these mergers, as a function of the corresponding GW peak frequency (bottom x-axis) or merger time (top x-axis), derived using the methods outlined in Sec. 3.3. Each colour refers to a different SMA of the initial BBH before interaction: $\sim$ 1 AU (*orange*), $\sim$ 0.1 AU (*red*), and $\sim$ 0.01 AU (*blue*). The *dashed coloured lines* illustrate the asymptotic limit $\Delta\phi \propto f^{-13/3}$, where the *horizontal dotted line* indicates the analytical maximum value for $\Delta\phi$ assuming the distance between the BBH and the single BH, R, is similar to the initial SMA, a (see Methods). The three highlighted examples, **(A,B,C)**, are shown and studied further in Fig. 3.3.

We now consider results from controlled $\mathcal{PN}$ binary-single interactions between BBHs with initial SMA $a = 0.01, 0.1, 1$ AU, respectively, and an incoming BH, all with equal mass $m = 20\ M_{\odot}$. These values are characteristic for BHs interacting in dense stellar systems, as these map to stellar clusters with escape velocities, v_e, of $\sim 30\ \mathrm{km\,s^{-1}}$ (globular cluster), $\sim 90\ \mathrm{km\,s^{-1}}$ (dense stellar cluster), $\sim 300\ \mathrm{km\,s^{-1}}$ (nuclear star cluster), for $a = 1, 0.1, 0.01$ AU, respectively (e.g. Antonini & Rasio, 2016). For every 3-body merger that forms, we measure numerically r_0 and R, from which we estimate the maximum GW phase shift and corresponding GW peak frequency, as outlined in Section 3.3.

Fig. 3.2 shows our numerically derived distributions of f_m and $\Delta\phi(e_m)$. As seen, the chaotic nature of the binary-single problem leads to GW sources with notable GW phase shifts, especially in the range between $1 - 10$ Hz, accessible to third-generation (3G) ground-based GW observatories such as ET and CE. For instance, $\sim 20\%$ of the population with $a_0 = 0.1$ AU (red) has a maximum phase shift above 0.01 radians. This result is non-trivial, as an analytical estimate for the maximum GW phase shift results in a near universal upper limit of $\Delta\phi_H(e) \sim 10^{-2} \times (m[M_{\odot}]/R[\mathrm{AU}])^{1/7}$ radians (Samsing et al., 2025), which is derived using Eq. 3.3 with r_0 set to its maximum possible value, corresponding to where the merging BBH starts exactly at its Hill sphere relative to the single BH at distance R (see Methods).

To understand what kind of 3-body evolutions are able to bypass the analytical limit of $\sim 10^{-2}$ radians, we now consider the three distinct examples shown in Fig. 3.3. In **(A)**, we show a highly chaotic and long-lived interaction, that concludes with an endstate charaterized by the BBH passing the bound single near closest approach on a clearly curved orbit. In **(B)**, we show an example where the BBH merges right after turning around to directly move towards the bound single. This creates a large offset between the reference- and the true trajectory. Note also how the single BH scatters off the BBH near the 3-body COM $(0, 0)$ as it inspirals. This creates large extra perturbations to the GW signal. In **(C)**, we show a case where the merging BBH is heading directly towards the bound single BH. Here there is no significant curvature, but the acceleration along its direction of motion towards the single BH creates the GW phase shift. Note that the orbital precession due to the 1- and 2-$\mathcal{PN}$ terms is included in this figure for a more accurate illustration of the dynamics.

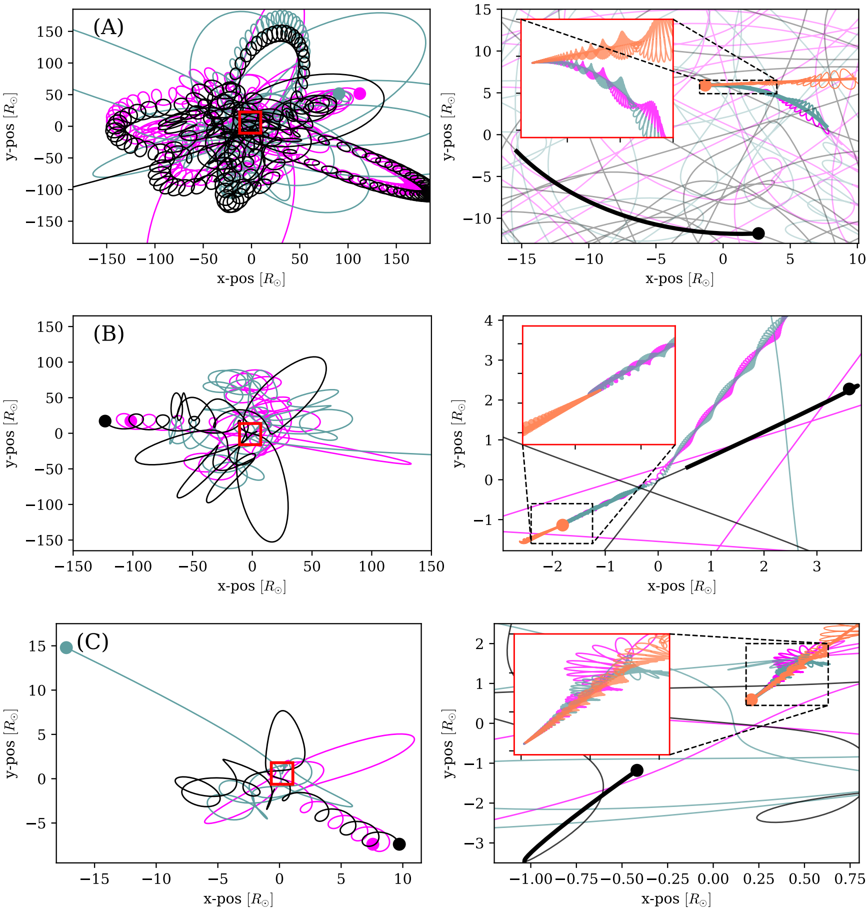

Figure 3.3: **Examples of 3-body BBH mergers resulting in significant GW phase shifts.** The shown interactions involve BHs with equal mass $m = 20M_\odot$, and initial SMA $a = 0.1$ AU for case **(A)** and **(B)**, where case **(C)** has $a = 0.01$ AU. The filled-circles in the left figures indicate the initial positions of the BHs, where the filled-circles in the right figures show the end positions at merger. The orange lines illustrate the trajectory the merging BBHs would take if the third BH was not there (see Fig. 3.1). Common for the cases that give rise to significant GW phase shifts is that the chaotic nature of the 3-body problem brings the BBH close to the remaining bound single BH near merger. This is clearly seen in these examples. GW phase shifts and corresponding peak frequencies for (A,B,C) are shown in Fig. 3.2.

As follows from Eq. 3.3, the only important parameter that can freely vary during interactions, and also lead to a large GW phase shift at a given f, is the distance R. The GW sources we see forming with the largest GW phase shift are therefore all characterized by having the remaining single BH much closer at merger than expected from the initial binary separation. As illustrated, this all follows naturally from the chaotic nature of the 3-body problem, which further opens up for new directions in performing, classifying and identifying GW phase-shifted sources in $\mathcal{PN}$ few-body scatterings.

GW phase shifts being a natural outcome when BBHs merge through few-body interactions in stellar clusters opens up tremendous possibilities for probing the origin and assembly mechanisms of individual GW sources. In particular, many of these systems form at GW frequencies of a few hertz, placing them near the lower end of the sensitivity band of future observatories such as ET and CE. GW phase shifts from Rømer delay have been quantified to be among the loudest type of environmental effect (Zwick et al., 2025c; Takátsy et al., 2025; Zwick et al., 2025b) and, given their large amplitude found in this work and the sensitivity of next-generation detectors, they are expected to be present in a significant portion of GW signals if these dynamical environments contribute to the merger rate.

3.5 Acknowledgements

The authors are grateful to Lorenzo Speri, Fabio Antonini and Daniel J. D'Orazio for useful discussions. K.H, L.Z., P.S., J.T, and J.S. are supported by the Villum Fonden grant No. 29466, and by the ERC Starting Grant no. 101043143 – BlackHoleMergs led by J. Samsing. M.Z. gratefully acknowledges funding from the Brinson Foundation in support of astrophysics research at the Adler Planetarium. A.A.T. acknowledges support from the Horizon Europe research and innovation programs under the Marie Skłodowska-Curie grant agreement no. 101103134.

3.6 Supplemental Material: Methods

3.6.1 Analytical Framework

Our analytical framework presented in Sec. 3.3 builds on the 2.5 $\mathcal{PN}$ orbit-averaged equations presented by Peters64. Despite these only including the lowest order $\mathcal{PN}$ terms and using Newtonian definitions of the orbital elements (e.g. Zwick et al., 2020), these equations still offer very useful insight into the general scalings of the problem, as well as a reliable and fast way of estimating the GW phase shift of 3-body mergers. The phase shift that we consider and is generally considered in the literature (e.g. Meiron et al., 2017; Vijaykumar et al., 2023; Robson et al., 2018) simply originates from the acceleration of the binary COM, as is evident from Eq. 3.1. Therefore, our scalings with masses and distance are fully consistent with this framework. Through the Peters64 equations, effects from the evolving eccentricity are only included in our model at the lowest order. While the Peters64 inspiral time is known to differ by up to a factor of a few from the exact general relativistic value, particularly at high eccentricities (Fumagalli et al., 2025), we note that the distributions and results presented in Fig. 3.2 are fundamentally determined by the proximity of the third object to the binary, and are thus not sensitive to the precise inspiral time prescription. However, if desired, our framework can be followed up using more sophisticated analysis methods (see Sec. 3.4 and (Samsing et al., 2025)).

For deriving the relations in Sec. 3.3, we make use of the formalism from (Samsing et al., 2025; Hendriks et al., 2025), which presented analytical closed-form solutions to the limit where the acceleration of the eccentric inspiraling BBH is assumed constant, also referred to here as the *linear limit*. We further focus on the maximum possible GW phase shift, denoted by $\Delta\phi$, which is related to the observer dependent value given by $\delta\phi \approx \Delta\phi \times cos(i)sin(j)$, where i is the angle in the plane of the ‘outer binary’ (the binary composed of the BBH and the single BH) between the LOS of the observer and the line connecting the location of BBH merger and the COM of the 3-body system, and j is the angle between the LOS and the angular momentum vector of the ‘outer binary’ (e.g. Meiron et al., 2017; Samsing et al., 2025).

We start by noting that the time dependent GW phase shift can be approximated by the light crossing time between the perturbed (accelerated path) and the un-perturbed (linear path), defined by τ, divided by the orbital time of the inspiraling BBH, T, times 2π (see Fig. 3.1). In the limit where the acceleration on the COM of the inspiraling BBH is assumed constant, one therefore finds that $\Delta\phi$ can be written as (Samsing et al., 2025)

$$\Delta\phi(t) \approx 2\pi\tau(t)/T(t). \tag{3.6}$$

Now using that the time shift (see Fig. 3.1)

$$\tau(t) = \frac{l(t)}{c} = \frac{1}{2}\frac{Gm_3}{c}\frac{t^2}{R^2}, \tag{3.7}$$

and the orbital time $T(t)$ is given by

$$T(t) = 2\pi\sqrt{a(t)^3/Gm_{12}}, \tag{3.8}$$

one finds that $\Delta\phi$ can be written as,

$$\Delta\phi \approx \frac{1}{2}\frac{G^{3/2}}{c}\frac{m_3 m_{12}^{1/2}}{R^2} \times \frac{t^2}{a(t)^{3/2}}, \tag{3.9}$$

where $a(t)$ is the SMA of the BBH at time t, R is the distance between the BBH and the single at the time of merger, m_1, m_2, m_3 are the masses of the two BBH components and the the single BH, respectively, and $m_{12} = m_1 + m_2$ is the total mass of the BBH. As the GW phase shift is defined as a function of time leading up to merger, the time t can be replaced by the merger time in the rest frame of the BBH. For this we approximate the merger time by the expression given by Peters64,

$$t_e \approx \frac{3}{85}\frac{c^5}{G^3}\frac{a^4(1-e^2)^{7/2}}{m_1 m_2 m_{12}}, \tag{3.10}$$

where e is the eccentricity of the BBH. By now using the relation between a and e as presented in Peters64,

$$a(e) = \frac{C_0 e^{12/19}}{(1-e^2)} \times g(e), \tag{3.11}$$

where

$$g(e) = \left(1 + 121e^2/304\right)^{870/2299}, \tag{3.12}$$

and C_0 is a constant that depends on the initial conditions, a_0, e_0, we can now replace the dependence of a with eccentricity e in the above relations. For determining C_0 we note that the 3-body BBH mergers we consider all start with high eccentricity ($e_0 \approx 1$), from which it follows that the constant $C_0 \approx 2r_0/g(1)$, where $r_0 = a_0(1-e_0)$. With this constant we can now write the relation $a(e)$ as,

$$a(e) \approx \frac{2r_0 e^{12/19}}{(1-e^2)} \frac{g(e)}{g(1)}, \ (e_0 \approx 1). \tag{3.13}$$

By substituting this relation between a and e into Eq. 3.9 and Eq. 3.10, one finds

$$\begin{aligned} \Delta\phi(e) \approx & \frac{288\sqrt{2}}{85^2 g(1)^{13/2}} \frac{c^9}{G^{9/2}} \times \frac{m_3}{R^2} \frac{r_0^{13/2}}{m_1^2 m_2^2 m_{12}^{3/2}} \\ & \times e^{78/19}(1-e^2)^{1/2} g(e)^{13/2}, \end{aligned} \tag{3.14}$$

which also can be written in terms of the peak GW frequency at formation,

$$f_0 \approx \frac{1}{\pi}\sqrt{Gm_{12}/r_0^3}. \tag{3.15}$$

Note here that both e and f, which are key GW observables, are somewhat subject to definitions as recently discussed in Vijaykumar et al. (2024).

A convenient aspect of writing Eq. 3.9 in terms of r_0 is that r_0 only varies very little during the eccentric inspiral phase, in contrast to a, e. This implies that r_0 can be defined relatively accurately without specifying exactly at what point in time it is defined, as long as the BBH is still eccentric enough, or equivalently close enough to its initial assembly. We elaborate further on this in the Sec. 3.6.3.

Considering Eq. 3.14, we see that the only part of the function that relates to the time-evolving BBH is the function

$$F(e) = e^{78/19}(1-e^2)^{1/2}g(e)^{13/2}, \tag{3.16}$$

which has a maximum that defines the maximum of the time-evolving GW phase shift. The eccentricity that leads to this maximum, referred to as e_m, is $e_m \approx 0.95$ (see also (Samsing et al., 2025)) with a corresponding GW peak frequency, $f_m = f(e_m)$, that follows from combining Eq. 3.13 and 3.15,

$$f \approx f_0 \times \left(\frac{2e^{12/19}}{1+e} \frac{g(e)}{g(1)} \right)^{-3/2}. \tag{3.17}$$

The value for f_m can be below the observable band (see Fig. 3.2), and to quantify the maximum measurable value for $\Delta\phi$ when the BBH enters the band one therefore needs to rewrite Eq. 3.9 in terms of f instead of e. However, it is not algebraically possible to express e as a function of f using Peters64's relations. For this, we therefore need to make an approximation in the limit $e \approx 1$ limit for which we can write Eq. 3.17 as $(f/f_0)^{-2/3} \approx e^{12/19}$ that leads to $e \approx (f_0/f)^{19/18} \approx (f_0/f)$. Substituting this into Eq. 3.14 one finds,

$$\begin{aligned} \Delta\phi(f) \approx & \frac{c^9 G^{-7/3}}{2\pi^{13/3}} \left(\frac{5}{256} \right)^2 \times \frac{m_3}{R^2} \frac{m_{12}^{2/3}}{m_1^2 m_2^2} \\ & \times f^{-13/3} \times (1 + (f_0/f))^7 (1 - (f_0/f))^{1/2}. \end{aligned} \tag{3.18}$$

The $\propto f^{-13/3}$ factor correctly defines the asymptomatic limit ($f \gg f_0$), as this is the solution to the well studied circular case (Meiron et al., 2017). Despite the approximation used between e and f above, we find this expression to correctly capture the GW phase shift evolution within a factor of unity of our considered eccentric inspiraling BBH, as a function of f (see also (Samsing et al., 2025)).

Fig. 3.4 shows the $\Delta\phi(f)$ evolution of the inspiraling BBHs from our data

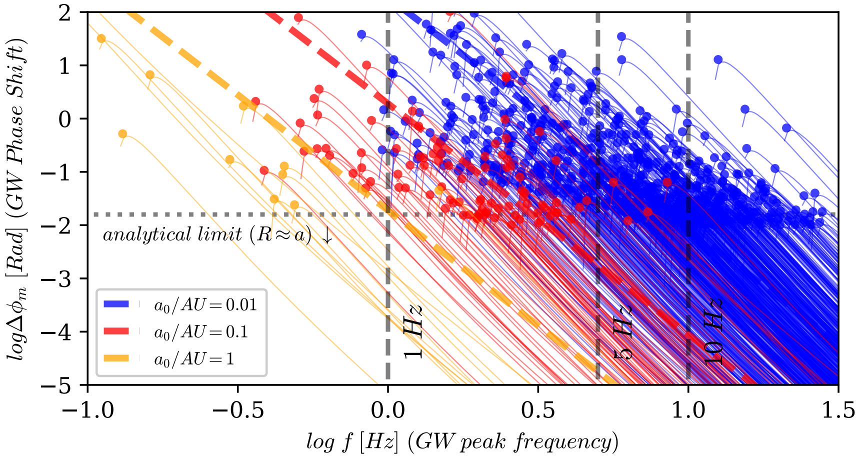

Figure 3.4: **Evolution of GW phase shift with GW peak frequency.** The figure shows evolutionary tracks of the GW phase shift as a function of the GW peak frequency, f, from its initial value at formation, f_0, derived using Eq. 3.18. The data is the same as the one shown in Fig. 3.2, but only including the GW sources with a maximum GW phase shift of $> 10^{-2}$. The filled-circles are identical to the ones shown in Fig. 3.2, and illustrate correctly (within our analytical approximations) the maximum value for the GW phase shift along each track.

presented in Fig. 3.2, with a maximum $\Delta\phi > 10^{-2}$ radians evolved using Eq. 3.18 from their initial formation frequency f_0, towards higher f. The dots at the individual peaks are identical to $\Delta\phi(e_m)$, f_m, and derived from Eq. 3.14 and Eq. 3.17 (the slight offsets are due the approximations we here made for $\Delta\phi(f)$). As seen, several of the BBH sources that peak at low f are still able to enter higher frequency bands but with a smaller $\Delta\phi$. Irrespective of 3G GW detectors (ET, CE) will operate down to 1 or 5 Hz, this clearly shows that GW sources will enter, or even form in 3G GW detectors, and possibly also in current LVK-detectors with a significant GW phase shift.

Fig. 3.5 provides additional insight into the properties of the populations shown in Fig. 3.2. We highlight on the population with an initial semi major axis of 0.1 AU (red in Fig. 3.2). The top panel highlights systems for which the merger time at *assembly*, t_m, exceeds the orbital period, T_0, or the *initital binary* in the scattering. This selection reveals two sub-populations. Systems with $t_m/T_0 > 1$ show phase shifts exceeding the analytical limit, but remaining below the asymptotic limit $f^{-13/3}$. More insight into this can be seen

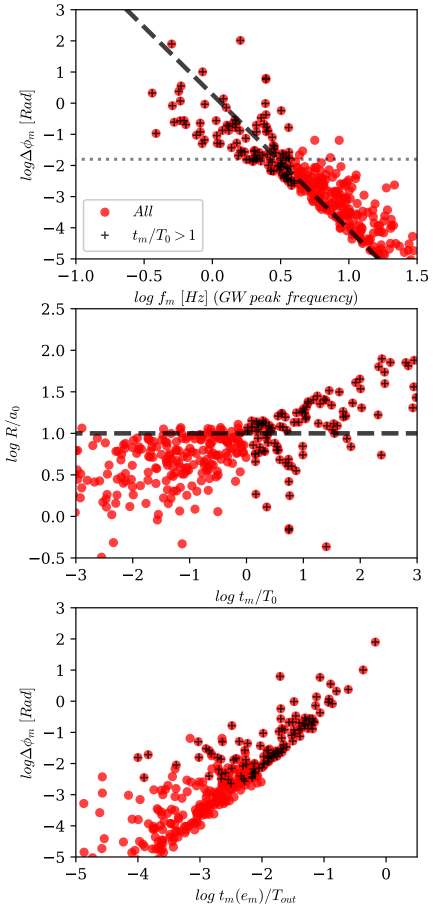

Figure 3.5: **Characteristics of phase-shifted 3-body BBH mergers.** *Top:* the GW phase shift as a function of the peak GW frequency (see Fig. 3.2) for the population with $a_0 = 0.1AU$. The $+$-marked systems are those binaries whose time to merger at assembly (t_m) exceeds the orbital period of the initial binary (T_0). The black dashed line is the asymptotic limit $f^{-13/3}$ and the dotted line is the expected analytical upper threshold according to our analytical model. *Middle:* the distance R at merger between the binary and third body, relative to the semi-major axis of the initial binary, a_0. *Bottom:* the maximum GW phase shift as a function of the merger time at the maximum (where $e = e_m$), relative to the outer orbital period of the tertiary in the 3-body merger ($T_{\rm out}$).

in the middle panel where we plot t_m/T_0 against the distance R relative to semi-major axis of the initial binary a_0. This showcases that these systems correspond to larger separations R/a_0, as the third body can travel farther from the binary, leading to reduced phase shifts relative to the power law.

Lastly, in the bottom panel we show the maximum phase shift as a function of the merger time t_m at said maximum, occurring at eccentricity e_m, relative to the outer orbital period $T_{\rm out}$ of the eventual third body. This highlights that the merger time from the peak is typically much shorter than $T_{\rm out}$, justifying the assumption of constant acceleration.

3.6.2 Dynamical Constraints

In our considered linear limit it appears from Eq. 3.14 that any GW phase shift can be achieved, as long as R and r_0 are chosen to be small and large enough, respectively. However, by imposing a dynamical stability to the system, our linear limit also implies a maximum value for $\Delta\phi$ as a function of m and R.

To see this we note that r_0 cannot take any value, but has to be small enough that the radiated energy over the first peri-center passage,

$$\Delta E_0 \approx \frac{85\pi G^{7/2}}{12\sqrt{2}c^5}\frac{m_1^2 m_2^2\sqrt{m_{12}}}{r_0^{7/2}}. \tag{3.19}$$

leads to an orbital energy

$$E_0 = \frac{Gm_1 m_2}{2a_0}, \tag{3.20}$$

that has a corresponding SMA a_0 that is smaller than the BBH Hill radius, R_H,

$$R_H \sim R((m_1 + m_2)/m_3)^{1/3}, \tag{3.21}$$

by a factor β, such that $a_0 \lesssim \beta R_H$.

By now equating E_0 and ΔE_0, and impose the requirement $a_0 = \beta R_H$ for stability, one finds the following maximum possible value for r_0, defined here as r_H,

$$r_H \approx \left(\frac{85\pi}{6\sqrt{2}}\frac{G^{5/2}}{c^5}\frac{\beta R m_1 m_2 m_{12}^{5/6}}{m_3^{1/3}}\right)^{2/7}. \tag{3.22}$$

The corresponding maximum GW phase shift can now be found be substituting r_H from the above Eq. 3.22 into Eq. 3.14,

$$\Delta\phi_H(e) \approx 10^{-2} \times \left(\frac{\beta}{0.1}\right)^{13/7} \left(\frac{m/M_\odot}{R/AU}\right)^{1/7} F(e). \tag{3.23}$$

As seen here, the maximum value estimated from the characteristic length- and mass-scales of the problem in this linear limit is therefore relatively small, as well as only weakly dependent on the BH mass and initial orbital seperation. However, as presented in Sec. 3.4, BBH mergers with GW phase shifts above this limit still exist, and form as a result of the chaotic nature of the 3-body problem, which occasionally brings the BBH much close that $\sim R$ to the single BH near merger (see also Fig. 3.3).

3.6.3 Numerical Methods

The scatterings presented in this *Letter* were generated with a $\mathcal{PN}$ few-body code that includes 1- and 2-$\mathcal{PN}$ terms which lead to precession as well as the dissipative 2.5-$\mathcal{PN}$ term (Blanchet, 2014). For each of our scatterings we initiate a circular BBH with a given SMA a, and sample the distribution of incoming single BHs at infinity according to the system we consider. From the distribution at infinity, we then propagate each single close to the binary using Kepler's equations following well known procedures (Hut & Bahcall, 1983; Samsing et al., 2014). At this closer distance we then initiate our $\mathcal{PN}$ few-body code, and let it run for a total of 1000 initial BBH orbital times. This resulted in a few percent of inconclusive scatterings, that mainly originates from scatterings for which the third object is sent out on an almost unbound orbit (e.g. Hut, 1983; Samsing & Ilan, 2018). For each BBH that merges during the interaction, i.e. for each 3-body merger, we measure the initial peri-center distance r_0 and the distance from the BBH COM to the third object R at merger, from which we theoretically estimate the GW phase shift using the formalism from the above Sec. 3.6.1. The distance r_0 is measured numerically when the inspiraling BBH is subject to a tidal force from the third object that is $< 10^{-3}$ compared to its own binding force. In this way we make sure that tides no longer impact the BBH evolution. The distance

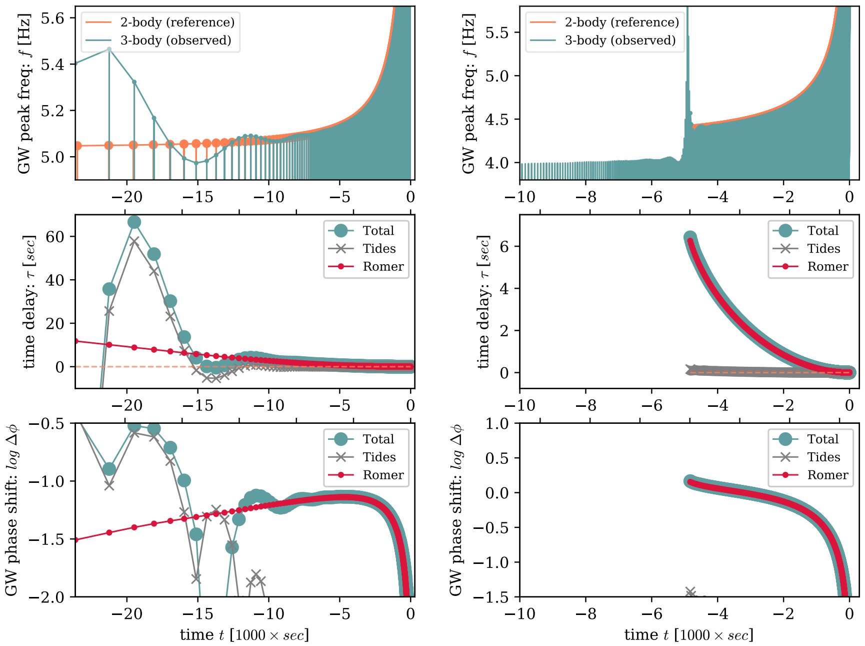

Figure 3.6: **GW Modulations in 3-body interactions.** Numerically derived differences, as seen by a distant non-cosmological observer, between the true inspiraling BBH and its reference BBH for the two examples; (**A**) (*left column*) and (**B**) (*right column*) introduced in Sec. 3.4. For both columns the *top plot* shows the evolution of BBH peak frequency f (the blue and orange lines show results for the perturbed 3-body BBH and its 2-body reference BBH, respectively), the *middle plot* the time delay τ (the blue line shows the total, the grey line shows the contribution from tides, where the red line is the contribution from the BBH COM acceleration), and in the *bottom plot* is shown the corresponding GW phase shift (same notation as for the middle plot). Our analytical framework from Sec. 3.3 describes the evolution shown here with red lines (COM acceleration), where the deviations away from this are coursed by semi-chaotic tidal interactions between the single BH and the BBH. Results are further discussed in Sec. 3.6.4.

r_0 stays approximately constant until the merging BBH starts circularizing, which implies r_0 can be measured relatively unambiguously.

The orange coloured paths seen in Fig. 3.3 and Fig. 3.1, which illustrate the trajectories the BBHs would take if the third object was not there, are derived by evolving the $\mathcal{PN}$ equations-of-motion backwards from merger without the third object. This novel technique, as further described in Samsing et al. (2025) and in Sec. 3.6.4 below, allows for an extremely accurate way of numerically estimating observable Doppler and tidal effects in the GW signal induced by the presence of the third object. Examples of this are shown in Fig. 3.6.

3.6.4 Numerical Estimation of GW Phase Shifts

The distribution of GW phase shifts shown in Fig. 3.2 and our analytical descriptions from Sec. 3.3 do not capture the rich information that otherwise could be encoded in many of the GW phase shifted sources. For this, one needs numerical methods to resolve the fine and often non-linear differences between the true observed BBH and its corresponding reference GW signal.

As an example, Fig. 3.6 shows numerically derived quantities for example $(\mathbf{A})$ and $(\mathbf{B})$ presented in Fig. 3.3. The quantities are derived by comparing the GW signal a distant non-cosmological observer would see from the true BBH evolving near the third object with a reference BBH created by backwards simulating the $\mathcal{PN}$ equations without the third object (Sec. 3.6.3 and Samsing et al. (2025)). In case of example $(\mathbf{A})$, one clearly sees periodic modulations in both the GW peak frequency (*top*), time delay (*middle*), and GW phase shift (*bottom*) below ~ 5000 seconds prior to merger. These originate from the time-dependent tidal coupling between the single BH and the precessing BBH as its inspirals. When the BBH becomes compact enough the tidal coupling fades away, after which the GW phase shift becomes dominated by the BBH COM acceleration. As seen, this part in the GW phase shift until merger, is very smooth and follows accurately our formalism presented in Sec. 3.3. In example $(\mathbf{B})$ is seen a clear strong perturbation of the GW signal ~ 5000 seconds prior to merger. This is due to the single BH scatters off the BBH close to merger (see Fig, 3.3), which leads to an almost impulsive change in the BBH orbital parameters. For 3G detectors operating near 5 Hz, such highly non-linear outcomes should be present, and would provide an enormous amount of unique information about the BBH formation beyond the corresponding GW phase shift and linear predictions.

Chapter 4

Towards Gravitational Wave Parameter Inference for Binaries with an Eccentric Companion

> *"What happened in Monte Carlo happened, and what happened in Barcelona happened, and what happened in Madrid happened, and here we are. We are in Rome."*
>
> – Rafael Nadal

This chapter includes the article *"Towards Gravitational Wave Parameter Inference for Binaries with an Eccentric Companion"*, by Kai Hendriks, Lorenz Zwick, Pankaj Saini, János Takátsy, and Johan Samsing, submitted to *Physical Review D*.

4.1 Abstract

We introduce a complete model for dephasing due to line-of-sight acceleration (LOSA) in gravitational wave (GW) signals from stellar-mass binary black holes (BBHs) in three-body systems. Our prescription provides curvature- and projection-dependent phase features that are not recovered by local-expansion-based treatments. We perform parameter-space surveys and mock parameter inferences assuming the nominal sensitivity of the Einstein Telescope (ET) to identify the regime where the time-varying LOSA allows for separate constraints on the outer orbital parameters, in particular the tertiary mass and distance. We estimate that ET may detect a few to tens of such systems per year, provided that all binaries merge dynamically, and demonstrate that these constraints can be used to directly discriminate between a dynamical and AGN origin for BBHs. Finally, we reanalyse the GW190814 event and four O4a events finding no evidence for LOSA, with the previously claimed LOSA in GW190814 disappearing when a sufficiently long data segment is used.

4.2 Introduction

Understanding the formation pathways of binary black holes (BBHs) remains a central challenge in gravitational-wave (GW) astrophysics, particularly following the now ∼200 BBH detections reported by the LIGO-Virgo-KAGRA (LVK) Collaboration (The LIGO Scientific Collaboration et al., 2025a). Several formation channels have been proposed, including isolated binary stars (Dominik et al., 2012, 2013, 2015; Belczynski et al., 2016b,a; Silsbee & Tremaine, 2017; Murguia-Berthier et al., 2017; Rodriguez & Antonini, 2018; Schrøder et al., 2018; Iorio et al., 2023), dynamical interactions within dense stellar clusters (Portegies Zwart & McMillan, 2000; Lee et al., 2010; Banerjee et al., 2010; Tanikawa, 2013; Bae et al., 2014; Rodriguez et al., 2015; Ramirez-Ruiz et al., 2015; Rodriguez et al., 2016a,b,b; Askar et al., 2017; Park et al., 2017; Samsing, 2018; Samsing & D'Orazio, 2018; Samsing et al., 2020; Trani et al., 2021, 2022), galactic nuclei (GN) (O'Leary et al., 2009; Hong & Lee, 2015; VanLandingham et al., 2016; Antonini & Rasio, 2016; Stephan et al., 2016; Hoang et al., 2018; Hamers et al., 2018; Trani et al., 2019; Liu et al., 2019a; Liu & Lai, 2021; Atallah et al., 2023), active galactic nuclei (AGN) discs (Bartos et al., 2017; Stone et al., 2017; McKernan et al., 2018; Tagawa et al., 2020; Samsing et al., 2022; Trani et al., 2024b; Fabj & Samsing, 2024), single-single GW captures of primordial black holes (Bird et al., 2016; Cholis et al., 2016; Sasaki et al., 2016; Carr et al., 2016), and very massive stellar mergers (Loeb, 2016; Woosley, 2016; Janiuk et al., 2017; D'Orazio & Loeb, 2018). If contributing to the overall merger rate, each channel is expected to produce distinct populations of mergers with characteristic properties in specific observables such as the binary eccentricity (e.g. Gültekin et al., 2006; Samsing et al., 2014; Samsing & Ramirez-Ruiz, 2017; Samsing & Ilan, 2018; Samsing et al., 2018b,a; Samsing & D'Orazio, 2018; Rodriguez et al., 2018; Liu et al., 2019b; Zevin et al., 2019; Samsing et al., 2019, 2020), the relative spin orientation of the merging BBHs (e.g. Kalogera, 2000; Rodriguez et al., 2016c; Liu & Lai, 2018), or the mass distribution (e.g. Zevin et al., 2017; Su et al., 2021).

Instead of focusing solely on population-level characteristics, recent studies have proposed investigating environmental effects (EEs) as an additional means to constrain BBH formation scenarios. EEs are modifications to a vacuum waveform caused by astrophysical perturbations to the GW source (e.g. Chakrabarti, 1993; Ryan, 1995; Barausse & Rezzolla, 2008; Levin, 2007; Kocsis et al., 2011; Barausse et al., 2014; Inayoshi et al., 2017a; Meiron et al., 2017; Bonetti et al., 2017; Torres-Orjuela et al., 2019; Randall & Xianyu, 2019b; Cardoso & Maselli, 2020; D'Orazio & Loeb, 2020; Liu et al., 2022; Xuan et al., 2023; Garg et al., 2022; Cole et al., 2023; Chandramouli & Yunes, 2022; Sberna et al., 2022; Zwick et al., 2023; Tiede et al., 2024; Dyson et al., 2024; Destounis et al., 2023; Cardoso et al., 2022; Caputo et al., 2020; Zwick et al., 2024; Derdzinski et al., 2021; Basu et al., 2024; Caneva Santoro et al., 2024; Levin, 2007; Derdzinski et al., 2021; Garg et al., 2022; Speri et al., 2023; Duque et al., 2025; Liu et al., 2015; Toubiana et al., 2021; Zwick et al., 2023; Martin Barandiaran et al., 2024; Spieksma et al., 2025). Over the last few years, several works have highlighted how EEs may be used as a powerful tool, enabling to identify *smoking gun signatures* of binary formation channels on an individual-event basis. Compact object binary formation pathways that are characterised by strong interactions with the environment, such as the dynamical (Portegies Zwart & McMillan, 2000; Lee et al., 2010; Banerjee et al., 2010; Tanikawa, 2013; Bae et al., 2014; Rodriguez et al., 2015; Ramirez-Ruiz et al., 2015; Rodriguez et al., 2016a,b,b; Askar et al., 2017; Park et al., 2017; Samsing & D'Orazio, 2018; Samsing et al., 2020; Trani et al., 2021; Naoz et al., 2013; Li et al., 2014; Antonini et al., 2016; Antognini & Thompson, 2016; Silsbee & Tremaine, 2017; Randall & Xianyu, 2018; Hamers & Thompson, 2019; Liu & Lai, 2021; Trani et al., 2022; Saini et al., 2025) and AGN (Bartos et al., 2017; Stone et al., 2017; McKernan et al., 2018; Tagawa et al., 2020; Samsing et al., 2022; Trani et al., 2024b,b; Fabj & Samsing, 2024) channels, are expected to produce a significant fraction of sources with detectable EE for next generation ground-based detectors (Zwick et al., 2025b).

In particular, the most promising avenue is the detection of Rømer delays, or line-of-sight acceleration (LOSA)[1] due to a nearby third body (Meiron et al., 2017; Bonvin et al., 2017; Vijaykumar et al., 2023; Samsing et al., 2025; Hendriks et al., 2024, 2025; Robson et al., 2018). Rømer delays induce a frequency-dependent shift $\delta\psi_{\mathrm{R}}$ in the GW phase with an amplitude proportional to the gravitational acceleration and in its simplest form (a constant LOSA) a characteristic frequency scaling of $f^{-13/3}$:

$$\delta\psi_R \propto \frac{m_3}{R_3^2}\, f^{-13/3}, \tag{4.1}$$

where m_3 is the third body mass, R_3 the distance between the third body and the binary centre of mass, and f is the detector frame GW frequency. While the detection of dephasing with this frequency scaling would provide incontrovertible evidence for the presence of a third body, the size of the dephasing itself is determined by a degenerate combination of third body mass and distance. Therefore, it would be impossible to precisely determine the

---

[1] The terms line-of-sight/centre-of-mass acceleration and Rømer delay phase shift (or dephasing) refer to exactly the same type of EE. We use different naming conventions depending on the context.

properties of the third body and distinguish between perturbations from another stellar-mass object (dynamical channel) or a supermassive BH (AGN channel). Previous studies have improved upon constant-acceleration models by incorporating higher-order time derivatives of the LOSA which partially capture the curvature of the outer orbit and yield more accurate dephasings in certain regimes (Tiwari et al., 2024, 2025a,b). However, these treatments rely on local Taylor expansions and therefore cannot reproduce the full, strongly time-dependent structure of the acceleration that arises in eccentric Keplerian orbits or from evolving projection geometry relevant for dynamical interactions in dense stellar clusters.

In this work we introduce a model of Rømer delay which includes arbitrary outer orbit eccentricity and incorporates time-dependent projection effects. This global treatment reveals features in the phase evolution that cannot be captured by expansion-based approaches. We show explicitly in what astrophysical scenarios the mass–distance degeneracy can be broken. Additionally, motivated by the potential for degeneracy-breaking, we re-analyse GW190814, which was previously reported to exhibit a measurable LOSA (Yang et al., 2025), as well as analyse several promising events from the LVK O4a observing run (The LIGO Scientific Collaboration et al., 2025a).

This paper is structured as follows: in Sec. 4.3, we lay out the waveform and dephasing models used in this work, as well as the mathematical frameworks for the parameter inference. In Sec. 4.4, we explore the parameter space of the dephasing model and investigate the interplay between different outer orbital parameters. Subsequently, in Sec. 4.5, we generate several mock GW events that include our updated dephasing model and perform parameter inference assuming ET sensitivity. Lastly, in Sec. 4.6, we show the results from our LOSA inference of GW190814 and several O4a events.

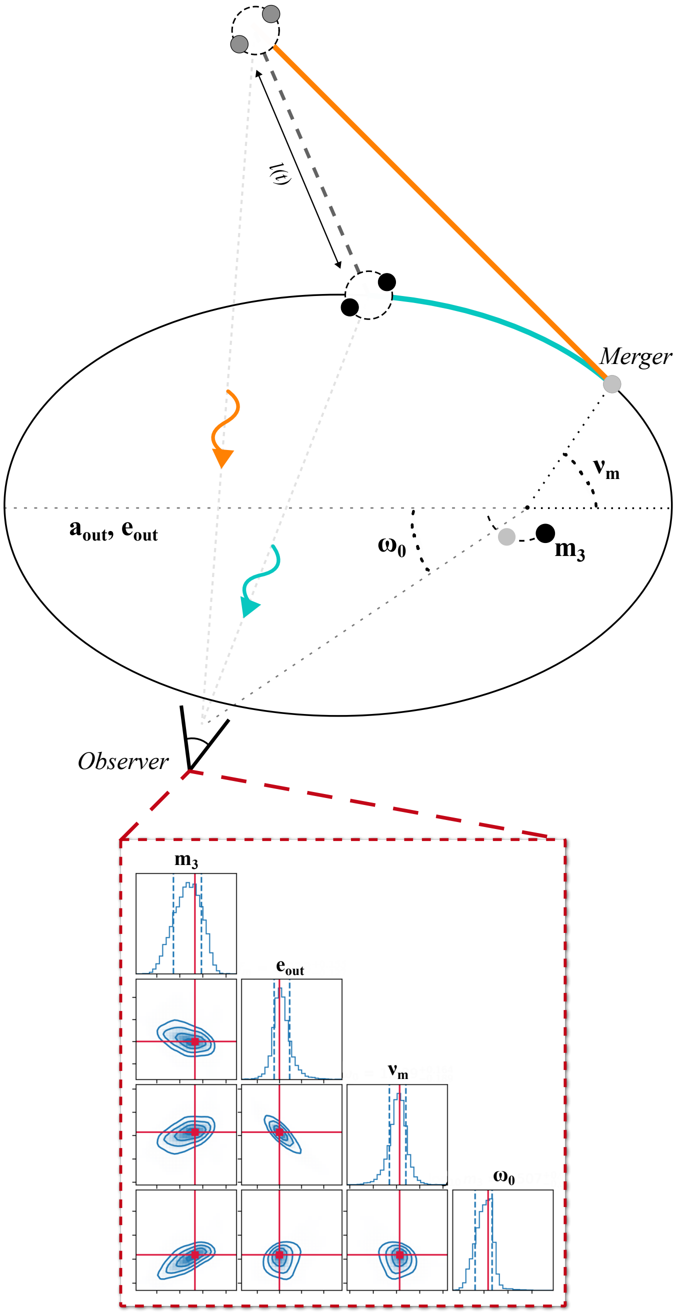

Figure 4.1: Schematic depiction of the premise of this work, in which we study the detectability of the GW phase shift in signals from BBHs whose COM is on an orbit around a third BH. By modelling the outer eccentricity and projection effects, one can in principle constrain the properties of the three-body system.

4.3 Methods

4.3.1 Waveforms and SNR calculations

While it is known that BBHs in realistic dynamical environments can in fact retain a small but non-negligible eccentricity upon entering the detector band (e.g. Samsing, 2018; Romero-Shaw et al., 2020), we assume a circular inner orbit. The circular assumption allows for fast waveform evaluation and for isolating the impact of the environmental dephasing itself. Note however, that eccentricity introduces additional harmonics that encode information about the earlier stages of the inspiral, which can significantly enhance the detectability of environmental effects (Takátsy et al., 2025; Zwick et al., 2025a).

We employ several classes of circular waveform models. For our parameter space survey in Sec. 4.4 and mock inference in Sec. 4.5, we use Fourier space Newtonian waveforms in the stationary phase approximation (Cutler & Flanagan, 1994; Blanchet, 2014):

$$\tilde{h}(f) = \sqrt{\frac{5}{24}}\pi^{-2/3}\frac{Q}{D(z)}\frac{(G\mathcal{M}_z)}{c^{3/2}}^{5/6} f^{-7/6}\exp\left[i\psi_{\rm vac}\right], \tag{4.2}$$

where f is the observer frame GW frequency, $D(z)$ is the luminosity distance, $\mathcal{M}_z$ is the red-shifted chirp mass, and Q a geometric pre-factor. We assume an all-sky average with $Q = 2/5$ and additionally multiply with 3/2 to account for the geometry of the detector (Regimbau et al., 2012). The GW phase $\psi_{\rm vac}$ is given by:

$$\psi_{\rm vac} = 2\pi f t_c - \phi_c - \frac{\pi}{4} - \frac{3}{128}\left(\frac{\pi G\mathcal{M}_z f}{c^3}\right)^{-5/3}. \tag{4.3}$$

Here we set the constant phase offset $\phi_{\rm c}$ and integration constant $t_{\rm c}$ representing the phase and time at coalescence both to 0, as they do not influence simple estimates of the BBH SNR (though they are crucial for full parameter inference). The vacuum phase (Eq. 4.3) can be supplied by additional dephasing prescriptions as a simple model for EE, as is done in many works (e.g. Zwick et al., 2025b; Samsing et al., 2025; Hendriks et al., 2025; Samsing et al., 2024; Zwick & Samsing, 2025; Takátsy et al., 2025). Then:

$$\psi_{\mathrm{tot}} = \psi_{\mathrm{vac}} + \psi_{\mathrm{EE}}. \tag{4.4}$$

For the analysis of GW190814 and the O4a events in Sec. 4.6, we employ the `IMRPhenomXPHM` waveform, enabling a direct comparison with Yang et al. (2025) and the GWTC-4 catalogue (The LIGO Scientific Collaboration et al., 2025a). For consistency with GWTC-4, we additionally include the `SpinTaylor` extension for the O4a detections.

The SNR of a waveform h is given by the square root of the noise weighted inner product $< h, h >$, where:

$$\langle h_1, h_2 \rangle = 2 \int_0^{\infty} \frac{\tilde{h}_1 \tilde{h}_2^* + \tilde{h}_1^* \tilde{h}_2}{S_n(f')} \mathrm{d}f' \tag{4.5}$$

where $\tilde{h}_i$ is the Fourier transform of h_i, whereas S_n characterises the noise profile of the given GW detector. Where this approach is in principle independent of the choice of GW detector, we solely focus on ET (Maggiore et al., 2020; Abac et al., 2025) sensitivity in this work as EEs are expected to only start to become detectable in next-generation GW observatories (Zwick et al., 2025b).

A simple estimate for the detectability of an EE is the so-called δSNR criterion:

$$\delta \mathrm{SNR}^2 \equiv \langle \Delta h, \Delta h \rangle > \mathcal{C}^2, \tag{4.6}$$

$$\Delta h = h_{\mathrm{vac}} - h_{\mathrm{EE}}. \tag{4.7}$$

Here h_{vac} represents the vacuum waveform, while h_{EE} the perturbed waveform with the addition of EE. The threshold $\mathcal{C}$ is commonly chosen to be $\mathcal{O}(10)$ to assure sufficient mismatch. We note that we will supply our parameter space exploration using Eq. 4.6 with several Bayesian parameter inference experiments, as detailed in Sec. 4.5.

In this work, we will also investigate the prospects for distinguishing between different types of EE within the same waveform. Therefore, we introduce the additional concept of a residual SNR between two waveforms enhanced with different EE prescriptions (EE1 and EE2). We dub the concept of ”delta–δSNR”, defined as:

$$\Delta\delta\mathrm{SNR}^2 \equiv \langle \Delta h, \Delta h \rangle > \mathcal{C}^2, \tag{4.8}$$

$$\Delta h = h_{\mathrm{EE1}} - h_{\mathrm{EE2}}. \tag{4.9}$$

This serves as a useful tool to survey large portions of parameter space.

In our application, the two EEs correspond to the following choices. The waveform h_{EE1} incorporates the eccentric dephasing described in Eq. 4.13. The comparison waveform h_{EE2} instead includes a generic dephasing term of the form

$$d\psi = A f^{-13/3}, \tag{4.10}$$

which captures the leading frequency dependence expected from a LOSA. For each realisation of h_{EE1}, we construct h_{EE2} such that both waveforms exhibit the same dephasing amplitude when the binary enters the ET frequency band ($f_{\mathrm{in}} \sim 2\,\mathrm{Hz}$ for our example systems). The constant A is determined by matching $d\psi_{\mathrm{EE2}}$ to $d\psi_{\mathrm{EE1}}$ at this frequency. This procedure provides the ”best-fit” non-eccentric dephasing with the same initial magnitude, thereby allowing the resulting $\Delta\delta$SNR to quantify how distinguishable the true eccentric signal is from its closest generic (non-eccentric) counterpart.

4.3.2 Eccentric Rømer delay dephasing

The effect of dephasing due to Rømer delay has been studied in detail in multiple works (e.g. Yunes et al., 2011; Robson et al., 2018; Samsing et al., 2025; Hendriks et al., 2025; Vijaykumar et al., 2023; Tiwari et al., 2024). Central to this paper is our previous work in Hendriks et al. (2025), where we investigated the Rømer dephasing allowing for *both* the binary orbit and the outer orbit to be eccentric. We note two key findings from this previous work: *i)* an eccentric outer orbit can increase the amount of dephasing with several orders of magnitude compared to its circular equivalent, and *ii)* the outer eccentricity can have clear distinguishable features in the dephasing. These features make the dephasing deviate from the power law in Eq. 4.1.

A first quantification of dephasing from 3-body interactions in realistic globular-cluster-like settings was carried out in Hendriks et al. (2024), showing that specific configurations exist that generate exceptionally large dephasing. A more sophisticated parameter study, carried out in this work, which incorporates eccentricity effects and predicts in more detail the detectability of Rømer dephasing is therefore a logical and necessary next step.

To describe the Rømer dephasing for an eccentric outer orbit, we employ the framework described in Hendriks et al. (2025). We define[2] the Rømer dephasing as

$$d\psi = \frac{2\pi}{c} l(t) f, \tag{4.11}$$

where $l(t)/c$ is the difference in light travel time between the observed binary whose COM is on a curved path (turquoise in Fig. 4.1) and a fictional reference binary with a constant speed (orange in Fig. 4.1). When the outer orbit is circular, the Rømer time delay $l(t)/c$ has a closed analytical form (Meiron et al., 2017; Samsing et al., 2025). In the outer eccentric case, without approximating the local curvature (e.g. via a Taylor expansion), the Rømer delay can only be obtained numerically as its evaluation requires solving the Kepler equation. We find $l(t)/c$ numerically and express it as $l(f)/c$ in terms of the GW frequency f to be able to apply it to a Fourier domain waveform. As mentioned before, we assume that the inspiralling binary is circular, which yields for the inspiral time t (Peters, 1964; Yunes et al., 2009):

$$t_{\text{circ}} = \frac{5\mathcal{M}}{256} G^{-5/3} c^5 (2\pi\mathcal{M}\frac{f}{2})^{-8/3}, \tag{4.12}$$

where $\mathcal{M}$ is the chirp mass, and f the GW frequency. Similar to Eq. 4.3, we here ignore the constant offset t_c which is not important for our SNR es-

---

[2] Note that in our previous work we defined $d\psi = \frac{2\pi}{c} l(t) f_{\text{orb}}$, to make the transition between circular and eccentric binaries smoother. Here we choose the definition in Eq. 4.11, which is the appropriate form for application to full waveform models.

timates.

We also introduce the quantity $F(\omega_0)$, which is a projection factor that depends on the angle ω_0 between the observer and the major axis of the outer ellipse. More explicitly, $F(\omega_0, f) = \cos(\omega_0 + \alpha(t))$ where $\alpha(t)$ is the angle between the $x-$ and $y-$component of the $\mathbf{l}(t)$ vector before the ω_0 rotation is applied to the system. The final form of the Rømer dephasing is then

$$d\psi_R(f) = F(\omega_0)\frac{2\pi}{c}l(f)f, \tag{4.13}$$

which therefore accounts for both eccentricity and projection modifications to the commonly used constant acceleration dephasing prescription.

In this study we assume that the observer lies in the plane of the outer orbit, i.e. $\sin\iota = 1$, where ι is the inclination angle. This idealisation allows the environmental dephasing to be isolated and examined in a controlled manner. It is important to note that this means that the recovered parameters should be treated as lower bounds.

In this work we adopt a sign convention for the true anomaly at merger, ν_m, such that the example in Fig. 4.1 is defined to be positive. Consequently, a negative value (for example, $\nu_m = -\pi/4$) indicates that the binary passes the outer pericentre during its inspiral (given a sufficiently long observation time). The viewing-angle parameter ω_0 in Fig. 4.1 is shown with a negative sign under this convention. A positive value corresponds to the mirror configuration across the semi-major axis of the outer orbit.

We apply the Rømer dephasing externally to the waveform, as follows (Takátsy et al., 2025):

$$\tilde{h}_{\text{pert}}(f) = \tilde{h}_{\text{vac}}(f)\exp[i(-d\psi_R(f))]. \tag{4.14}$$

In Sec. 4.6, we customise the `bilby` waveform by applying a leading-order LOSA dephasing to it according to Bonvin et al. (2017):

$$d\psi(f) = \frac{25}{65536\eta^2}\left(\frac{GM}{c^3}\right)\left(\frac{a}{c}\right)\left(\frac{GM}{c^3}f\right)^{-13/3}, \tag{4.15}$$

where a is the LOSA, M the total mass, and η is the symmetric mass ratio. We apply it to the waveform in the same fashion as Eq. 4.14.

4.3.3 MCMC parameter inference

In this work, we employ two methodologies to perform parameter inference experiments. For the tests performed in Sec. 4.5, we adopt the Newtonian waveforms described in section 4.3.1, supplied by a dephasing prescription for EE. We assume that the binary coalescence time t_c is fixed by a measurement of the merger and ring-down portions of the GW signal, and truncate the waveform when the binary reaches the innermost stable circular orbit. To perform the parameter inference we use Monte-Carlo-Markhov-Chain (MCMC) methods. We employ the convenient sampler `emcee` (Foreman-Mackey et al., 2013), typically running 18 parallel walkers for 10,000 steps. The likelihood $\mathcal{L}$ for the MCMC tests is given by:

$$\mathcal{L}\left(\Theta\right) \propto \exp\left[-\langle h(\Theta) - h(\Theta_{\rm GT}), h(\Theta) - h(\Theta_{\rm GT})\rangle\right] \tag{4.16}$$

where $\Theta_{\rm GT}$ is a vector of "ground-truth" parameters for the injected signal. The noise is stationary and determined by the power spectral density of the given GW detector, which is ET in this work (Maggiore et al., 2020; Abac et al., 2025). To facilitate convergence, we initialise the walkers near the injected true values. This approach also eliminates the need to define priors for the vacuum binary parameters (which is only suitable for high SNR signals. These choices for the initialisation set-up are made purely for convenience and have no impact on the final results unless stated otherwise.

For the parameter inference of the real GW data (Sec. 4.6), we use the open-source code `bilby` (Ashton et al., 2019). This package is also MCMC-based, and has the convenient functionality of easy access to raw data of LVK events and waveforms. For all analyses, our sampler settings are `sampler='dynesty'`, `nlive=1000`, `naccept=60`, `sample='acceptance-walk'`, and `dlogz=0.1`.

4.4 Exploration of parameter space

Before performing parameter estimation tests, we first survey the relevant regions of parameter space. Our goal is to identify where dephasing induced by a constant LOSA can be distinguished from dephasing produced by a tertiary companion on an eccentric outer orbit. To this end, we employ the $\Delta\delta\mathrm{SNR}$ criterion introduced in Sec. 4.3. This metric does not, by itself, guarantee that the two effects are separable in a full Bayesian analysis. Rather, it quantifies whether the residual between the two waveform models carries sufficient power to be observationally detectable. A subsequent Bayesian inference step (Sec. 4.5) is then required to determine whether distinguishability persists once parameter degeneracies are taken into account.

Our methodology is as follows: We consider a representative, high-SNR binary with component masses $m_1 = m_2 = 8, M_\odot$, perturbed by a tertiary companion of mass $m_3 = 10, M_\odot$, and placed at redshift $z = 0.2$. For this system, we compute $\Delta\delta\mathrm{SNR}$ values for waveforms that include a Rømer delay modeled either with the full eccentric prescription (Eq. 4.13) or with the best-fit approximation of the circular version (Eq. 4.10), as described in Sec. 4.3.2. The resulting $\Delta\delta\mathrm{SNR}$ quantifies the residual power between the waveform perturbed by an eccentric outer orbit and that obtained using a constant LOSA.

Our choice of fiducial parameters is motivated by astrophysical considerations and by the need to obtain signals with measurable dephasing. The binary component masses m_1 and m_2 are selected to lie near the peak of the LVK mass distribution, making them representative of the underlying population (The LIGO Scientific Collaboration et al., 2025a,b). These relatively low masses also maximise the accumulated dephasing, which is advantageous for the present study. In dense stellar clusters, three-body encounters are most efficient for nearly equal mass objects (e.g. Kremer et al., 2020; Rodriguez et al., 2022; Morscher et al., 2015), and for this reason we choose a tertiary mass m_3 that is comparable to the binary masses, both in this survey and in the mock inference presented below. The adopted redshift of $z = 0.2$ yields a high SNR for ET, which is required for the dephasing effects to be detectable. This red-

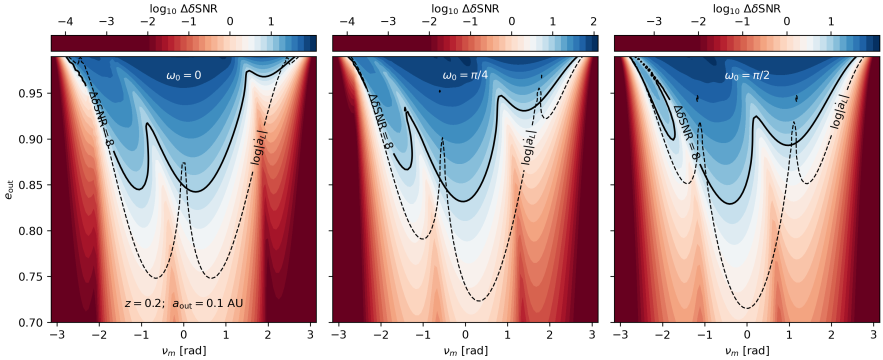

Figure 4.2: $\Delta\delta$SNR contours as a function of outer orbit eccentricity $e_{\rm out}$ and merger true anomaly ν_m, for $m_1 = m_2 = m_3 = 8\ \mathrm{M}_\odot$. The panels show the results for three different choices of ω_0, i.e. three different viewing angles. Typically, the largest residuals occur for mergers just before of just after pericentre, where both acceleration and eccentricity signatures are maximal. The black solid contour represents configurations with $\Delta\delta\mathrm{SNR} = 8$, which is approximately where it becomes distinguishable from circular dephasing. Additionally, we overplot a contour of constant LOSJ (dashed), according to Eq. 4.18.

shift lies well within the expected horizon of ET (Maggiore et al., 2020), and although it does not correspond to the ”typical” detection distance, systems at this redshift are still expected to contribute merger rates of several tens per Gpc^3 per year (The LIGO Scientific Collaboration et al., 2025b). Finally, our fiducial choice of $a_{\rm out} = 0.1$ AU is typical of cluster environments (Antonini & Rasio, 2016). In the sections below we also explore values as small as $a_{\rm out} \sim 0.01$ AU, which remain within the range expected in the densest regions of clusters and are therefore astrophysically well motivated (Samsing & Hotokezaka, 2021).

Figure 4.2 collects some representative results. The panels show $\Delta\delta$SNR contours as a function of the outer-orbit eccentricity and the true anomaly at merger, ν_m, for three choices of the projection angle ω_0, representing here three different viewing angle configurations. Here, low-eccentricity tertiary orbits are effectively indistinguishable from circular ones. Instead, detectable differences emerge in certain regions of high eccentricity, with the precise threshold modulated by ν_m. The largest residuals occur when the merger takes place in a region with strong variation in the LOSA over an inspiral timescale. Typically, this occurs just before or just after pericentre passage, a configuration in which both the instantaneous acceleration and the discrepancy between the eccentric and constant-acceleration dephasing prescriptions are maximised.

In our setup, the measured LOSA expresses itself analytically as

$$a_{\mathrm{L}}(t) = F(\omega_0, \nu(t)) \times Gm_3 \frac{(1 + e_{\mathrm{out}} \cos\nu(t))^2}{p_{\mathrm{out}}^2} , \tag{4.17}$$

where we have used the fact that the orbital radius is $R(\nu) = a_{\mathrm{out}}(1 - e_{\mathrm{out}}^2)/(1 + e_{\mathrm{out}} \cos\nu) = p_{\mathrm{out}}/(1 + e_{\mathrm{out}} \cos\nu)$, with p_{out} the semi-latus rectum. The combined time dependence of the separation R (from the eccentricity) and the multiplicative factor $F(\omega_0, \nu(t))$ (from the projection effects) determines the structure of the measured LOSA. In the limit where the change in LOSA over time is relatively constant, we can write $F(\omega_0, \nu(t)) \approx \cos(\nu + \omega_0)$. The line-of-sight jerk (LOSJ) then becomes

$$\begin{aligned} |\dot{a}_L| \approx \frac{Gm_3}{R^2} \dot{\nu} \Bigg[& \frac{2e_{\mathrm{out}}}{1 + e_{\mathrm{out}} \cos\nu} \sin\nu \cos(\nu + \omega_0) \\ & + \sin(\nu + \omega_0) \Bigg] , \end{aligned} \tag{4.18}$$

with $\dot{\nu} = (Gm_3 p_{\mathrm{out}})^{1/2}/R^2$ from angular momentum conservation. We overlay a contour of constant LOSJ in Fig. 4.2 (evaluated at $\nu = \nu_m$). The imprint of the LOSJ is clearly reflected in the overall morphology of the $\Delta\delta$SNR contours, most notably in the locations of the $\Delta\delta$SNR peaks. In general, and especially at the highest eccentricities, the constant–LOSJ approximation of Eq. 4.18 does not perfectly reproduce the shape of the $\Delta\delta$SNR contours. The contours become visibly skewed relative to the LOSJ prediction, indicating that higher-order derivative of the LOSA contribute appreciably in this regime and that the full model is required for an accurate description.

Figure 4.3 shows how the tertiary pericentre distance $r_{\mathrm{p,out}}$ required to reach $\Delta\delta\mathrm{SNR} = 8$ depends on tertiary mass, assuming $\nu_m = 0$ (i.e., merger at pericentre) and a highly eccentric orbit. The different colours represent three choices for merging binary masses, appropriate for neutron star mergers,

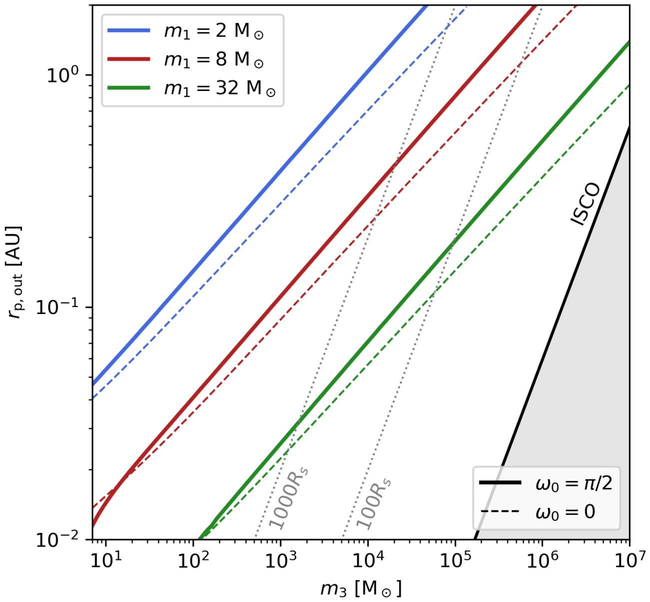

Figure 4.3: Tertiary pericentre distance required to achieve $\Delta\delta\mathrm{SNR} = 8$ for a merger occurring at pericentre ($\nu_m = 0$). Shown are choices for representative masses (colors) and projection angle (dashed lines).

light BBHs and heavy BBHs. The relation is shown for two different choices of ω_0. Note the characteristic scaling $r_{\rm p,out} \propto m_3^{1/2}$ that follows lines of constant acceleration. We also note how measurements of dephasing are in general more easily performed for lighter sources due to the increased number of GW cycles.

Taken together, Figures 4.2 and 4.3, as well as additional analogous calculations, indicate that distinguishing eccentric-induced from circular-induced dephasing is feasible for nearby, low-mass binaries. The corresponding constraints on the triple are:

1. **Tight eccentric triples:** The merging binary must be eccentric and have a pericentre distance that satisfies the results shown in Figure 4.3.
2. **Merger near pericentre:** The merger should occur within approximately $-\frac{\pi}{2} < \nu_m < \frac{\pi}{2}$ for eccentricity effects to be distinguishable.

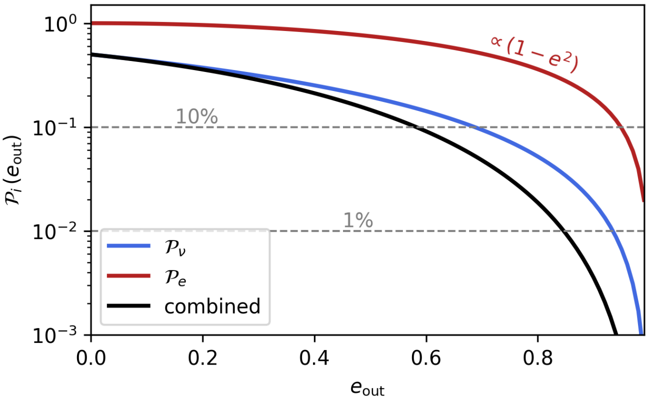

Figure 4.4: Shown are the probability $\mathcal{P}_\nu$ of finding a binary with a true anomaly within $-\frac{\pi}{2}$ and $\frac{\pi}{2}$ as a function of eccentricty, as well as the probability $\mathcal{P}_e$ of finding a binary with $e > e_{\rm out}$, assuming a thermal distribution. These can be used to give an estimate of the fraction of binaries with the properties discussed in Sec. 4.4.

We estimate the number of sources that satisfy these conditions, as well as other constraints. The binary masses used here correspond to the most common BBH mergers observed by LIGO, and we denote by $f_{\rm dyn}$ the fraction formed with a dynamically assembled tertiary. Focusing on the cluster channel, where the tertiary mass is comparable to the binary, detectable dephasing requires pericentre distances $\lesssim 10^{-2}$AU. The overall probability combines the lognormal semimajor–axis distribution between 10^{-2} and 10^3AU (Antonini & Rasio, 2016), a thermal eccentricity distribution, and the likelihood of observing a merger near pericentre. As shown in Fig. 4.4, for a representative semimajor axis of $0.1,$ AU only a few percent of systems satisfy both $e_{\rm out} \gtrsim 0.8$ and $-\frac{\pi}{2} < \nu_m < \frac{\pi}{2}$. Since ET is expected to detect 10^5–10^6 BBH mergers per year (e.g. Maggiore et al., 2020; Regimbau et al., 2012, 2014; Belgacem et al., 2019), of which a few percent lie at high SNR and low redshift, this still yields the possibility of a few to tens of events per year in the relevant part of parameter space after accounting for $f_{\rm dyn}$. The situation is more complex for the AGN channel, for which the eccentricity distribution of binaries around the SMBH is unknown, and most likely suppressed by gas effects. On the other hand, it is very likely that binaries merge in the vicinity of migration traps, which tend to be in a high acceleration region very close to the SMBH. Additionally, other than binaries around the SMBH, these traps might host stellar-mass three-body systems that are tight due to the surrounding gas, which may produce detectable phase shifts (Tagawa et al., 2025).

It is important to emphasise that the $\mathcal{P}_\nu$ distribution shown in Fig. 4.4 is a conservative estimate. While binaries on eccentric outer orbits spend most of their time near apocentre, where the orbital curvature and thus the induced acceleration are weakest, it is not a priori clear whether mergers predominantly occur in this regime. The chaotic nature of three-body interactions often triggers inspirals during close encounters, making mergers at small ν_m values, corresponding to the strong-curvature regime, entirely plausible (Samsing, 2018; Hendriks et al., 2025). Furthermore, although the prior on the outer semi-major axis is taken to be uniform in $\log(a_{\rm out})$ over the range $10^{-2} - 10^3$AU, the subset of systems that actually undergo mergers is preferentially drawn from the small-$a_{\rm out}$ end of this distribution. Such configurations naturally produce smaller pericentre distances, further enhancing the likelihood of mergers occurring in regimes where the induced dephasing is most pronounced.

4.5 Parameter inference of mock events

We here report the results of the parameter inference with the MCMC framework described in Sec. 4.3.3. In this setup we keep the binary parameters, as well as the tertiary mass m_3 fixed: $m_1 = 8M_\odot, m_2 = 8M_\odot, z = 0.2, m_3 = 10M_\odot$.

4.5.1 Inference results

In Figs. 4.5 & 4.6 we show corner plots for the outer orbit parameters of two MCMC runs. We show the results for a run with moderate eccentricity (0.65, Fig. 4.5) and high eccentricity (0.9, Fig. 4.6).

Fig. 4.5 corresponds to a moderately eccentric outer orbit on which the binary inspirals while passing the pericentre of the tertiary's orbit. In this

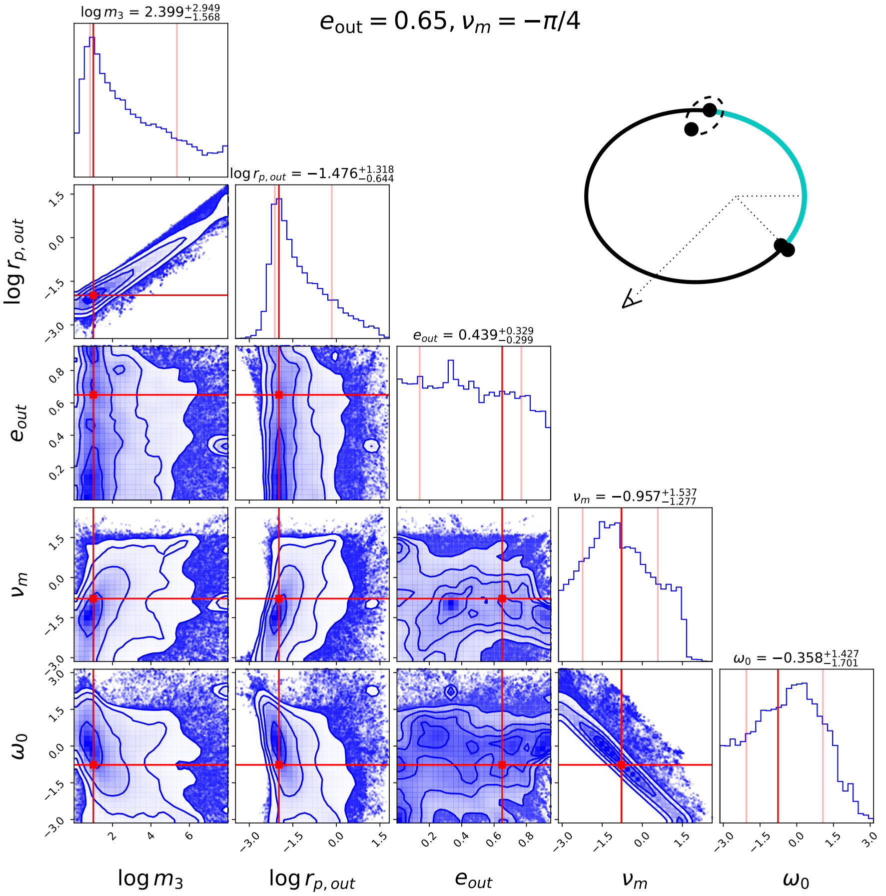

Figure 4.5: Corner plots for 5 outer orbital parameters $m_3, r_{\rm p,out}, e_{\rm out}, \nu_m$, and ω_0 for a three-body system observed by ET. The binary merges beyond pericentre, i.e. $\nu_m = -\pi/4$. We set $e_{\rm out} = 0.65$ and $\omega_0 \sim -\pi/4$. We use $m_1 = 8M_\odot$, $m_2 = 8M_\odot$, $m_3 = 10M_\odot$, $z = 0.2$, and $a_{\rm out} = 0.03$AU. Above the panels, we show the recovered median (50^{th} percentile) and bounds of the 68% credible interval. The same bounds are visualised in the 1-d posteriors in shaded red, as well as the injected true values in bright red.

configuration, according to Eq. 4.18 the projection effects dominate over the eccentricity contribution. The latter can only be dominant in the LOSJ approximation if $\nu_m = -\omega_0$. This signal has an SNR of 87 and is only marginally distinguishable from a vacuum waveform, with δSNR ~ 8.6. Despite $\Delta\delta$SNR ~ 20, meaning that it is clearly distinguishable from a generic LOSA dephasing (Eq. 4.15), no tight constraints on the outer orbital param-

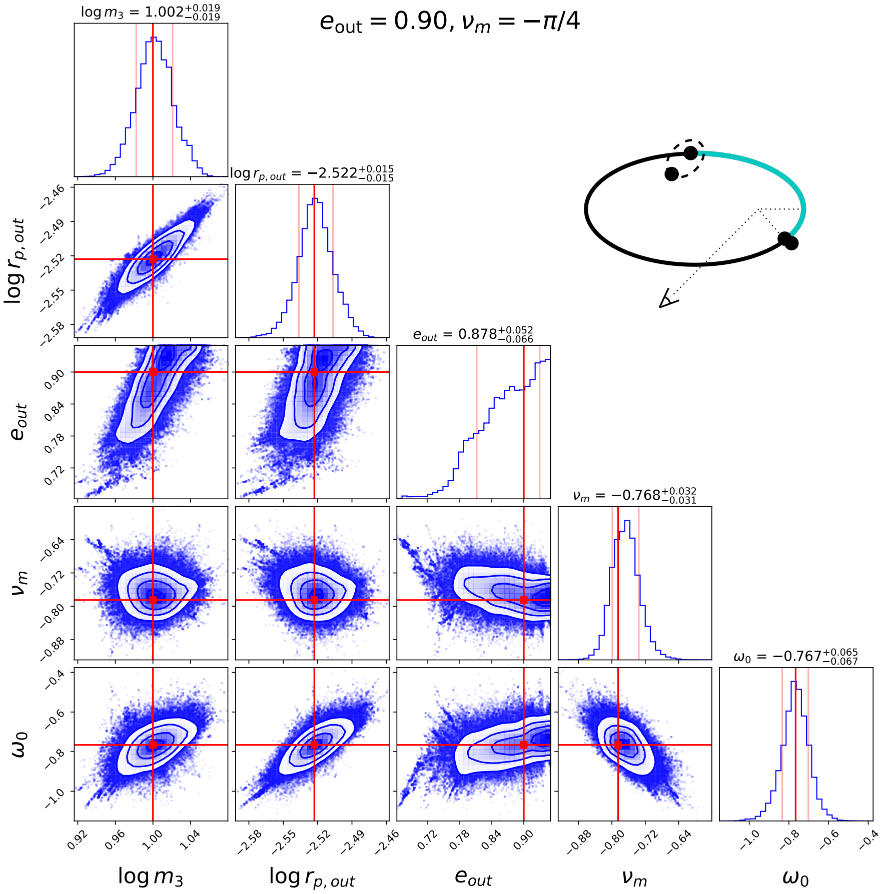

Figure 4.6: Corner plots for 5 outer orbital parameters $m_3, r_{\rm p,out}, e_{\rm out}, \nu_m$, and ω_0 for a three-body system observed by ET. The binary merges beyond pericentre, i.e. $\nu_m = -\pi/4$. We set $e_{\rm out} \sim 0.9$ and $\omega_0 \sim -\pi/4$. We use $m_1 = 8M_\odot$, $m_2 = 8M_\odot$, $m_3 = 10M_\odot$, $z = 0.2$, and $a_{\rm out} = 0.03$AU. Above the panels, we show the recovered median (50^{th} percentile) and bounds of the 68% credible interval. The same bounds are visualised in the 1-d posteriors in shaded red, as well as the injected true values in bright red.

eters can be obtained as the LOSA (Eq. 4.17) does not change significantly over time. Note that this $\Delta\delta$SNR is in agreement with Fig. 4.3, where we see that this system, which has $p_{\rm out} \sim 0.01$AU, lies just below the threshold of distinguishability for the red curve. This highlights that a large $\Delta\delta$SNR alone is insufficient; robust constraints on the outer–orbit parameters additionally require the signal to be measurably distinct from a vacuum waveform, i.e.

to have a sufficiently high δSNR. Importantly, the signal still carries enough power to reveal a clear degeneracy between m_3 and $r_{\rm p,out}$, as well as between ν_m and ω_0, which become identical in the limit of a circular outer orbit. In this configuration, the time variation of the LOSA remains too limited to break these degeneracies. Even so, the data constrain m_3 to be below $\sim 10^5\, M_\odot$, thereby excluding a heavy supermassive black hole companion in this case.

In Fig. 4.6, which corresponds to a highly eccentric outer orbit, the strong time variation of the line of sight acceleration produces a markedly more informative signal. Also here, the projection effects dominate. The event has a ΔSNR ~ 48 and a $\Delta\delta$SNR ~ 34.8, and with $p_{\rm out} \sim 0.003$AU it is well below the detection threshold displayed in Fig. 4.3. The substantial dephasing relative to both the vacuum and generic LOSA waveforms results in significantly tighter constraints on the outer orbital parameters than Fig. 4.5. Most notably, the degeneracy between m_3 and the outer pericentre distance $r_{\rm p,out}$, which is prominent at lower eccentricities, is effectively broken. The tertiary mass and $r_{\rm p,out}$ are now well constrained. Likewise, the degeneracy between ν_m and the projection angle ω_0 is resolved, reflecting the fact that a highly eccentric configuration generates a rapidly evolving LOSA whose curvature carries distinct imprints of both quantities. Overall, the inference shows that for sufficiently eccentric outer orbits in tight 3-body systems the dynamics of the system are encoded strongly enough in the gravitational wave phase evolution that several of the relevant parameters can be recovered with high precision.

4.5.2 Constraining the tertiary mass

In Fig. 4.7 we show how the constraint on the tertiary mass depends on the outer eccentricity for a representative configuration, evaluated for two choices of the viewing orientation, $\omega_0 = 0$ and $\omega_0 = -\pi/4$. In both cases the binary merges at $\nu_m = -\pi/4$. A general trend is apparent: increasing outer eccentricity improves the mass constraint. For both orientations, the posterior on m_3 becomes constrained at the 68 percent level for $e_{\rm out} \gtrsim 0.82$ and at the 90 percent level for $e_{\rm out} \gtrsim 0.87$. At the 68 percent level the AGN channel can be

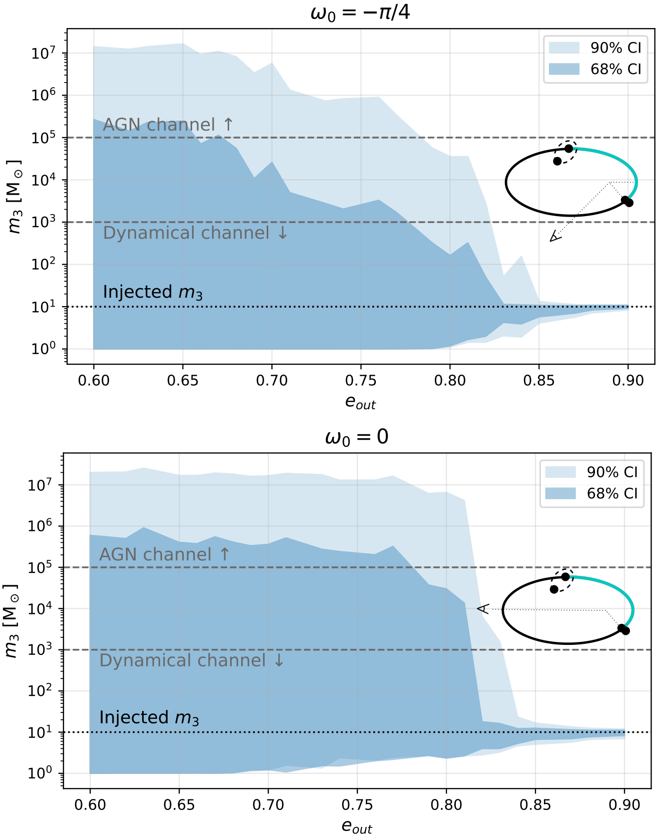

Figure 4.7: 68% and 90% confidence intervals of the recovered tertiary mass as a function of outer eccentricity, for $\omega_0 = -\pi/4$ (top) and $\omega_0 = 0$ (bottom). We use $m_1 = 8M_\odot$, $m_2 = 8M_\odot$, $z = 0.2$, $m_3 = 10M_\odot$, $a_{\rm out} = 0.04$AU, and $\nu_m = -\pi/4$.

excluded for $e_{\rm out} \approx 0.67$ for $\omega_0 = -\pi/4$ and for $e_{\rm out} \approx 0.78$ for $\omega_0 = 0$. A dynamical channel origin can be constrained at $e_{\rm out} \approx 0.73$ for $\omega_0 = -\pi/4$ and $e_{\rm out} \approx 0.82$ for $\omega_0 = 0$.

The two panels exhibit slightly different shapes. For $\omega_0 = 0$ a sharp change appears at high eccentricity that is not present in the top panel which shows a more gradual decrease in CI width. In the $\omega_0 = 0$ orientation, the outer orbit contains a point at $\nu = \pi/2$ where the acceleration vector becomes exactly perpendicular to the line of sight. As a result the projected acceleration drops to zero, which introduces a local decrease in the accumulated dephasing. This behaviour is a clear imprint of projection effects and

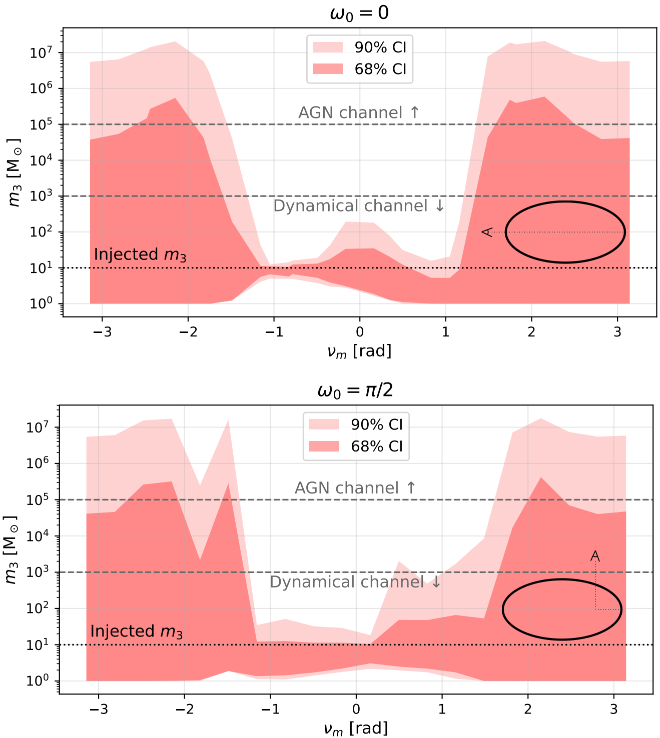

Figure 4.8: 68% and 90% confidence intervals of the recovered tertiary mass as a function of true anomaly at merger ν_m, for $\omega_0 = 0$ (top) and $\omega_0 = \pi/2$ (bottom). We use $m_1 = 8M_\odot$, $m_2 = 8M_\odot$, $z = 0.2$, $m_3 = 10M_\odot$, $a_{\text{out}} = 0.04\text{AU}$, and $e_{\text{out}} = 0.85$.

therefore carries information that assists in constraining the tertiary mass. For eccentricities below approximately $e_{\text{out}} \sim 0.8$ the binary either does not cross $\nu = \pi/2$ within the relevant segment of the orbit or it does so before entering the ET band. Once e_{out} exceeds this value the drop becomes observable in band, producing the corresponding improvement in the mass constraint. This feature underscores the need to model projection effects when extracting dephasing signatures from systems of this kind.

Especially visible in the lower panel, a flattening of the credible intervals toward lower eccentricities (with the 68 percent interval approaching $m_3 \sim 10^6 M_\odot$ and the 90 percent interval $\sim 10^7 M_\odot$) arises from the prior boundaries. Although we adopt broad priors on m_3 in the range 1–$10^8 M_\odot$, systems that are only weakly informative about the tertiary mass naturally accumulate against these limits, producing the apparent saturation in the intervals.

The overall morphology of the credible-interval curves in Fig. 4.8 closely mirrors that seen in Fig. 4.2. For $\omega_0 = 0$ the most informative mergers occur for $\nu_m \sim \pm 1$ rad, offset from pericentre. For $\omega_0 = \pi/2$, mergers closest to pericentre provide the strongest constraint, illustrating that the optimal phase for inference depends on the viewing geometry. Perhaps unexpectedly, Fig. 4.8 also shows that the mass constraint is not significantly degraded at apocentre. Instead, the weakest constraints arise somewhat before and after this point ($\nu_m \sim \pm 2$ rad). This behaviour has a simple underlying explanation: when the binary inspirals near apocentre, the centre of mass undergoes a noticeable change in projected direction, introducing curvature in the line-of-sight acceleration. This time-dependent modulation of the projection factor $F(\omega_0, t)$ provides additional structure in the waveform, allowing the LOSA signature to be more cleanly disentangled and yielding a slightly improved constraint on m_3 compared to configurations immediately adjacent to apocentre. We note that this behaviour differs from that seen in Fig. 4.2, where apocentre configurations produce the poorest constraints. This comparison highlights that individual parameter constraints can exhibit subtleties that are not captured by a global metric such as the $\delta\Delta\mathrm{SNR}$, which effectively marginalises over the full parameter space.

We also note a distinctive feature in the bottom panel in the form of a dip around $\nu_m \simeq -1.8$ rad. This point is noteworthy because it corresponds to a configuration in which the binary enters the detector band precisely as the LOSA becomes perpendicular to the observer, producing the characteristic dip in the accumulated dephasing at the moment when its amplitude is largest. This is the same feature causing the drop in the bottom panel of Fig. 4.7. For ν_m values lower than ~ -1.8 rad, the dip lies outside the observing band, whereas for ν_m slightly higher than this value, the dip shifts to higher frequencies where the dephasing amplitude is smaller, making the effect less pronounced and thereby yielding weaker constraints on m_3. At higher resolution the feature would appear smoother, but its origin and behaviour remain clear.

As established in Sec. 4.4, the regime $-\frac{\pi}{2} \leq \nu_m \leq \frac{\pi}{2}$ (and, for the present configuration, more precisely within ± 1 rad) is where the waveform departs most strongly from a generic LOSA-type dephasing and where the tightest constraints on m_3 are expected. Importantly, however, valuable astrophysical insights can be gained without a full measurement of the tertiary mass. Even the ability to place meaningful upper limits on m_3 is sufficient to rule out or favour specific formation channels, and such constraints can be obtained for systems that are less tightly bound than the fiducial configuration. For example, to constrain the dynamical channel at the 68% level, a merger occurring near pericentre may have an outer semimajor axis larger by a factor of ~ 1.5 than $a_{\rm out} = 0.04\,$AU for $\omega_0 = 0$, and by ~ 2 for $\omega_0 = \pi/2$. Similarly, to exclude the AGN channel, $a_{\rm out}$ can be increased by a factor of ~ 3 for $\omega_0 = 0$ or by ~ 2.75 for $\omega_0 = \pi/2$. These scalings demonstrate that robust constraints on formation pathways can be achieved even when the system is not in the most informative region of parameter space.

4.6 Analysis of GW190814 and O4a events

In this section we discuss the results from our LOSA analysis of several LVK events, most notably GW190814 (Abbott et al., 2020b). Recent work by Yang et al. (2025) reported a LOSA of $0.0015^{+0.0008}_{-0.0008} cs^{-1}$ for this particular event, suggesting the presence of a nearby compact object. Additionally, we analyse 4 events in the LVK O4a catalogue (The LIGO Scientific Collaboration et al., 2025a) which contained reported discrepancies between different waveform models, potentially due to an unmodelled LOSA. For all events, we initially only fit the generic LOSA of Eq. 4.15. Only those events for which we are able to constrain a non-zero acceleration, we would re-analyse with our eccentric dephasing model. We use wide priors for the O4a observations and adopt the GW190814 priors from Yang et al. (2025). For all analyses we assume a uniform prior distribution for the acceleration between $-0.005cs^{-1}$ and $+0.005cs^{-1}$. The noise power spectral densities were obtained for each

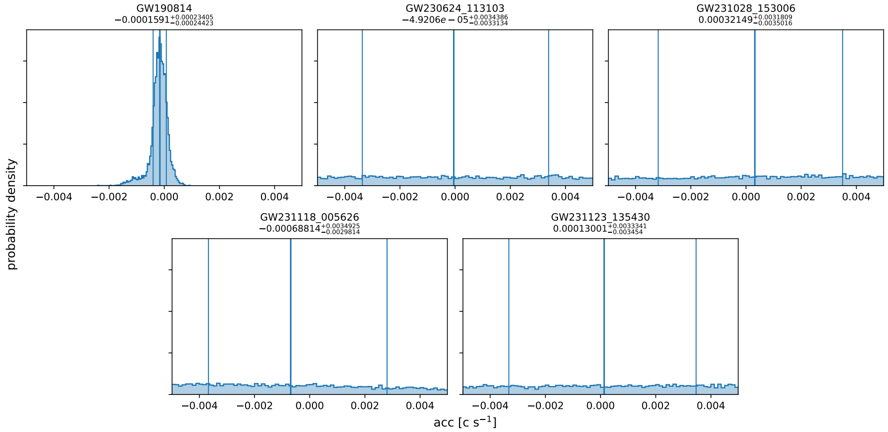

Figure 4.9: Distributions for the inferred LOSA from 5 different GW events. For GW190814 we find a constraint consistent with zero LOSA, while the remaining four events are unconstrained and return the prior distribution. For each panel, the quoted value corresponds to the 50th percentile of the posterior, with uncertainties given by the 16th and 84th percentiles. These percentiles are also indicated within the panels, defining the central 68% credible interval.

individual event directly from the GWTC (`https://gwosc.org/`).

The results are depicted in Fig. 4.9. For the 4 O4a events, our posteriors return the prior distribution. Therefore, we are not able to constrain any LOSA. The dephasing is largest and therefore most easily constrained early in the inspiral at low frequencies (Eq. 4.15). Binaries with low component masses and small mass ratios (non-equal masses) spend more time in this regime and are therefore better candidates for a detection. The 4 LVK events have neither of these properties. With this finding we are able to rule out that the inference discrepancies between different waveform models for these events are caused by a missing LOSA.

For GW190814, the inferred posterior is consistent with no LOSA, with 0 lying within 1-σ of the mean. Importantly, this result is in line with the non-detection reported in Tiwari et al. (2025b) and contradicts the claimed LOSA observation presented in Yang et al. (2025). In reanalysing the data presented in Yang et al. (2025) using identical parameter settings, we successfully reproduce the LOSA reported therein. However, we find that their use of a 4-second signal duration, corresponding to an effective inspiral phase of only

1.6 seconds, is insufficient for analysing a signal of roughly 10 seconds in total inspiral duration (Abbott et al., 2020b). When repeating their analysis with a more appropriate and conservative 32-second segment, we find no evidence for any LOSA in GW190814. Our results therefore demonstrate that the inference reported in Yang et al. (2025) arises from their limited signal window rather than from any genuine physical effect.

4.7 Summary and conclusion

We summarise the main findings of this work below.

- This work introduces a dephasing model required for dynamical three-body interactions that self-consistently treats the full outer orbit, allowing for arbitrary eccentricity and projection effects. By capturing the resulting time-dependent LOSA, the model breaks the fundamental mass–distance degeneracy inherent to constant-acceleration prescriptions and enables constraints on the tertiary mass and orbital parameters.

- Two conditions in the three-body configuration apply in order for eccentric dephasing with projection effects to be distinguishable from generic LOSA dephasing ($\Delta\delta\mathrm{SNR} \gtrsim 8$) with ET sensitivity. Firstly, the outer orbit must be at least appreciably eccentric ($e_{\mathrm{out}} \gtrsim 0.7$) and sufficiently tight, with a semi-major axis of order 0.01 to 0.1 AU for stellar–mass tertiaries. Secondly, the merger must occur close to pericentre, i.e. approximately within the interval $-\frac{\pi}{2} < \nu_m < \frac{\pi}{2}$. In this regime, the LOSA varies most strongly and the eccentric signature is maximally imprinted. Apart from a sufficient $\Delta\delta\mathrm{SNR}$, a detectable eccentric dephasing additionally needs enough power in its $\delta\mathrm{SNR}$ ($\gtrsim 8$) for it to be distinguishable from a vacuum waveform.

- The required ingredients for observable eccentric dephasing and constraining the outer orbital parameters are astrophysically plausible. Under simple assumptions about the semimajor axis and eccentricity distributions of triples in clusters, a few percent of dynamically formed BBH triples satisfy the combined requirements of high outer eccentricity and merger near pericentre. When this fraction is folded together with ET detection forecasts, we still expect a few to tens of events per year in which eccentric Rømer dephasing should be observable, depending on the poorly known fraction $f_{\rm dyn}$ of BBHs assembled in three-body systems.

- For N-body simulations of three-body interactions in dense stellar clusters that produce measurable phase shifts, the relevant parameters to record are the outer true anomaly at merger ν_m, eccentricity $e_{\rm out}$, and semi-major axis $a_{\rm out}$. Characterising the distributions of these quantities will give more accurate predictions for their detection rates and substantially improve our understanding of the dynamical assembly of BHs in three-body systems.

- Across much of the parameter space the tertiary mass cannot be measured precisely but its upper limit can still be tightly constrained, providing strong discriminating power between dynamical and AGN channels. For the slightly optimised but astrophysically plausible configurations explored here, the mass becomes measurable once the outer eccentricity exceeds $e_{\rm out} \sim 0.8$ with $a_{\rm out} = 0.04$AU (i.e. $r_{\rm p,out} \sim 0.008$AU), with the exact threshold depending on the merger true anomaly and the viewing angle. Even at moderate eccentricities ($e_{\rm out} < 0.8$), for mergers near pericentre and for small outer separations, as well as mergers with high $e_{\rm out}$ outside the optimal ν_m range, the recovered upper limit on m_3 can be sufficient to rule out supermassive perturbers in the AGN channel.

- Reanalysis of GW190814 and several O4a events finds no evidence for a LOSA. The previously claimed evidence in GW190814 (Yang et al., 2025) is not reproduced when an appropriate signal duration is used, confirming that the effect is an artefact of an insufficiently long data segment. Additionally, we can rule out that the waveform discrepancies reported in the selected O4a events are caused by an unmodelled LOSA as their inference returns the (flat) prior distributions.

This work opens several avenues for further investigation. A key next step is to incorporate the eccentricity of the inner binary, which is expected to significantly enhance the detectability of Rømer dephasing through the additional harmonic structure of eccentric inspirals (Zwick et al., 2025a; Takátsy et al., 2025). This extension will also allow direct application of the model to LVK events with confirmed non-zero eccentricity. On the astrophysical side, more detailed predictions for the distribution of triple configurations can be obtained through dedicated N-body simulations of dense stellar clusters and, potentially, of three-body interactions in AGN disks. Finally, while our analysis has focused on stellar-mass triples, an analogous injection study with supermassive tertiary companions would shed light on the astrophysical ingredients for detectable dephasing in the AGN channel and the need for using full orbital models. Together, these developments will help build a more complete framework for identifying and directly characterising EEs in GW sources.

Data availability

The data used to complete this study will be shared upon request to the corresponding author.

Acknowledgements

The authors are thankful for insightful discussions with Rico K. L. Lo, which have been extremely helpful in analysing the LVK events. K.H., P.S. and J.S. are supported by the Villum Fonden grant No. 29466, and by the ERC Starting Grant no. 101043143 – BlackHoleMergs. L.Z. is supported by the European Union's Horizon 2024 research and innovation program under the Marie Sklodowska-Curie grant agreement No. 101208914. J.T. is supported by the Alexander von Humboldt Foundation under the project no. 1240213

- HFST-P. The Center of Gravity is a Center of Excellence funded by the Danish National Research Foundation under grant No. 184. The Tycho supercomputer hosted at the SCIENCE HPC center at the University of Copenhagen was used for performing the parameter inference of the LVK events presented in this work. The authors are grateful for their Jupyter notebook epic_ecc_PE_MCMC.ipynb.

Chapter 5

Conclusion

”We all gonna make it bruhz.”

– Lorenz Zwick

How do merging black hole binaries form? In this doctoral thesis, I have shed light on this question by investigating the observable signatures of dynamically formed BBHs and have contributed to the field of GW astrophysics from several different angles.

In Chapter 1, I laid out the premise of this work. After providing a background on GWs and the different formation channels of BBHs, I introduced the concept of EEs. EEs result from interactions between a BBH and its surrounding astrophysical environment and are *directly imprinted* onto the waveform. As opposed to making general population-level predictions, EEs allow us to directly probe the formation environment of individual events. This new approach to the central question is a cornerstone of this thesis. I subsequently introduced the type of EE that is the main focus of this work, namely that of *GW phase shifts due to Rømer time delay*, occurring in 3-body mergers in dynamical environments. A model for the phase shift in highly eccentric binaries with a circular tertiary was derived in our work in Samsing et al. (2025), paving the way for the subsequent studies that I carried out in this thesis.

The mathematical framework of Samsing et al. (2025) was extended in the work outlined in Chapter 2, in which we constructed a semi-analytical model for Rømer dephasing allowing for *both* the inner and outer orbit to be eccentric, which is a realistic scenario in 3-body interactions. We identified the features in the phase shift directly related to the outer orbital eccentricity. We found that the most significant imprints of eccentricity occur when the binary passes the pericentre of the outer orbit during its inspiral. At high outer eccentricities, the phase shift can be orders of magnitude larger than its circular equivalent. We additionally demonstrated that the phase shift can directly be extracted from simulated 3-body mergers, allowing for research into the astrophysical configurations optimising the phase shift.

In Chapter 3 I presented a study in which we investigated the behaviour of the GW phase shift in realistic binary-single scatterings. We performed a controlled set of N-body simulations with configurations representative of interactions in stellar clusters. We found that a subset of the assembled 3-body mergers has a substantial GW phase shift. In a large number of cases, the magnitude of the phase shift would exceed conservative analytical estimates. This is a promising result for current and future GW observatories: if dynamically formed BBHs contribute to the overall merger rate, this hints towards the presence of Rømer delay phase shifts large enough to be observable.

In Chapter 4, we performed a parameter inference study of the phase shift. We presented a further improved model that additionally includes observer projection effects. With parameter-space surveys and mock ET parameter inferences of circular inner binaries, we identified parts of parameter space where the outer orbital parameters, including the tertiary mass m_3, can be constrained and the formation environment can be inferred. Even partial constraints can provide meaningful information about the nature of the third object. Lastly, we found that the claimed detection of a phase shift in GW190814 by Yang et al. (2025) was non-physical, stemming from an insufficiently long duration of the analysed signal.

Taken together, this thesis has demonstrated that Rømer-delay phase shifts, and EEs in general, are a powerful tool to probe BBH formation. Crucially,

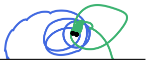

this work shows that Rømer dephasing provides a previously elusive direct link between GW astrophysics and GW data. The phase shift is an observable that can be measured directly in simulations of BBH-producing environments and used immediately in GW signal analysis to assess the observability of the formation mechanism to which it corresponds. Additionally, these results strengthen the scientific potential of next-generation GW observatories. By showing that this EE can reach observable levels, these studies highlight how future detectors will contribute to new knowledge in GW astrophysics.

This work opens up a number of exciting different avenues. From an astrophysical perspective, a natural next step is to characterise in greater detail which 3-body configurations give rise to observable phase shifts. By combining N-body simulations with realistic models of stellar clusters, one can study how varying the parameters of the 3-body scattering influence the behaviour of the phase shift. Distributions of the phase shift for a range of orbital parameters can grant us a better quantitative understanding of the dynamical processes that lead to 3-body mergers. From a observational point of view, there is also more to discover. As eccentricity in binaries is an important indicator of a dynamical origin and a known enhancer of the phase shift (Zwick et al., 2025a; Takátsy et al., 2025), important follow-up work is to study the detectability of phase-shifted eccentric binaries. How much better resolvable is the phase shift if the binary is eccentric? What regimes of 3-body parameters can we probe with eccentric binaries? Could a phase shift be hiding in eccentric BBHs already detected by LVK?

Will we ever fully understand how binary black holes form? Unclear. One certainty, however, is that every incremental step closer towards the answer will reveal more fascinating features of black holes and their pairing mechanisms. And, perhaps more importantly, each new result that we find will spark new questions. As long as we remain curious, the shore of our ignorance will keep growing, and astrophysics will progress. We learn by finding joy in questioning reality. After all, is the uncertainty of everything not exactly what makes us feel reassured?

Appendix A

N-body simulations

The binary-single scatterings which we simulate in Chapter 2 can only be computed numericaly due to their highly chaotic nature. The simulations we adopt use a Post-Newtonian ($\mathcal{PN}$) framework (Blanchet, 2014). In this formalism, the equations of motion (EOM) are written in a series expansion around $1/c$ where c is the speed of light (Samsing et al., 2025). We express the EOM in terms of a pairwise acceleration vector $\underline{a}$:

$$\underline{a} = \underbrace{\underline{a}_0}_{\text{Newt.}} + \underbrace{\underbrace{c^{-2}\underline{a}_2}_{1\mathcal{PN}} + \underbrace{c^{-4}\underline{a}_4}_{2\mathcal{PN}}}_{\text{precession}} + \underbrace{\underbrace{c^{-5}\underline{a}_5}_{2.5\mathcal{PN}}}_{\text{GW rad.}} + \mathcal{O}. \tag{A.1}$$

Here, $\underline{a}$ is the 0^{th}-order classical Newtonian acceleration

$$\underline{a}_0 = \frac{Gm_2}{r^2}\underline{n}, \tag{A.2}$$

and each subsequent acceleration is a higher order contribution. We include the $1\mathcal{PN}$ and $2\mathcal{PN}$ terms that model apsidal precession, as well as the important $2.5\mathcal{PN}$ term which is the leading-order GW radiation contribution that models energy and angular momentum dissipation away from the system. Each of these terms is crucial for accurately modelling the 3-body dynamics in a binary-single scattering eventually leading to a bound merger (Saini et al., 2025). Explicitly,

$$\begin{aligned}\underline{a}_2 = \frac{Gm_2}{r^2}\Big(\underline{n}\Big[&-v_1^2 - 2v_2^2 + 4v_1v_2 + \frac{3}{2}(nv_2)^2 + \\ &5\frac{Gm_1}{r} + 4\frac{Gm_2}{r}\Big] + (\underline{v}_1 - \underline{v}_2)\big[4nv_1 - 3nv_2\big]\Big),\end{aligned} \tag{A.3}$$

$$\begin{aligned}\underline{a}_4 = \frac{Gm_2}{r^2}\Big(\underline{n}\Big[&-2v_2^4 + 4v_2^2(v_1v_2) - 2(v_1v_2)^2 \\ &+ \frac{3}{2}v_1^2(nv_2)^2 + \frac{9}{2}v_2^2(nv_2)^2 - 6(v_1v_2)(nv_2)^2 \\ &- \frac{15}{8}(nv_2)^4 + \frac{Gm_1}{r}\Big(-\frac{15}{4}v_1^2 + \frac{5}{4}v_2^2 - \frac{5}{2}v_1v_2 \\ &+ \frac{39}{2}(nv_1)^2 - 39(nv_1)(nv_2) + \frac{17}{2}(nv_2)^2\Big) \\ &+ \frac{Gm_2}{r}(4v_2^2 - 8v_1v_2 + 2(nv_1)^2 \\ &- 4(nv_1)(nv_2) - 6(nv_2)^2)\Big] \\ &+ (\underline{v}_1 - \underline{v}_2)\Big[v_1^2(nv_2) + 4v_2^2(nv_1) - 5v_2^2(nv_2) \\ &- 4(v_1v_2)(nv_1) + 4(v_1v_2)(nv_2) - 6(nv_1)(nv_2)^2 \\ &+ \frac{9}{2}(nv_2)^3 + \frac{Gm_1}{r}\Big(-\frac{63}{4}nv_1 + \frac{55}{4}nv_2\Big) \\ &+ \frac{Gm_2}{r}\big(-2nv_1 - 2nv_2\big)\Big]\Big) \\ &+ \frac{G^3m_2}{r^4}\Big(\underline{n}\Big[-\frac{57}{4}m_1^2 - 9m_2^2 - \frac{69}{2}m_1m_2\Big]\Big),\end{aligned} \tag{A.4}$$

and the last term, $\underline{a}_5$, is the leading term in the series that is dissipative ($2.5\mathcal{PN}$), which results in pairwise energy and angular momentum loss through the emission of GWs,

$$\begin{aligned}\underline{a}_5 = \frac{4}{5}\frac{G^2m_1m_2}{r^3}\Big(&(\underline{v}_1 - \underline{v}_2)\Big[-(\underline{v}_1 - \underline{v}_2)^2 \\ &+ 2\frac{Gm_1}{r} - 8\frac{Gm_2}{r}\Big] \\ &+ \underline{n}(nv_1 - nv_2)\Big[3(\underline{v}_1 - \underline{v}_2)^2 - 6\frac{Gm_1}{r} + \frac{52}{3}\frac{Gm_2}{r}\Big]\Big).\end{aligned} \tag{A.5}$$

In the above equations $\underline{a}$ is the acceleration vector from some object '1' to another object '2'. The quantities m_i and $\underline{v}_i$ respectively denote the mass and velocity vector of object 'i'. r is the absolute distance between the 2 objects, $\underline{n}$ is the unit vector pointing from object '2' to '1', and $x_1 x_2$ represents the dot product between two arbitrary vectors x_1 and x_2. Since the acceleration is evaluated in a pairwise fashion, the velocities correspond to the velocities relative to the COM of the pair.

One has to calculate the acceleration between *each pair of objects* in the simulation, i.e. between each pair of the 3 BHs in the work of Chapter 2. Eq. A.1 is in its essence a differential equation for the pairwise position $\underline{r}$ which needs to be solved numerically in order to evolve the system in time and monitor the interaction between the 3 BHs. To do this we use the well-established N-body code from Samsing et al. (2014, 2017); Samsing & Ilan (2018); Samsing et al. (2022). This code uses the Livermore Solver for Ordinary Differential Equations (LSODE, Hindmarsh (1983); Radhakrishnan & Hindmarsh (1993)) to solve the differential equations with variable order and variable time-stepping. The output of the code is a time series of the positions and velocities of the individual objects.

Bibliography

Aasi, J., et al. 2015, Class. Quant. Grav., 32, 074001, doi: 10.1088/0264-9381/32/7/074001

Abac, A., Abramo, R., Albanesi, S., et al. 2025, arXiv e-prints, arXiv:2503.12263, doi: 10.48550/arXiv.2503.12263

Abac, A. G., Abbott, R., Abe, H., et al. 2024, ApJ, 973, 132, doi: 10.3847/1538-4357/ad65ce

Abbott, B. P., & et al. 2019, Physical Review X, 9, 031040, doi: 10.1103/PhysRevX.9.031040

Abbott, B. P., Abbott, R., Abbott, T. D., et al. 2016, Phys. Rev. Lett., 116, 061102, doi: 10.1103/PhysRevLett.116.061102

Abbott, B. P., Abbott, R., Abbott, T. D., et al. 2018, Living Reviews in Relativity, 21, 3, doi: 10.1007/s41114-018-0012-9

—. 2019a, ApJL, 882, L24, doi: 10.3847/2041-8213/ab3800

—. 2019b, ApJ, 883, 149, doi: 10.3847/1538-4357/ab3c2d

Abbott, R., Abbott, T. D., Abraham, S., et al. 2020a, Phys. Rev. Lett., 125, 101102, doi: 10.1103/PhysRevLett.125.101102

—. 2020b, ApJL, 896, L44, doi: 10.3847/2041-8213/ab960f

Abbott, R., Abe, H., Acernese, F., et al. 2023, ApJS, 267, 29, doi: 10.3847/1538-4365/acdc9f

Abbott, R., Abbott, T. D., Acernese, F., et al. 2024, Phys. Rev. D, 109, 022001, doi: `10.1103/PhysRevD.109.022001`

Acernese, F., Agathos, M., Agatsuma, K., et al. 2015, Classical and Quantum Gravity, 32, 024001, doi: `10.1088/0264-9381/32/2/024001`

Agazie, G., Anumarlapudi, A., Archibald, A. M., et al. 2023, ApJL, 951, L8, doi: `10.3847/2041-8213/acdac6`

Akutsu, T., et al. 2019, Nature Astron., 3, 35, doi: `10.1038/s41550-018-0658-y`

Amaro-Seoane, P., Audley, H., Babak, S., et al. 2017, arXiv e-prints, arXiv:1702.00786, doi: `10.48550/arXiv.1702.00786`

Amaro-Seoane, P., Andrews, J., Arca Sedda, M., et al. 2023, Living Reviews in Relativity, 26, 2, doi: `10.1007/s41114-022-00041-y`

Antognini, J. M. O., & Thompson, T. A. 2016, MNRAS, 456, 4219, doi: `10.1093/mnras/stv2938`

Antoni, A., MacLeod, M., & Ramirez-Ruiz, E. 2019, ApJ, 884, 22, doi: `10.3847/1538-4357/ab3466`

Antonini, F., Chatterjee, S., Rodriguez, C. L., et al. 2016, ApJ, 816, 65, doi: `10.3847/0004-637X/816/2/65`

Antonini, F., & Rasio, F. A. 2016, ApJ, 831, 187, doi: `10.3847/0004-637X/831/2/187`

Arca Sedda, M., Li, G., & Kocsis, B. 2021, A&A, 650, A189, doi: `10.1051/0004-6361/202038795`

Ashton, G., et al. 2019, Astrophys. J. Suppl., 241, 27, doi: `10.3847/1538-4365/ab06fc`

Askar, A., Szkudlarek, M., Gondek-Rosińska, D., Giersz, M., & Bulik, T. 2017, MNRAS, 464, L36, doi: `10.1093/mnrasl/slw177`

Atallah, D., Trani, A. A., Kremer, K., et al. 2023, MNRAS, 523, 4227, doi: 10.1093/mnras/stad1634

Backer, D. C., & Hellings, R. W. 1986, Annual Review of Astronomy and Astrophysics, 24, 537–575, doi: 10.1146/annurev.aa.24.090186.002541

Bae, Y.-B., Kim, C., & Lee, H. M. 2014, MNRAS, 440, 2714, doi: 10.1093/mnras/stu381

Banerjee, S., Baumgardt, H., & Kroupa, P. 2010, MNRAS, 402, 371, doi: 10.1111/j.1365-2966.2009.15880.x

Barausse, E., Cardoso, V., & Pani, P. 2014, Phys. Rev. D, 89, 104059, doi: 10.1103/PhysRevD.89.104059

Barausse, E., & Rezzolla, L. 2008, Phys. Rev. D, 77, 104027, doi: 10.1103/PhysRevD.77.104027

Bartos, I., Kocsis, B., Haiman, Z., & Márka, S. 2017, ApJ, 835, 165, doi: 10.3847/1538-4357/835/2/165

Basu, P., Chatterjee, S., & Mondal, S. 2024, MNRAS, 531, 1506, doi: 10.1093/mnras/stae1239

Bavera, S. S., Fragos, T., Zevin, M., et al. 2021, A&A, 647, A153, doi: 10.1051/0004-6361/202039804

Belczynski, K., Holz, D. E., Bulik, T., & O'Shaughnessy, R. 2016a, Nature, 534, 512, doi: 10.1038/nature18322

Belczynski, K., Repetto, S., Holz, D. E., et al. 2016b, ApJ, 819, 108, doi: 10.3847/0004-637X/819/2/108

Belgacem, E., Dirian, Y., Foffa, S., et al. 2019, JCAP, 2019, 015, doi: 10.1088/1475-7516/2019/08/015

Bellovary, J. M., Mac Low, M.-M., McKernan, B., & Ford, K. E. S. 2016, apjl, 819, L17, doi: 10.3847/2041-8205/819/2/L17

Binney, J., & Tremaine, S. 2008, Galactic dynamics: Second Edition (Princeton: Princeton University Press)

Bird, S., Cholis, I., Muñoz, J. B., et al. 2016, Physical Review Letters, 116, 201301, doi: `10.1103/PhysRevLett.116.201301`

Blanchet, L. 2014, Living Reviews in Relativity, 17, 2, doi: `10.12942/lrr-2014-2`

Bonetti, M., Barausse, E., Faye, G., Haardt, F., & Sesana, A. 2017, Classical and Quantum Gravity, 34, 215004, doi: `10.1088/1361-6382/aa8da5`

Bonvin, C., Caprini, C., Sturani, R., & Tamanini, N. 2017, Phys. Rev. D, 95, 044029, doi: `10.1103/PhysRevD.95.044029`

Camilloni, F., Grignani, G., Harmark, T., et al. 2023, Phys. Rev. D, 107, 084011, doi: `10.1103/PhysRevD.107.084011`

Camilloni, F., Harmark, T., Grignani, G., Orselli, M., & Pica, D. 2024, MNRAS, 531, 1884, doi: `10.1093/mnras/stae1093`

Caneva Santoro, G., Roy, S., Vicente, R., et al. 2024, Phys. Rev. Lett., 132, 251401, doi: `10.1103/PhysRevLett.132.251401`

Caputo, A., Sberna, L., Toubiana, A., et al. 2020, ApJ, 892, 90, doi: `10.3847/1538-4357/ab7b66`

Cardoso, V., Destounis, K., Duque, F., Macedo, R. P., & Maselli, A. 2022, Phys. Rev. Lett., 129, 241103, doi: `10.1103/PhysRevLett.129.241103`

Cardoso, V., & Maselli, A. 2020, A&A, 644, A147, doi: `10.1051/0004-6361/202037654`

Carr, B., Kühnel, F., & Sandstad, M. 2016, Phys. Rev. D, 94, 083504, doi: `10.1103/PhysRevD.94.083504`

Castelvecchi, D. 2018, Nature, 556, 164, doi: `10.1038/d41586-018-04157-6`

Chakrabarti, S. K. 1993, ApJ, 411, 610, doi: 10.1086/172863

Chamberlain, K., Moore, C. J., Gerosa, D., & Yunes, N. 2019, Phys. Rev. D, 99, 024025, doi: 10.1103/PhysRevD.99.024025

Chandramouli, R. S., & Yunes, N. 2022, Phys. Rev. D, 105, 064009, doi: 10.1103/PhysRevD.105.064009

Chen, X. 2021, in Handbook of Gravitational Wave Astronomy, 39, doi: 10.1007/978-981-15-4702-7_39-1

Cholis, I., Kovetz, E. D., Ali-Haïmoud, Y., et al. 2016, Phys. Rev. D, 94, 084013, doi: 10.1103/PhysRevD.94.084013

Cole, P. S., Coogan, A., Kavanagh, B. J., & Bertone, G. 2023, Phys. Rev. D, 107, 083006, doi: 10.1103/PhysRevD.107.083006

Cutler, C., & Flanagan, É. E. 1994, Phys. Rev. D, 49, 2658, doi: 10.1103/PhysRevD.49.2658

Damour, T., & Deruelle, N. 1985, Annales de L'Institut Henri Poincare Section (A) Physique Theorique, 43, 107. https://ui.adsabs.harvard.edu/abs/1985AIHPA..43..107D

Derdzinski, A., D'Orazio, D., Duffell, P., Haiman, Z., & MacFadyen, A. 2021, MNRAS, 501, 3540, doi: 10.1093/mnras/staa3976

Destounis, K., Kulathingal, A., Kokkotas, K. D., & Papadopoulos, G. O. 2023, Phys. Rev. D, 107, 084027, doi: 10.1103/PhysRevD.107.084027

Dominik, M., Belczynski, K., Fryer, C., et al. 2012, ApJ, 759, 52, doi: 10.1088/0004-637X/759/1/52

—. 2013, ApJ, 779, 72, doi: 10.1088/0004-637X/779/1/72

Dominik, M., Berti, E., O'Shaughnessy, R., et al. 2015, ApJ, 806, 263, doi: 10.1088/0004-637X/806/2/263

D'Orazio, D. J., & Loeb, A. 2018, Phys. Rev. D, 97, 083008, doi: 10.1103/PhysRevD.97.083008

—. 2020, Phys. Rev. D, 101, 083031, doi: 10.1103/PhysRevD.101.083031

Duque, F., Kejriwal, S., Sberna, L., Speri, L., & Gair, J. 2025, Phys. Rev. D, 111, 084006, doi: 10.1103/PhysRevD.111.084006

Dyson, C., Redondo-Yuste, J., van de Meent, M., & Cardoso, V. 2024, Phys. Rev. D, 109, 104038, doi: 10.1103/PhysRevD.109.104038

Einstein, A. 1915, Sitzungsberichte der Königlich Preussischen Akademie der Wissenschaften, 844

Evans, M., Corsi, A., Afle, C., et al. 2023, arXiv e-prints, arXiv:2306.13745, doi: 10.48550/arXiv.2306.13745

Event Horizon Telescope Collaboration, Akiyama, K., Alberdi, A., et al. 2019, ApJL, 875, L1, doi: 10.3847/2041-8213/ab0ec7

Ezquiaga, J. M., Holz, D. E., Hu, W., Lagos, M., & Wald, R. M. 2021, Phys. Rev. D, 103, 064047, doi: 10.1103/PhysRevD.103.064047

Fabj, G., & Samsing, J. 2024, MNRAS, 535, 3630, doi: 10.1093/mnras/stae2499

Fabj, G., Tiede, C., Rowan, C., Pessah, M., & Samsing, J. 2025, arXiv e-prints, arXiv:2510.07952, doi: 10.48550/arXiv.2510.07952

Farr, W. M., Stevenson, S., Miller, M. C., et al. 2017, Nature, 548, 426, doi: 10.1038/nature23453

Foreman-Mackey, D., Hogg, D. W., Lang, D., & Goodman, J. 2013, PASP, 125, 306, doi: 10.1086/670067

Fumagalli, G., Loutrel, N., Gerosa, D., & Boschini, M. 2025, Phys. Rev. D, 112, 024012, doi: 10.1103/znmj-6wvt

García-Bellido, J., Nuño Siles, J. F., & Ruiz Morales, E. 2021, Physics of the Dark Universe, 31, 100791, doi: 10.1016/j.dark.2021.100791

Garg, M., Derdzinski, A., Zwick, L., Capelo, P. R., & Mayer, L. 2022, MNRAS, 517, 1339, doi: 10.1093/mnras/stac2711

Gayathri, V., Healy, J., Lange, J., et al. 2022, Nature Astronomy, 6, 344, doi: 10.1038/s41550-021-01568-w

Gerosa, D., & Berti, E. 2017, Phys. Rev. D, 95, 124046, doi: 10.1103/PhysRevD.95.124046

Gondán, L., & Kocsis, B. 2022, MNRAS, 515, 3299, doi: 10.1093/mnras/stac1985

Gültekin, K., Miller, M. C., & Hamilton, D. P. 2006, ApJ, 640, 156

Hamers, A. S., Bar-Or, B., Petrovich, C., & Antonini, F. 2018, ApJ, 865, 2, doi: 10.3847/1538-4357/aadae2

Hamers, A. S., & Thompson, T. A. 2019, ApJ, 883, 23, doi: 10.3847/1538-4357/ab3b06

Hansen, R. O. 1972, Physical Review D, 5, 1021, doi: 10.1103/PhysRevD.5.1021

Heger, A., Fryer, C. L., Woosley, S. E., Langer, N., & Hartmann, D. H. 2003, ApJ, 591, 288, doi: 10.1086/375341

Heggie, D. C. 1975, in IAU Symposium, Vol. 69, Dynamics of the Solar Systems, ed. A. Hayli, 73

Hendriks, K., Zwick, L., & Samsing, J. 2025, ApJ, 985, 252, doi: 10.3847/1538-4357/adcb35

Hendriks, K., Atallah, D., Martinez, M., et al. 2024, arXiv e-prints, arXiv:2411.08572, doi: 10.48550/arXiv.2411.08572

Hindmarsh, A. C. 1983, in IMACS Transactions on Scientific Computation, Vol. 1, Scientific Computing, ed. R. S. Stepleman et al. (Amsterdam: North-Holland), 55–64

Hoang, B.-M., Naoz, S., Kocsis, B., Rasio, F. A., & Dosopoulou, F. 2018, ApJ, 856, 140, doi: `10.3847/1538-4357/aaafce`

Hong, J., & Lee, H. M. 2015, MNRAS, 448, 754, doi: `10.1093/mnras/stv035`

Hotokezaka, K., & Piran, T. 2017, ApJ, 842, 111, doi: `10.3847/1538-4357/aa6f61`

Hu, W.-R., & Wu, Y.-L. 2017, National Science Review, 4, 685, doi: `10.1093/nsr/nwx116`

Hut, P. 1983, AJ, 88, 1549, doi: `10.1086/113445`

Hut, P., & Bahcall, J. N. 1983, ApJ, 268, 319

Inayoshi, K., Hirai, R., Kinugawa, T., & Hotokezaka, K. 2017a, MNRAS, 468, 5020, doi: `10.1093/mnras/stx757`

Inayoshi, K., Tamanini, N., Caprini, C., & Haiman, Z. 2017b, Phys. Rev. D, 96, 063014, doi: `10.1103/PhysRevD.96.063014`

Iorio, G., Mapelli, M., Costa, G., et al. 2023, MNRAS, 524, 426, doi: `10.1093/mnras/stad1630`

Janiuk, A., Bejger, M., Charzyński, S., & Sukova, P. 2017, ArXiv e-prints, 51, 7, doi: `10.1016/j.newast.2016.08.002`

Kagra Collaboration, Akutsu, T., Ando, M., et al. 2019, Nature Astronomy, 3, 35, doi: `10.1038/s41550-018-0658-y`

Kalogera, V. 2000, ApJ, 541, 319, doi: `10.1086/309400`

Kawamura, S., Ando, M., Seto, N., et al. 2011, Classical and Quantum Gravity, 28, 094011, doi: `10.1088/0264-9381/28/9/094011`

Kocsis, B., Yunes, N., & Loeb, A. 2011, Phys. Rev. D, 84, 024032, doi: 10.1103/PhysRevD.84.024032

Kremer, K., Ye, C. S., Rui, N. Z., et al. 2020, ApJS, 247, 48, doi: 10.3847/1538-4365/ab7919

Kushnir, D., Zaldarriaga, M., Kollmeier, J. A., & Waldman, R. 2016, MNRAS, 462, 844, doi: 10.1093/mnras/stw1684

Laeuger, A., Seymour, B., Chen, Y., & Yu, H. 2024, Phys. Rev. D, 109, 064086, doi: 10.1103/PhysRevD.109.064086

Lee, W. H., Ramirez-Ruiz, E., & van de Ven, G. 2010, ApJ, 720, 953

Levin, Y. 2007, MNRAS, 374, 515, doi: 10.1111/j.1365-2966.2006.11155.x

Li, G., Naoz, S., Kocsis, B., & Loeb, A. 2014, ApJ, 785, 116, doi: 10.1088/0004-637X/785/2/116

LIGO Scientific Collaboration, Aasi, J., Abbott, B. P., et al. 2015, Classical and Quantum Gravity, 32, 074001, doi: 10.1088/0264-9381/32/7/074001

Liu, B., D'Orazio, D. J., Vigna-Gómez, A., & Samsing, J. 2022, Phys. Rev. D, 106, 123010, doi: 10.1103/PhysRevD.106.123010

Liu, B., & Lai, D. 2018, ApJ, 863, 68, doi: 10.3847/1538-4357/aad09f

—. 2021, MNRAS, 502, 2049, doi: 10.1093/mnras/stab178

Liu, B., Lai, D., & Wang, Y.-H. 2019a, ApJL, 883, L7, doi: 10.3847/2041-8213/ab40c0

—. 2019b, ApJ, 881, 41, doi: 10.3847/1538-4357/ab2dfb

Liu, B., Muñoz, D. J., & Lai, D. 2015, MNRAS, 447, 747, doi: 10.1093/mnras/stu2396

Liu, S., Hu, Y.-M., Zhang, J.-d., & Mei, J. 2020, Phys. Rev. D, 101, 103027, doi: 10.1103/PhysRevD.101.103027

Lo, R. K. L., Vujeva, L., Ezquiaga, J. M., & Chan, J. C. L. 2025, Phys. Rev. Lett., 134, 151401, doi: 10.1103/PhysRevLett.134.151401

Loeb, A. 2016, ApJL, 819, L21, doi: 10.3847/2041-8205/819/2/L21

Luo, J., Chen, L.-S., Duan, H.-Z., et al. 2016, Classical and Quantum Gravity, 33, 035010, doi: 10.1088/0264-9381/33/3/035010

Maggiore, M. 2007, Gravitational Waves: Volume 1: Theory and Experiments, doi: 10.1093/acprof:oso/9780198570745.001.0001

Maggiore, M., Van Den Broeck, C., Bartolo, N., et al. 2020, JCAP, 2020, 050, doi: 10.1088/1475-7516/2020/03/050

Magorrian, J., Tremaine, S., Richstone, D., et al. 1998, AJ, 115, 2285, doi: 10.1086/300353

Mandel, I., & de Mink, S. E. 2016, MNRAS, 458, 2634, doi: 10.1093/mnras/stw379

Mandel, I., & Farmer, A. 2017, Nature, 547, 284, doi: 10.1038/547284a

—. 2022, Phys. Rep., 955, 1, doi: 10.1016/j.physrep.2022.01.003

Martin Barandiaran, M., Kuroyanagi, S., & Nesseris, S. 2024, Classical and Quantum Gravity, 41, 095002, doi: 10.1088/1361-6382/ad36a7

McKernan, B., & Ford, K. E. S. 2024, MNRAS, 531, 3479, doi: 10.1093/mnras/stae1351

McKernan, B., Ford, K. E. S., Bellovary, J., et al. 2018, The Astrophysical Journal, 866, 66, doi: 10.3847/1538-4357/aadae5

Meiron, Y., Kocsis, B., & Loeb, A. 2017, ApJ, 834, 200, doi: 10.3847/1538-4357/834/2/200

Memmesheimer, R.-M., Gopakumar, A., & Schäfer, G. 2004, Physical Review D, 70, 104011, doi: 10.1103/PhysRevD.70.104011

Miller, M. C., & Yunes, N. 2019, Nature, 568, 469, doi: 10.1038/s41586-019-1129-z

Moore, C. J., Cole, R. H., & Berry, C. P. L. 2015, Classical and Quantum Gravity, 32, 015014, doi: 10.1088/0264-9381/32/1/015014

Morscher, M., Pattabiraman, B., Rodriguez, C., Rasio, F. A., & Umbreit, S. 2015, ApJ, 800, 9, doi: 10.1088/0004-637X/800/1/9

Murguia-Berthier, A., MacLeod, M., Ramirez-Ruiz, E., Antoni, A., & Macias, P. 2017, ApJ, 845, 173, doi: 10.3847/1538-4357/aa8140

Naoz, S., Kocsis, B., Loeb, A., & Yunes, N. 2013, ApJ, 773, 187, doi: 10.1088/0004-637X/773/2/187

Netzer, H. 2013, The Physics and Evolution of Active Galactic Nuclei

Nitz, A., Harry, I., Brown, D., et al. 2024, gwastro/pycbc: v2.3.3 release of PyCBC, Zenodo, doi: 10.5281/ZENODO.10473621

O'Leary, R. M., Kocsis, B., & Loeb, A. 2009, MNRAS, 395, 2127, doi: 10.1111/j.1365-2966.2009.14653.x

O'Neill, D., D'Orazio, D. J., Samsing, J., & Pessah, M. E. 2024, ApJ, 974, 216, doi: 10.3847/1538-4357/ad7250

Oppenheimer, J. R., & Snyder, H. 1939, Physical Review, 56, 455, doi: 10.1103/PhysRev.56.455

Park, D., Kim, C., Lee, H. M., Bae, Y.-B., & Belczynski, K. 2017, MNRAS, 469, 4665, doi: 10.1093/mnras/stx1015

Peters, P. C. 1964, Physical Review, 136, 1224, doi: 10.1103/PhysRev.136.B1224

Peters, P. C., & Mathews, J. 1963, Physical Review, 131, 435, doi: `10.1103/PhysRev.131.435`

Petiteau, A., Babak, S., Sesana, A., & de Araújo, M. 2013, Phys. Rev. D, 87, 064036, doi: `10.1103/PhysRevD.87.064036`

Pijnenburg, M., Cusin, G., Pitrou, C., & Uzan, J.-P. 2024, Phys. Rev. D, 110, 044054, doi: `10.1103/PhysRevD.110.044054`

Portegies Zwart, S. F., & McMillan, S. L. W. 2000, ApJL, 528, L17, doi: `10.1086/312422`

Pratten, G., García-Quirós, C., Colleoni, M., et al. 2021, Phys. Rev. D, 103, 104056, doi: `10.1103/PhysRevD.103.104056`

Radhakrishnan, K., & Hindmarsh, A. C. 1993, Description and Use of LSODE, the Livermore Solver for Ordinary Differential Equations, Tech. Rep. UCRL-ID-113855, Lawrence Livermore National Laboratory

Ramirez-Ruiz, E., Trenti, M., MacLeod, M., et al. 2015, ApJL, 802, L22, doi: `10.1088/2041-8205/802/2/L22`

Randall, L., & Xianyu, Z.-Z. 2018, ApJ, 864, 134, doi: `10.3847/1538-4357/aad7fe`

—. 2019a, ApJ, 878, 75, doi: `10.3847/1538-4357/ab20c6`

—. 2019b, arXiv e-prints, arXiv:1902.08604, doi: `10.48550/arXiv.1902.08604`

Regimbau, T., Meacher, D., & Coughlin, M. 2014, Phys. Rev. D, 89, 084046, doi: `10.1103/PhysRevD.89.084046`

Regimbau, T., Dent, T., Del Pozzo, W., et al. 2012, Phys. Rev. D, 86, 122001, doi: `10.1103/PhysRevD.86.122001`

Reitze, D., Adhikari, R. X., Ballmer, S., et al. 2019, in Bulletin of the American Astronomical Society, Vol. 51, 35, doi: `10.48550/arXiv.1907.04833`

Robson, T., Cornish, N. J., Tamanini, N., & Toonen, S. 2018, Phys. Rev. D, 98, 064012, doi: 10.1103/PhysRevD.98.064012

Rodriguez, C. L., Amaro-Seoane, P., Chatterjee, S., et al. 2018, Phys. Rev. D, 98, 123005, doi: 10.1103/PhysRevD.98.123005

Rodriguez, C. L., & Antonini, F. 2018, ApJ, 863, 7, doi: 10.3847/1538-4357/aacea4

Rodriguez, C. L., Chatterjee, S., & Rasio, F. A. 2016a, Phys. Rev. D, 93, 084029, doi: 10.1103/PhysRevD.93.084029

Rodriguez, C. L., Haster, C.-J., Chatterjee, S., Kalogera, V., & Rasio, F. A. 2016b, ApJL, 824, L8, doi: 10.3847/2041-8205/824/1/L8

Rodriguez, C. L., Morscher, M., Pattabiraman, B., et al. 2015, Phys. Rev. Lett., 115, 051101, doi: 10.1103/PhysRevLett.115.051101

Rodriguez, C. L., Zevin, M., Pankow, C., Kalogera, V., & Rasio, F. A. 2016c, ApJL, 832, L2, doi: 10.3847/2041-8205/832/1/L2

Rodriguez, C. L., Weatherford, N. C., Coughlin, S. C., et al. 2022, ApJS, 258, 22, doi: 10.3847/1538-4365/ac2edf

Romero-Shaw, I., Lasky, P. D., & Thrane, E. 2021, ApJL, 921, L31, doi: 10.3847/2041-8213/ac3138

Romero-Shaw, I., Lasky, P. D., Thrane, E., & Calderón Bustillo, J. 2020, ApJL, 903, L5, doi: 10.3847/2041-8213/abbe26

Rowan, C., Boekholt, T., Kocsis, B., & Haiman, Z. 2023, MNRAS, 524, 2770, doi: 10.1093/mnras/stad1926

Rowan, C., Whitehead, H., Boekholt, T., Kocsis, B., & Haiman, Z. 2024, MNRAS, 527, 10448, doi: 10.1093/mnras/stad3641

Rowan, C., Whitehead, H., Fabj, G., et al. 2025a, MNRAS, 539, 1501, doi: 10.1093/mnras/staf547

Rowan, C., Whitehead, H., & Kocsis, B. 2025b, MNRAS, 544, 4576, doi: `10.1093/mnras/staf1896`

Ryan, F. D. 1995, Phys. Rev. D, 52, 5707, doi: `10.1103/PhysRevD.52.5707`

Saini, P., Zwick, L., Takátsy, J., et al. 2025, Phys. Rev. D, 112, 103047, doi: `10.1103/8bt1-xgh4`

Samsing, J. 2018, Phys. Rev. D, 97, 103014, doi: `10.1103/PhysRevD.97.103014`

Samsing, J., Askar, A., & Giersz, M. 2018a, ApJ, 855, 124, doi: `10.3847/1538-4357/aaab52`

Samsing, J., & D'Orazio, D. J. 2018, MNRAS, 481, 5445, doi: `10.1093/mnras/sty2334`

Samsing, J., D'Orazio, D. J., Kremer, K., Rodriguez, C. L., & Askar, A. 2020, Phys. Rev. D, 101, 123010, doi: `10.1103/PhysRevD.101.123010`

Samsing, J., Hamers, A. S., & Tyles, J. G. 2019, Phys. Rev. D, 100, 043010, doi: `10.1103/PhysRevD.100.043010`

Samsing, J., Hendriks, K., Zwick, L., D'Orazio, D. J., & Liu, B. 2025, ApJ, 990, 211, doi: `10.3847/1538-4357/ad9f3d`

Samsing, J., & Hotokezaka, K. 2021, ApJ, 923, 126, doi: `10.3847/1538-4357/ac2b27`

Samsing, J., & Ilan, T. 2018, MNRAS, 476, 1548, doi: `10.1093/mnras/sty197`

Samsing, J., MacLeod, M., & Ramirez-Ruiz, E. 2014, ApJ, 784, 71, doi: `10.1088/0004-637X/784/1/71`

—. 2017, ApJ, 846, 36, doi: `10.3847/1538-4357/aa7e32`

—. 2018b, ApJ, 853, 140, doi: `10.3847/1538-4357/aaa715`

Samsing, J., & Ramirez-Ruiz, E. 2017, ApJL, 840, L14, doi: 10.3847/2041-8213/aa6f0b

Samsing, J., Bartos, I., D'Orazio, D. J., et al. 2022, Nature, 603, 237, doi: 10.1038/s41586-021-04333-1

Samsing, J., Zwick, L., Saini, P., et al. 2024, arXiv e-prints, arXiv:2412.14159, doi: 10.48550/arXiv.2412.14159

Sasaki, M., Suyama, T., Tanaka, T., & Yokoyama, S. 2016, Physical Review Letters, 117, 061101, doi: 10.1103/PhysRevLett.117.061101

Sathyaprakash, B. S., & Schutz, B. F. 2009, Living Reviews in Relativity, 12, 2, doi: 10.12942/lrr-2009-2

Sberna, L., Babak, S., Marsat, S., et al. 2022, Phys. Rev. D, 106, 064056, doi: 10.1103/PhysRevD.106.064056

Schrøder, S. L., Batta, A., & Ramirez-Ruiz, E. 2018, ApJL, 862, L3, doi: 10.3847/2041-8213/aacf8d

Schwarzschild, K. 1916, Sitzungsberichte der Königlich Preussischen Akademie der Wissenschaften, 189

Silsbee, K., & Tremaine, S. 2017, ApJ, 836, 39, doi: 10.3847/1538-4357/aa5729

Sparke, L. S., & Gallagher, III, J. S. 2000, Galaxies in the universe : an introduction

Spera, M., Mapelli, M., Giacobbo, N., et al. 2019, MNRAS, 485, 889, doi: 10.1093/mnras/stz359

Speri, L., Antonelli, A., Sberna, L., et al. 2023, Physical Review X, 13, 021035, doi: 10.1103/PhysRevX.13.021035

Spieksma, T. F. M., Cardoso, V., Carullo, G., Della Rocca, M., & Duque, F. 2025, Phys. Rev. Lett., 134, 081402, doi: 10.1103/PhysRevLett.134.081402

Stephan, A. P., Naoz, S., Ghez, A. M., et al. 2016, MNRAS, 460, 3494, doi: 10.1093/mnras/stw1220

Stevenson, S., Vigna-Gómez, A., Mandel, I., et al. 2017, Nature Communications, 8, 14906, doi: 10.1038/ncomms14906

Stone, N. C., Metzger, B. D., & Haiman, Z. 2017, MNRAS, 464, 946, doi: 10.1093/mnras/stw2260

Strokov, V., Fragione, G., Wong, K. W. K., Helfer, T., & Berti, E. 2022, Phys. Rev. D, 105, 124048, doi: 10.1103/PhysRevD.105.124048

Su, Y., Liu, B., & Lai, D. 2021, MNRAS, 505, 3681, doi: 10.1093/mnras/stab1617

Tagawa, H., Haiman, Z., & Kocsis, B. 2020, ApJ, 898, 25, doi: 10.3847/1538-4357/ab9b8c

Tagawa, H., Rowan, C., Takátsy, J., et al. 2025, arXiv e-prints, arXiv:2511.15193, doi: 10.48550/arXiv.2511.15193

Takahashi, R., & Nakamura, T. 2003, ApJ, 595, 1039, doi: 10.1086/377430

Takátsy, J., Zwick, L., Hendriks, K., et al. 2025, Classical and Quantum Gravity, 42, 215006, doi: 10.1088/1361-6382/ae0fd4

Tamanini, N., Klein, A., Bonvin, C., Barausse, E., & Caprini, C. 2020, Phys. Rev. D, 101, 063002, doi: 10.1103/PhysRevD.101.063002

Tanay, S., Haney, M., & Gopakumar, A. 2016, Physical Review D, 93, 064031, doi: 10.1103/PhysRevD.93.064031

Tanikawa, A. 2013, MNRAS, 435, 1358, doi: 10.1093/mnras/stt1380

Tanikawa, A., Susa, H., Yoshida, T., Trani, A. A., & Kinugawa, T. 2021, ApJ, 910, 30, doi: 10.3847/1538-4357/abe40d

Tanikawa, A., Yoshida, T., Kinugawa, T., et al. 2022, ApJ, 926, 83, doi: 10.3847/1538-4357/ac4247

The LIGO Scientific Collaboration, the Virgo Collaboration, the KAGRA Collaboration, et al. 2023, Physical Review X, 13, 041039, doi: 10.1103/PhysRevX.13.041039

—. 2025a, arXiv e-prints, arXiv:2508.18082, doi: 10.48550/arXiv.2508.18082

—. 2025b, arXiv e-prints, arXiv:2508.18083, doi: 10.48550/arXiv.2508.18083

Tiede, C., D'Orazio, D. J., Zwick, L., & Duffell, P. C. 2024, ApJ, 964, 46, doi: 10.3847/1538-4357/ad2613

Tiwari, A., Vijaykumar, A., Kapadia, S. J., Chatterjee, S., & Fragione, G. 2025a, Phys. Rev. D, 112, 084034, doi: 10.1103/gspl-m478

Tiwari, A., Vijaykumar, A., Kapadia, S. J., Fragione, G., & Chatterjee, S. 2024, MNRAS, 527, 8586, doi: 10.1093/mnras/stad3749

Tiwari, A., Vijaykumar, A., Kapadia, S. J., Ghosh, S., & Nielsen, A. B. 2025b, arXiv e-prints, arXiv:2506.22272, doi: 10.48550/arXiv.2506.22272

Torres-Orjuela, A., Chen, X., & Amaro-Seoane, P. 2020, Phys. Rev. D, 101, 083028, doi: 10.1103/PhysRevD.101.083028

Torres-Orjuela, A., Chen, X., Cao, Z., Amaro-Seoane, P., & Peng, P. 2019, Phys. Rev. D, 100, 063012, doi: 10.1103/PhysRevD.100.063012

Toubiana, A., Sberna, L., Caputo, A., et al. 2021, Phys. Rev. Lett., 126, 101105, doi: 10.1103/PhysRevLett.126.101105

Trani, A. A., Leigh, N. W. C., Boekholt, T. C. N., & Portegies Zwart, S. 2024a, A&A, 689, A24, doi: 10.1051/0004-6361/202449862

Trani, A. A., Quaini, S., & Colpi, M. 2024b, A&A, 683, A135, doi: 10.1051/0004-6361/202347920

Trani, A. A., Rastello, S., Di Carlo, U. N., et al. 2022, MNRAS, 511, 1362, doi: 10.1093/mnras/stac122

Trani, A. A., Spera, M., Leigh, N. W. C., & Fujii, M. S. 2019, ApJ, 885, 135, doi: 10.3847/1538-4357/ab480a

Trani, A. A., Tanikawa, A., Fujii, M. S., Leigh, N. W. C., & Kumamoto, J. 2021, MNRAS, 504, 910, doi: 10.1093/mnras/stab967

Tutukov, A. V., & Yungelson, L. R. 1993, MNRAS, 260, 675, doi: 10.1093/mnras/260.3.675

Vaccaro, M. P., Mapelli, M., Périgois, C., et al. 2024, aap, 685, A51, doi: 10.1051/0004-6361/202348509

Vaccaro, M. P., Seif, Y., & Mapelli, M. 2025, arXiv e-prints, arXiv:2508.03637, doi: 10.48550/arXiv.2508.03637

van Son, L. A. C., de Mink, S. E., Callister, T., et al. 2022, ApJ, 931, 17, doi: 10.3847/1538-4357/ac64a3

VanLandingham, J. H., Miller, M. C., Hamilton, D. P., & Richardson, D. C. 2016, ApJ, 828, 77, doi: 10.3847/0004-637X/828/2/77

Verbiest, J. P. W., Lentati, L., Hobbs, G., et al. 2016, MNRAS, 458, 1267, doi: 10.1093/mnras/stw347

Vijaykumar, A., Hanselman, A. G., & Zevin, M. 2024, ApJ, 969, 132, doi: 10.3847/1538-4357/ad4455

Vijaykumar, A., Tiwari, A., Kapadia, S. J., Arun, K. G., & Ajith, P. 2023, ApJ, 954, 105, doi: 10.3847/1538-4357/acd77d

Wang, Y., Stebbins, A., & Turner, E. L. 1996, Phys. Rev. Lett., 77, 2875, doi: 10.1103/PhysRevLett.77.2875

Wen, L. 2003, ApJ, 598, 419, doi: 10.1086/378794

Whitehead, H., Rowan, C., Boekholt, T., & Kocsis, B. 2024, MNRAS, 531, 4656, doi: 10.1093/mnras/stae1430

Wong, K. W. K., Baibhav, V., & Berti, E. 2019, MNRAS, 488, 5665, doi: 10.1093/mnras/stz2077

Woosley, S. E. 2016, ApJL, 824, L10, doi: 10.3847/2041-8205/824/1/L10

Xuan, Z., Naoz, S., & Chen, X. 2023, Phys. Rev. D, 107, 043009, doi: 10.1103/PhysRevD.107.043009

Yan, H., Chen, X., & Torres-Orjuela, A. 2023, Phys. Rev. D, 107, 103044, doi: 10.1103/PhysRevD.107.103044

Yang, S.-C., Han, W.-B., Tagawa, H., Li, S., & Zhang, C. 2025, ApJL, 988, L41, doi: 10.3847/2041-8213/adeaad

Yang, Y., Bartos, I., Gayathri, V., et al. 2019, Phys. Rev. Lett., 123, 181101, doi: 10.1103/PhysRevLett.123.181101

Yunes, N., Arun, K. G., Berti, E., & Will, C. M. 2009, Phys. Rev. D, 80, 084001, doi: 10.1103/PhysRevD.80.084001

Yunes, N., Miller, M. C., & Thornburg, J. 2011, Phys. Rev. D, 83, 044030, doi: 10.1103/PhysRevD.83.044030

Zackay, B., Venumadhav, T., Dai, L., Roulet, J., & Zaldarriaga, M. 2019, Phys. Rev. D, 100, 023007, doi: 10.1103/PhysRevD.100.023007

Zaldarriaga, M., Kushnir, D., & Kollmeier, J. A. 2018, MNRAS, 473, 4174, doi: 10.1093/mnras/stx2577

Zevin, M., Pankow, C., Rodriguez, C. L., et al. 2017, ApJ, 846, 82, doi: 10.3847/1538-4357/aa8408

Zevin, M., Samsing, J., Rodriguez, C., Haster, C.-J., & Ramirez-Ruiz, E. 2019, ApJ, 871, 91, doi: 10.3847/1538-4357/aaf6ec

Zevin, M., Bavera, S. S., Berry, C. P. L., et al. 2021, ApJ, 910, 152, doi: 10.3847/1538-4357/abe40e

Zwick, L., Capelo, P. R., Bortolas, E., Mayer, L., & Amaro-Seoane, P. 2020, MNRAS, 495, 2321, doi: 10.1093/mnras/staa1314

Zwick, L., Capelo, P. R., Bortolas, E., et al. 2021, Monthly Notices of the Royal Astronomical Society, 506, 1007, doi: 10.1093/mnras/stab1818

Zwick, L., Capelo, P. R., & Mayer, L. 2023, MNRAS, 521, 4645, doi: 10.1093/mnras/stad707

Zwick, L., Hendriks, K., Saini, P., et al. 2025a, arXiv e-prints, arXiv:2511.04540, doi: 10.48550/arXiv.2511.04540

Zwick, L., & Samsing, J. 2025, ApJ, 988, 272, doi: 10.3847/1538-4357/adea54

Zwick, L., Takátsy, J., Saini, P., et al. 2025b, ApJ, 991, 131, doi: 10.3847/1538-4357/adf6b8

Zwick, L., Tiede, C., Trani, A. A., et al. 2024, Phys. Rev. D, 110, 103005, doi: 10.1103/PhysRevD.110.103005

Zwick, L., Hendriks, K., O'Neill, D., et al. 2025c, Phys. Rev. D, 112, 063005, doi: 10.1103/lz7k-bvjf